Fabrication and Study of magnetic and transport properties of GdCo thin films, GdCo-based multilayers and Fe/Cr multilayers

Nguyen Thanh Nam

UNIVERSITÉ JOSEPH FOURIER, GRENOBLE

and

VIETNAM NATIONAL UNIVERSITY, HANOI

----------*****----------

PhD THESIS/THÈSE

Presented by/ Présentée par

NGUYEN THANH NAM

FABRICATION AND STUDY OF MAGNETIC AND TRANSPORT PROPERTIES OF GdCo THIN FILMS, GdCo-BASED MULTILAYERS AND Fe/Cr MULTILAYERS

For the degree of Doctor of Physics - Materials Science

Pour obtenir le titre de Docteur de Physique- Sciences des Matériaux

Date of defence/Date de soutenance: 05 November 2007/ 05 Novembre 2007

Examining Committee/ Composition du Jury:

Prof. V. Skumryev	Universitat Autònoma de Barcelona	Referee/Rapporteur
Prof. N. H. Nghi	Hanoi University of Technology	Referee/Rapporteur
Dr. L. Ranno	Université Joseph Fourier, Grenoble	Supervisor/Directeur de thèse
Prof. N. H. Duc	Vietnam National University, Hanoi	Supervisor/Directeur de thèse
Dr. C. Meyer	CNRS, Grenoble	Supervisor/Directeur de thèse
Dr. M. Viret	CEA, Saclay	Examiner/Examinateur

Thesis was prepared at/ Thèse préparée à

INSTITUT NÉEL, CNRS-UJF, GRENOBLE **and/et** CRYOLAB, VNU, HANOI

To my dear Oclt

Acknowledgements

I would like to thank:

My supervisors: Dr. Laurent Ranno (UJF), Prof. Nguyen Huu Duc (VNUH), and Dr. Claire Meyer (IN).

Institut Néel (CNRS).

Cryogenic Laboratory (VNUH).

Project 322 (Vietnam)

Center of Material Science (VNUH).

I greatly appreciate all the assistance from:

David Barral and Philippe David: *Thin film deposition.*

Annick Liénard: *AFM, EDX measurements.*

Richard Haettel: *Targets fabrication.*

Helge Haas: *Dektak, Lithography, Etching experiments.*

Content

Introduction

In recent decades, the transport properties (Hall effect and Magnetoresistance) of thin films which contain layers of magnetic materials have been studied a lot. The Extraordinary Hall Effect (EHE) in magnetic thin films and the Giant MagnetoResistance (GMR) in magnetic multilayers reveal the asymmetries of densities of state, scattering probabilities, mean-free paths between spin ↑ and spin ↓ channels of conduction electrons in magnetic materials. Using the electron spin as an extra designing degree of freedom laid the foundation of a new field which has rapidly lead to application : spinelectronics or spintronics. Although the application of spintronics has been developing very fast, some mechanisms related to the spin of electrons are still not fully understood. The aim of this thesis is to study the magnetic and transport properties of GdCo thin films, GdCo-based multilayers, and Fe/Cr multilayers.

The $Gd_{1-x}Co_x$ alloys have been chosen as the main object for the study for the following reasons:

(i). $Gd_{1-x}Co_x$ alloy is a metallic ferrimagnetic material with an expected high spin polarisation in the conduction band. The different temperature dependences of the Gd and Co sublattice magnetisations can induce a compensation temperature (T_{comp}). Close to compensation, the magnetisation of $Gd_{1-x}Co_x$ alloy varies linearly with temperature and cancels out at T_{comp}. Thus, it is possible to cancel demagnetising fields and Zeeman energy. Because the magnetisation is changed from Gd-dominant ($T < T_{comp}$) to Co-dominant ($T > T_{comp}$) at T_{comp}, the spin polarisation of conduction electrons (P) is reversed at T_{comp} too. In the cases of sputtered $Gd_{1-x}Co_x$ thin films, a uniaxial anisotropy can be induced out-of-plane, leading to a spontaneous perpendicular magnetisation in a large temperature range around T_{comp}. A special surface with zero spontaneous magnetisation, called the compensation surface, can be created in $Gd_{1-x}Co_x$ thin films with an in-plane composition gradient. This compensation surface divides the film into two zones: Co-dominant zone with positive P and Gd-dominant zone with negative P. An ideal 180^o domain wall called the compensation domain wall can be created parallel to the compensation surface when a magnetic field is applied on this film. The compensation domain wall with no magnetisation, i.e. no demagnetising energy, may become very useful for studying the role of magnetisation in the effects related to spin transport through domain walls (including spin injection and spin torque effects).

(ii). The spin-flop phenomenon of $Gd_{1-x}Co_x$ alloys can give important information about the exchange interaction between the Gd and Co magnetic sublattices. However, since the spin-flop field (B_{sf}) is usually very large, this phenomenon has not been experimentally studied except a unique study on a $GdCo_5$ single crystal with B_{sf} = 46 T at 5 K. Using $Gd_{1-x}Co_x$ alloy

near its T_{comp} , one can reduce B_{sf} to a few Tesla, this let us experimentally consider the spin-flop phenomenon in the vicinity of T_{comp} with the applied fields up to 6 T available at Institut Néel.

(iii). Different from the EHE of ferromagnetic materials where the Hall voltage is proportional to the sample magnetisation, in the case of ferrimagnetic materials, e.g. $Gd_{1-x}Co_x$, the contributions of the sublattice magnetisations to EHE are different. Although the EHE of $Gd_{1-x}Co_x$ alloys has been studied a lot in the 1970s, the contributions of Gd and Co sublattices to the EHE is still discussed. In our study, the magnetisation of $Gd_{1-x}Co_x$ can be experimentally measured by SQUID magnetometer at temperatures from 5 K to 300 K, and then the results are used to improve a mean-field calculation for the $Gd_{1-x}Co_x$ alloys. When comparing the temperature dependences of the Gd and Co sublattice magnetisations calculated by the mean-field theory to the experimental temperature dependence of the Hall resistivity, the Hall coefficients of the Gd and Co sublattices can be quantitatively estimated. Moreover, when the spin-flop phenomenon occurs, the ferrimagnetic configuration is broken, so the Hall behaviour of ferrimagnetic materials is more complicated and in need of new studies.

The mechanism of giant magnetoresistance (GMR) is due to spin dependent scatterings in magnetic layers. However, in nano scale systems such as GMR multilayers, the scatterings in bulk layers and at interfaces can be different. In some case, the interface scattering is dominant and plays a very important role in the spin dependent effects (EHE, GMR). In this thesis, GMR of Fe/Cr multilayer will be revisited with the change of Fe layer thickness to figure out the contribution of interface scattering to GMR.

In the traditional GMR junctions, the spontaneous magnetisation of magnetic layers is correctly assumed to be a constant (i.e. Fe, Co, Ni, NiFe) since experimental and application temperatures are far below the Curie temperatures. Here we use also $Gd_{1-x}Co_x$ close to its compensation temperature T_{comp} to allow magnetisation to be an extra degree of freedom keeping perpendicular anisotropy and long range magnetic order constant. Consequently, a new type of GMR junction with perpendicular anisotropy of the magnetic layer (i.e. $Gd_{1-x}Co_x$) is created. By changing the temperature across T_{comp}, the GMR can be studied with the variations of the film magnetisation and the spin polarisation of conduction electrons. Since the EHE of $Gd_{1-x}Co_x$ layer is quite large and very sensitive to the perpendicular part of its magnetisation, EHE can be used as an advanced method to investigate the rotation of $Gd_{1-x}Co_x$ magnetisation during the magnetisation process of the GMR junction.

This thesis includes seven chapters organised into two parts: The first part includes chapters 1, 2, 3, and 4 and is about the extraordinary Hall effect and magnetic properties of $Gd_{1-x}Co_x$ thin films. The second part involving chapters 5, 6, and 7 is about giant magnetoresistance of Fe/Cr and $Fe_{19}Ni_{81}$/Cu/$Gd_{1-x}Co_x$ multilayers. The specific contents of the chapters are:

- Chapter 1 is written as a short literature review about the magnetic properties and the extraordinary Hall effect of $Gd_{1-x}Co_x$ alloys. The mean-field theory will be introduced and some mean-field calculated results will be presented to evaluate the influence of the perpendicular anisotropy of $Gd_{1-x}Co_x$ thin film on the spin-flop phenomenon of $Gd_{1-x}Co_x$ alloys.
- Chapter 2 concerns the experimental techniques used to fabricate and characterise the samples. Among them, the transport measurement technique will be presented in more detail. The data processing technique for separating MR signal and Hall signal from each other will be clearly described.
- Chapter 3: All the results and discussions about the compensation domain wall in the $Gd_{1-x}Co_x$ thin film with an in-plane gradient of composition are shown in detail. The movement of the compensation domain wall following the variation of temperature is observed by means of the polar Kerr microscopy. The in-plane composition gradient of $Gd_{1-x}Co_x$ thin film is finally calculated by comparing the mean-field results with the experimental results of the compensation domain wall movement.
- Chapter 4: The extraordinary Hall effect and the magnetic properties of $Gd_{1-x}Co_x$ thin film are studied at temperatures between 5 K and 300 K. The quantitative contributions of the Gd and Co sublattice magnetisations to the EHE of $Gd_{1-x}Co_x$ thin film are estimated. The composition of $Gd_{1-x}Co_x$ alloys is chosen to have a compensation temperature below 300 K. Near T_{comp}, the spin-flop phenomenon is observed by means of the extraordinary Hall effect in an applied field up to 6 Tesla. The experimental spin-flop fields are compared to the spin-flop fields calculated by mean-field theory.
- Chapter 5: This chapter is a short summary of the magnetoresistive effects, among them the giant magnetoresistance (GMR) will be introduced in detail. The spin dependent scattering mechanism of GMR will be explained. The important role of the spin dependent scattering asymmetric coefficients of magnetic layer in GMR junction will be interpreted.
- Chapter 6: GMR of Fe/Cr multilayers is studied as a function of temperature between 77 K and 300 K. The variation of the Fe layer thickness while the thickness of Cr layer is fixed and the influence of thermal anneals allow us to evaluate the contribution of scatterings in the Fe/Cr interfaces to GMR.
- Chapter 7: $Gd_{1-x}Co_x$ alloy is applied to make a new type of GMR junction. One magnetic layer ($Gd_{1-x}Co_x$) has perpendicular anisotropy and the other magnetic layer ($Ni_{81}Fe_{19}$) has in-plane anisotropy. The transport and magnetic behaviours of the sample will be considered as a function of temperature (from 5 K to 300 K) and applied field (from 0 T to 6 T).

- Finally, in the main conclusion, the results and future work suggestions are summarised.

All studies in this thesis have been carried out in the framework of the cooperation program between Vietnam National University in Hanoi (VNUH) and Joseph Fourier University (UJF). The PhD scholarship was partially granted by Project 322 of Vietnam Government and partially funded from the Nanomagnetism group of Institut Néel (CNRS-UJF, Grenoble, France).

Chapter. 1. Magnetic and transport properties of $Gd_{1-x}Co_x$ ferrimagnetic alloys

1.1. Ferrimagnetism

Ferromagnetism is the magnetic state where a long range parallel alignment of all the magnetic moments of the material exists in the absence of an applied magnetic field. This long range order disappears above a critical temperature called the Curie temperature (T_C). Below T_c, a spontaneous magnetisation exists (Fig. 1.1.a). For example, Fe is a ferromagnetic material with T_C = 1043 K. Below 1043 K, the magnetic moments of Fe atoms are parallel to each other.

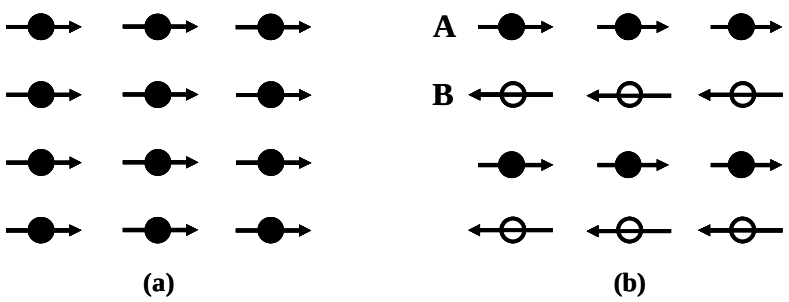

Fig. 1.1. Magnetic configurations of ferromagnetism (a) and ferrimagnetism (b).

Ferrimagnetism is a collinear magnetic phase where two magnetic sublattices (A and B in Fig. 1.1.b) can be defined. The term "sublattice" has no crystallographic meaning but refers only to the magnetic structure. In each sublattice, the magnetic moments are coupled ferromagnetically. Both sublattice magnetisations are coupled antiferromagnetically (Fig. 1.1.b). For example, $GdCo_5$ crystal is a ferrimagnetic material, where the magnetic moments of Co (or A) atoms are parallel to each other and they are antiparallel to the magnetic moments of Gd (or B) atoms.

Since the temperature dependences of both sublattice magnetisations are usually different, the temperature dependence of the total magnetisation of ferrimagnetic materials is quite complicated, and sometimes a compensation temperature (T_{comp}) can be produced. At T_{comp}, the sublattice magnetisations are compensated, therefore, the total magnetisation is zero. Fig. 1.2 shows three typical temperature dependences of the total magnetisation of ferrimagnetic materials. Basically, antiferromagnetism can be considered as a specific case of ferrimagnetism where the two sublattices have the same nature, so the total magnetisation is compensated at all temperatures.

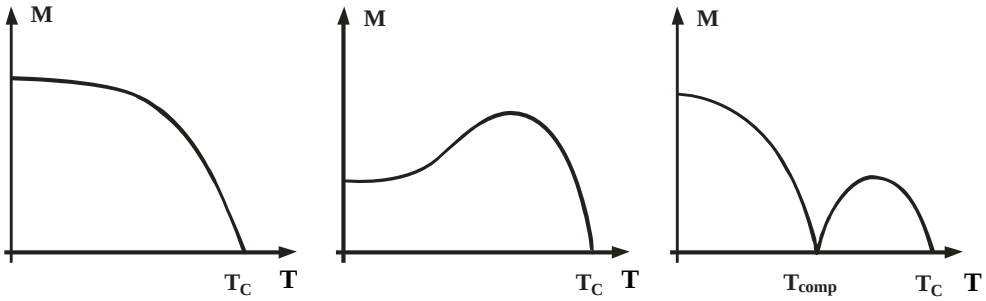

Fig. 1.2. Three typical temperature dependences of the spontaneous magnetisation of a ferrimagnetic material where T_C and T_{comp} are the Curie temperature and the compensation temperature, respectively.

1.2. Magnetic properties of $Gd_{1-x}Co_x$ alloys

In the case of $Gd_{1-x}Co_x$ alloys, their magnetic properties strongly depend on composition. When the Co content is high ($x > 0.5$), the Co-Co exchange interaction is very strong, therefore the magnetic moments of Co atoms are parallel even in the amorphous state. The Gd-Co negative exchange interaction is strong enough to keep Co and Gd moments antiparallel. Therefore, $Gd_{1-x}Co_x$ alloy with two magnetic sublattices of Gd and Co is a ferrimagnetic material in both crystalline and amorphous states (refs. [1]-[4]).

Because the Gd and Co sublattice magnetisations depend on the temperature in different manner, a compensation temperature (T_{comp}) can be obtained in a certain range of concentration. When a compensation temperature exists, the sublattice magnetisations are compensated at T_{comp} and the spontaneous magnetisation is zero (refs. [1], [5], and [6]).

1.2.1. Mean-field calculation for $Gd_{1-x}Co_x$ as a ferrimagnetic material

It is difficult to measure directly the sublattice magnetisations. A mean-field calculation [4] will be used to calculate the sublattice magnetisations of a ferrimagnetic material at any temperature. This method is explained hereafter in the case of $Gd_{1-x}Co_x$ ferrimagnetic alloys.

In zero external magnetic field, the magnetisations of Co and Gd sublattices are antiparallel. When an external magnetic field $\vec{H}$ is applied, the magnetic configuration of the $Gd_{1-x}Co_x$ alloy depends on the field strength. The mean internal magnetic field (also called the molecular field) of the alloy varies from Co atom position ($\overrightarrow{H_{Co}}$) to Gd atom position ($\overrightarrow{H_{Gd}}$) and can be written as:

$$\overrightarrow{H_{Co}} = \vec{H} + \lambda_{CoCo}\overrightarrow{M_{Co}} - \lambda_{CoGd}\overrightarrow{M_{Gd}} \qquad \textbf{(1.1.a)}$$

$$\overrightarrow{H_{Gd}} = \vec{H} - \lambda_{GdCo}\overrightarrow{M_{Co}} + \lambda_{GdGd}\overrightarrow{M_{Gd}} \qquad \textbf{(1.1.b)}$$

Where $\vec{H}$ is the applied field, $\overrightarrow{M_{Co}}$ and $\overrightarrow{M_{Gd}}$ are respectively the magnetisations of Co and Gd sublattices, $\lambda_{CoGd} = \lambda_{CoGd} = \lambda$ is the Co-Gd intersublattice molecular field coefficient,

λ_{CoCo} and λ_{GdGd} are respectively the Co-Co and Gd-Gd intrasublattice molecular field coefficients. These molecular field coefficients are unitless and of the order of $\lambda_{CoCo} \sim 1000$, $\lambda_{CoGd} \sim 100$, and $\lambda_{GdGd} \sim 10$. Since the Gd-Gd exchange interaction (λ_{GdGd}) is the weakest of the three, it is usually neglected. So equations (1.1) can then be written as:

$$\overrightarrow{H_{Co}} = \vec{H} + \lambda_{CoCo}\overrightarrow{M_{Co}} - \lambda\overrightarrow{M_{Gd}} \qquad \textbf{(1.2.a)}$$

$$\overrightarrow{H_{Gd}} = \vec{H} - \lambda\overrightarrow{M_{Co}} \qquad \textbf{(1.2.b)}$$

Assuming that the magnetic moments are mainly localised, according to Brillouin theory, the Gd and Co sublattice magnetisations can be obtained by solving the following equations:

$$M_{Co} = xN\mu_{Co}B_{J_{Co}}\left(\frac{\mu_o\overrightarrow{\mu_{Co}}.(\vec{H} + \lambda_{CoCo}\overrightarrow{M_{Co}} - \lambda\overrightarrow{M_{Gd}})}{k_B T}\right) \qquad \textbf{(1.3.a)}$$

$$M_{Gd} = (1-x)N\mu_{Gd}B_{J_{Gd}}\left(\frac{\mu_o\overrightarrow{\mu_{Gd}}.(\vec{H} - \lambda\overrightarrow{M_{Co}})}{k_B T}\right) \qquad \textbf{(1.3.b)}$$

where N is the number of atoms per volume unit, $\mu_{Co} = g_{Co}J_{Co}\mu_B$ and $\mu_{Gd} = g_{Gd}J_{Gd}\mu_B$ are respectively the magnetic moments of Co and Gd atoms, and B_J is the Brillouin function.

In order to apply the mean-field theory to calculate the magnetisation of $Gd_{1-x}Co_x$ ferrimagnetic alloys, many input parameters must be known, among them the Co-Co intrasublattice molecular field coefficient λ_{CoCo} and the Gd-Co intersublattice molecular field coefficient λ play very important roles in the magnetic properties of the alloys. λ_{CoCo} has a strong effect on T_C and a slight effect on T_{comp}, while λ has a very important influence on T_{comp} and a very weak influence on T_C. Both λ_{CoCo} and λ depend not only on the composition but also on the structure (crystalline or amorphous) of these alloys [7].

The shape anisotropy (films) and the magnetic anisotropy can be included in the molecular fields. In this work, the anisotropy will be taken into account when calculating the magnetisation processes under field, not the magnetisations of both sublattices.

Since the mean-field theory does not account for spin-wave excitations at low temperatures and does not account for the exchange fluctuation near the Curie temperature, the calculated temperature dependence of the magnetisation is less temperature-dependent at low temperature compared to the experimental one (refs. [4] and [8]). However, the input parameters of the mean-field calculation can be determined from experiments (see section 4.5.1), and the model gives M(T) from 0 K to temperatures larger than T_c, that is why we chose a mean-field theory for this thesis.

1.2.2. Magnetic properties of $Gd_{1-x}Co_x$ alloys

In 1989, Hansen et al [3] performed a lot of mean-field calculations for $Gd_{1-x}Co_x$ alloys.

Their calculation results have been compared to the experimental magnetisations of amorphous $Gd_{1-x}Co_x$ alloys. The comparison presented in Fig. 1.3 shows a good agreement between calculations and experiments in the range of temperatures below 500 K.

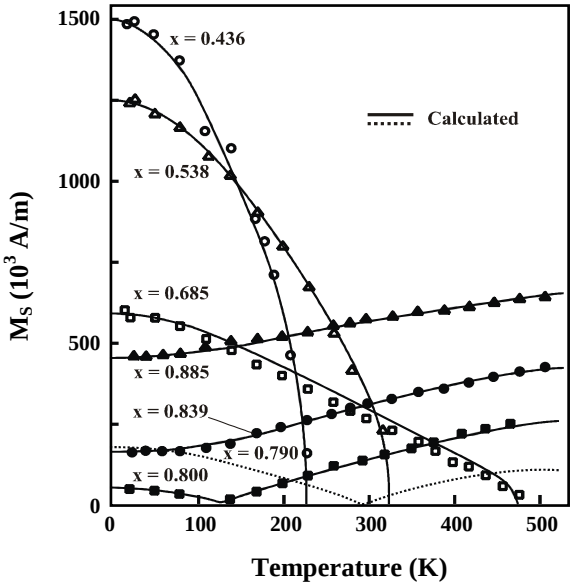

Fig. 1.3. Temperature dependence of the saturation magnetisation of amorphous $Gd_{1-x}Co_x$ alloys. The solid lines and dash line are results of the mean-field calculation of Hansen et al [4].

Around x = 0.80, 1% change of the Co composition makes 145 K change of the compensation temperature (T_{comp} increases from 4.2 K with x = 0.81 to 295 K with x = 0.79). A collection of T_{comp} is summarised in Fig. 1.4 (refs. [3]-[5]). It turns out from this figure that the mean slope of T_{comp} (about 70 K/at.%) is nearly twice smaller than that obtained from the calculations of Hansen et al (about 145 K/at.%). This large difference and the wide distribution of T_{comp} near x = 0.8 make question about how Hansen et al chose the value for the intersublattice molecular field coefficient λ in their mean-field calculations, and point at the difficulty to compare models and experiments in the published literature.

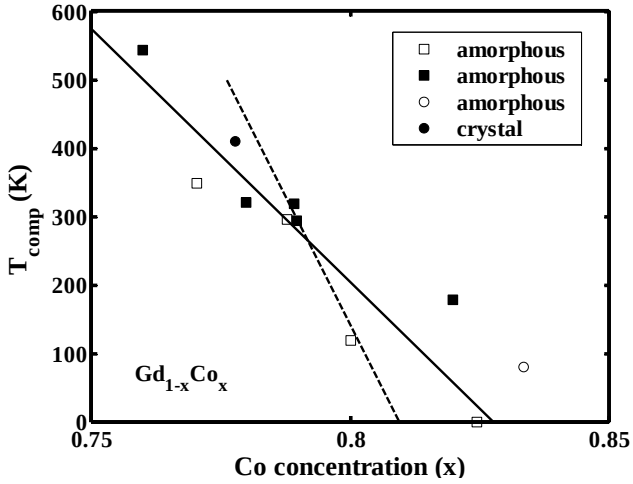

Fig. 1.4. The composition dependence of the compensation temperature (T_{comp}) of several amorphous and crystalline $Gd_{1-x}Co_x$ alloys (refs. [3]-[5]). The mean slope of T_{comp} is found to be about 70 K/at. % (solid line). The calculations of Hansen et al are also plotted as the dash line with a slope of 145 K/at.%.

Furthermore, the calculations of Hansen et al have been compared to experimental data in the range of temperatures below 500 K while the Curie temperature (T_C) of $Gd_{1-x}Co_x$ alloys with $x \approx 0.8$ is at least above 600 K (see Fig. 1.5). So it is difficult to know the agreement between calculation and experiment near T_C, i.e. the appropriateness of λ_{CoCo} used in their calculations.

The Curie temperature (T_C) of $Gd_{1-x}Co_x$ alloys imported from reference [4] are shown in Fig. 1.5. Because the amorphous $Gd_{1-x}Co_x$ alloys crystallise at high temperature (The crystallisation temperature depends on the composition. The higher the Co composition, the lower the crystallisation temperature), it is impossible to measure T_C of an amorphous $Gd_{1-x}Co_x$ alloy if it is above the crystallisation temperature. That is why there are no experimental values of T_C for the amorphous $Gd_{1-x}Co_x$ alloys above 620 K ($x > 0.70$). Therefore, T_C of an amorphous $Gd_{1-x}Co_x$ alloy when $x > 0.70$ must be extrapolated.

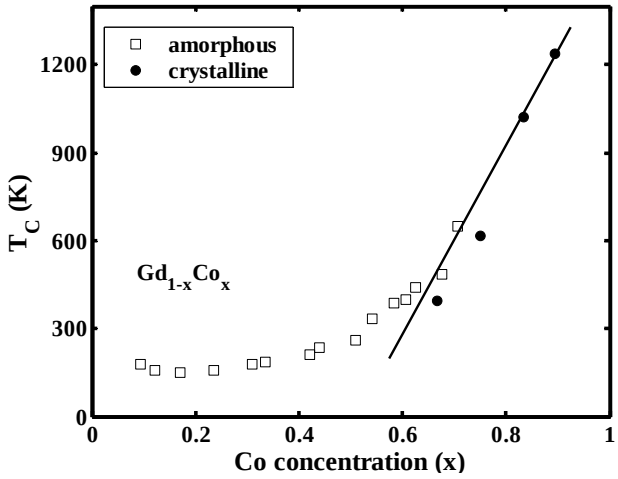

Fig. 1.5. The composition dependence of T_C of several amorphous and crystalline $Gd_{1-x}Co_x$ alloys, all these data are published in ref. [4]. The solid line serves as a guide for eyes.

In short, although there are many studies on the magnetic properties of $Gd_{1-x}Co_x$ alloys, the disagreement between studies is still large, especially in the compositional variation of T_{comp}. The dispersive distribution of T_{comp} versus composition in Fig. 1.4 is supposedly due to the two following reasons:

- The precision of composition measurements can be different between different studies depending on the composition measurement techniques. For example, the error of EDX technique used for composition measurement in this thesis is about 1%. Moreover, in case of a quite large sample with a gradient of composition, the mean value of composition is difficult to calculate since the EDX technique is sensitive to a very small area on the sample.
- Because of preferential Gd oxidation, the Gd composition in mean-field calculation can be smaller than the measured Gd composition. The oxidation would decrease the Gd contribution to magnetisation (GdO_x is most likely antiferromagnetic).

1.2.3. Magnetic coupling in the $Gd_{1-x}Co_x$ intermetallic alloys

The magnetic properties of the rare earth (R)-transition metal (T) compounds are determined by the large R-T exchange interactions. These interactions are thought to be caused by a combination of the intra-atomic 4f-5d and inter-atomic 5d-3d interactions. It is usual to express them as an effective exchange Hamiltonian in the form:

$$H_{exch} = -2A_{RT}S_R S_T \qquad \textbf{(1.4)}$$

where A_{RT} is the R-T exchange coupling parameter, S_R is the spin of the rare earth ion and S_T the quasi-spin of the transition metal atom [9].

By using high-field (up to 35 T) magnetisation measurements, F. R. de Boer et al have

specified the Gd-Co intersublattice molecular field coefficients in several ferrimagnetic materials, e.g. $CaCu_5$-type rare-earth cobalt compounds [10], $Gd_2Co_{14}B$ compound [11],... The composition dependences of the exchange coupling parameter (A_{GdCo}) for both crystal and amorphous $Gd_{1-x}Co_x$ alloys have been calculated by N.H. Duc et al (1996) in a series of publications ([12]-[14]) using earlier literature data. The results are presented on Fig. 1.6.

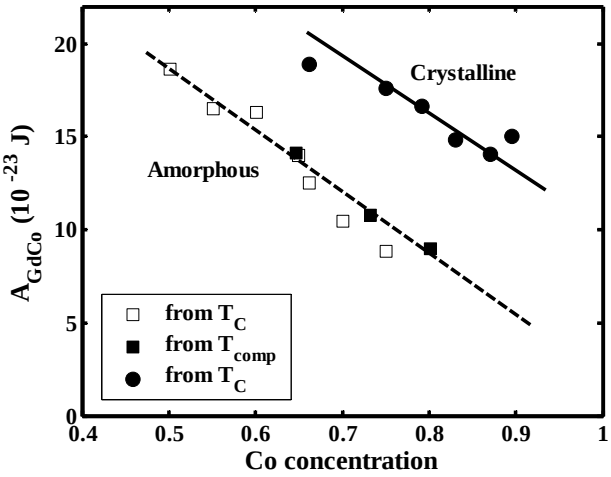

Fig. 1.6. The composition dependence of the exchange coupling parameter (A_{GdCo}) in the amorphous and crystalline $Gd_{1-x}Co_x$ alloys calculated by N. H. Duc et al (refs. [12]-[14]).

The value of the Gd-Co intersublattice molecular field coefficients (λ_{GdCo}) in $Gd_{1-x}Co_x$ can be derived from A_{GdCo} using the following relations:

$$\lambda_{GdCo} = \frac{Z_{GdCo}(g_{Co}-1)}{\mu_o g_{Co}\mu_B^2 xN} A_{GdCo} = \lambda_{CoGd} = \frac{Z_{CoGd}(g_{Gd}-1)}{\mu_o g_{Gd}\mu_B^2 (1-x)N} A_{CoGd} \qquad \textbf{(1.5)}$$

where Z_{GdCo} is the number of Co-nearest neighbours of one Gd atom and Z_{CoGd} is the number of Gd-nearest neighbours of one Co atom. They can be deduced from formulas: $Z_{GdCo} = (12+6x)x$ and $xZ_{CoGd} = (1-x)Z_{GdCo}$ (see ref.. [12]-[14]). Eventually, one finds:

$$\lambda = \lambda_{GdCo} = \lambda_{CoGd} = \frac{(12+6x)(g_{Co}-1)}{\mu_o g_{Co}\mu_B^2 N} A_{GdCo} \qquad \textbf{(1.6)}$$

The atomic densities N for crystalline and amorphous $Gd_{1-x}Co_x$ alloys depend on the composition and have been taken from refs. [4] and [15]. By using $g_{Gd} = 2$ (L = 0 for Gd) and $g_{Co} = 2$ (neglecting a small orbital contribution to magnetic moment), the values of λ_{GdCo} can be calculated and presented in Fig. 1.7.

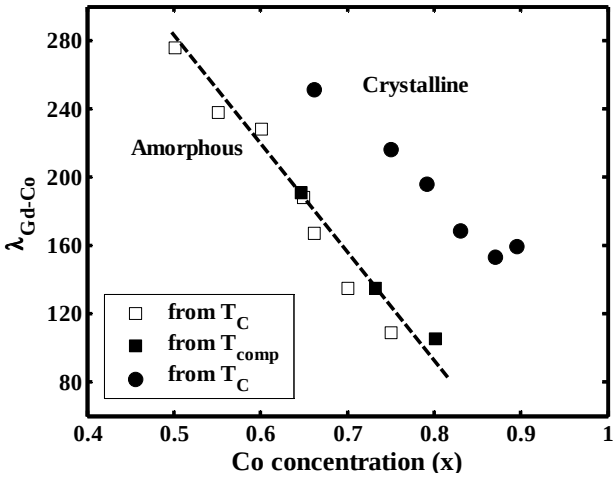

Fig. 1.7. The composition dependence of the Gd-Co intersublattic molecular field coefficient ($\lambda = \lambda_{GdCo}$) in the amorphous (open and solid squares) and crystalline (solid circles) $Gd_{1-x}Co_x$ alloys.

It is difficult to specify the real value of λ especially near x = 0.8. The causes may be that the accuracies of composition measurements in literature are different, therefore there is a distribution of the published λ for the same composition and same (amorphous or crystalline) structure. The rather large difference of λ between crystalline and amorphous alloys (Fig. 1.7) proves the important role of local geometrical structure with respect to the antiparallel interaction between the Gd and Co magnetic sublattices. For instance, it can be inferred from Fig. 1.7 that, when x = 0.8, λ is about 80 for an amorphous structure and 200 for a crystalline structure. If the sample is not completely amorphous, λ can be somewhere between 80 and 200.

1.3. Numerical simulation of magnetic behaviour of $Gd_{1-x}Co_x$ alloys

1.3.1. Theoretical magnetisation process of $Gd_{1-x}Co_x$ ferrimagnetic alloys

The general magnetisation process of $Gd_{1-x}Co_x$ ferrimagnetic alloys is sketched on Fig. 1.8. The ferrimagnetic saturation state can be achieved easily with an external magnetic field H_{S1} called the ferrimagnetic saturation field. In order to break the antiparallel configuration of the Gd and Co magnetic moments, the external magnetic field must overcome the spin-flop field H_{sf}. The amplitude of spin-flop field H_{sf} depends on (net) magnetisation and anisotropy of alloys. After spin-flop ($H > H_{sf}$), the magnetic configuration has to pass through an intermediate state when the Gd and Co sublattice magnetisations are not collinear to achieve the ferromagnetic saturation state where the two sublattice magnetisations are parallel to the applied field. The ferromagnetic saturation state of the $Gd_{1-x}Co_x$ alloys is reached when the applied field exceeds H_{S2} called the ferromagnetic saturation field.

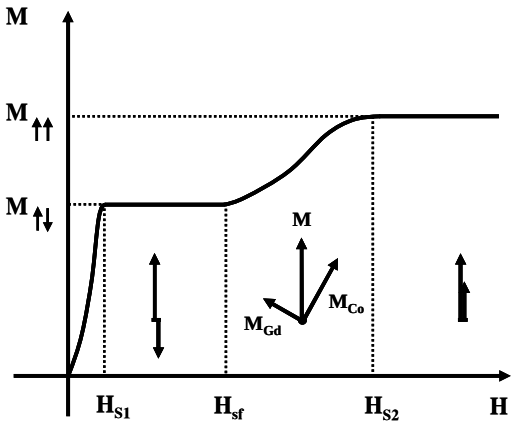

Fig. 1.8. General magnetisation process of $Gd_{1-x}Co_x$ ferrimagnetic material, where H_{S1}, H_{sf}, and H_{S2} are the ferrimagnetic saturation field, the spin-flop field, and the ferromagnetic saturation field, respectively.

The magnetisation process of $Gd_{1-x}Co_x$ alloys has been theoretically investigated by Radwansky et al in 1986 [16]. A mean-field calculation has been performed with the input parameters taken from literature. Theoretical values of the spin-flop field H_{sf} ($= \lambda|M_{Co} - M_{Gd}|$) and the ferromagnetic saturation field H_{S2} ($= \lambda|M_{Co} + M_{Gd}|$) have been estimated neglecting the anisotropy and the demagnetising energy.

In our opinion, anisotropy plays an important role in the magnetic behaviour of $Gd_{1-x}Co_x$ alloys, especially in the vicinity of compensation temperature (T_{comp}) where the total magnetisation is very small and Zeeman energy becomes comparable with anisotropy. On the other hand, when temperature is far from T_{comp}, the magnetisation becomes large, therefore the influence of demagnetising energy can not be neglected. In order to describe well the magnetisation process of $Gd_{1-x}Co_x$ alloys, these two factors (i.e. the anisotropy of Co sublattice and the demagnetising energy) will be taken into account in our mean-field theory developments.

1.3.2. The calculation model for magnetisation process of $Gd_{1-x}Co_x$ alloys

Fig. 1.9 shows three typical magnetic configurations of $Gd_{1-x}Co_x$ alloys in the whole magnetisation process. In low applied fields, the magnetic configuration of $Gd_{1-x}Co_x$ alloys is ferrimagnetic, and the total magnetic moment of sample is parallel to the dominant sublattice moment and antiparallel to the other (Fig. 1.9.a). In the intermediate state (Fig. 1.9.b), because of the dominance of Co sublattice anisotropy, the total magnetic moment is not anymore parallel to the applied field. Finally, when the applied field exceeds H_{S2}, both sublattice magnetic moments are parallel to the applied field, and the magnetic configuration becomes ferromagnetic as described in Fig. 1.9.c.

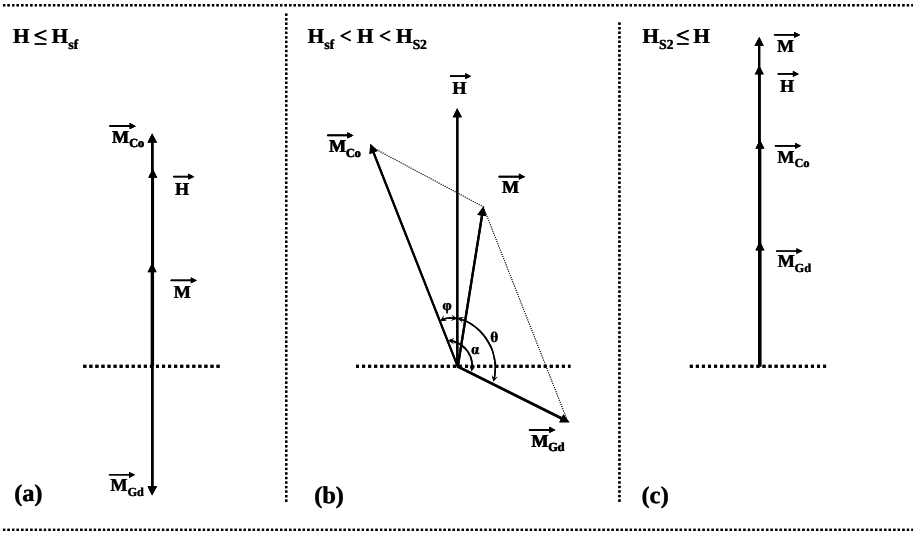

Fig. 1.9. The magnetic configuration of $Gd_{1-x}Co_x$ changes from ferrimagnetic configuration (a) to ferromagnetic configuration (c) via an intermediate configuration (b) under an applied magnetic field $\vec{H}$ parallel to the easy axis of Co sublattice. The angles θ and φ (θ, φ ∈ [0, π]) respectively describe the directions of Gd and Co sublattice magnetisations with respect to $\vec{H}$.

The free energy can be written as:

$$E = -\mu_o H M_{Co}\cos\varphi - \mu_o H M_{Gd}\cos\theta + \mu_o \lambda M_{Co} M_{Gd}\cos(\varphi+\theta) + K_{Co}\sin^2\varphi + \tfrac{1}{2}\mu_o\left(M_{Co}\cos\varphi + M_{Gd}\cos\theta\right)^2 \qquad (1.7)$$

where θ and φ are respectively the angles of Gd and Co sublattice magnetisations with respect to the applied field (see Fig. 1.9). K_{Co} is the first order anisotropy constant of Co sublattice. In the equation (1.7), the first and the second terms represent Zeeman energy, the third term is the intersublattice exchange energy, the fourth is the Co sublattice anisotropy energy, and the last term is the demagnetising energy. The anisotropy of Gd (L = 0 ion) sublattice is zero and not present in the equation. In order to calculate the critical fields of $Gd_{1-x}Co_x$ alloy, the problem is divided into two cases: $K_{Co} = 0$ and $K_{Co} > 0$.

a. When $K_{Co} = 0$ and the demagnetising energy is neglected (the calculation of Radwansky et al [16])

Because there is no anisotropy, the total magnetisation $\vec{M}$ is parallel to the applied field $\vec{H}$, and the free energy is:

$$E = -\mu_o H M + \mu_o \lambda M_{Co} M_{Gd}\cos\alpha \qquad (1.8)$$

$$= -\mu_o H\sqrt{M_{Co}^2 + M_{Gd}^2 + 2M_{Co}M_{Gd}\cos\alpha} + \mu_o\lambda M_{Co}M_{Gd}\cos\alpha$$

The equilibrium state is found by minimising the free energy with respect to α = (φ + θ).

$$\frac{dE}{d\alpha} = 0 \Leftrightarrow \left(\frac{H}{M} - \lambda\right)\sin\alpha = 0 \quad \textbf{(1.9)}$$

When $H < H_{sf}$: $\alpha = 0^{o}$, $\sin\alpha = 0$ and $M = |M_{Co} - M_{Gd}| \neq 0$.

When $H_{sf} < H < H_{s2}$: $0 < \alpha < 180^{o}$, $\sin\alpha > 0 \Rightarrow H/M = \lambda$

When $H > H_{S2}$: $\alpha = 180^{o}$, $\sin\alpha = 0$ and $M = M_{Co} + M_{Gd} \neq 0$.

At critical points $H = H_{sf}$ and $H = H_{S2}$, one can find:

$$H_{sf} = \lambda|M_{Co} - M_{Gd}| \quad \textbf{(1.10.a)}$$

$$H_{S2} = \lambda|M_{Co} + M_{Gd}| \quad \textbf{(1.10.b)}$$

At T_{comp}, the sublattice magnetisations compensate, therefore a conclusion can be inferred from equation (1.10.a) that: *In case of no anisotropy, the spin-flop field of $Gd_{1-x}Co_x$ alloys will be zero at the compensation temperature.*

b. When $K_{Co} \neq 0$ and the demagnetising energy is taken into account

The equilibrium state can be found by minimising equation (1.7) with respect to θ and φ, we find:

$$\frac{\partial E}{\partial\varphi} = \mu_o H M_{Co}\sin\varphi - \mu_o\lambda M_{Co}M_{Gd}\sin(\varphi+\theta) - \mu_o M_{Co}M_{Gd}\sin\varphi\cos\theta \quad \textbf{(1.11.a)}$$
$$+ (2K_{Co} - \mu_o M_{Co}^2)\sin\varphi\cos\varphi = 0$$

$$\frac{\partial E}{\partial\theta} = \mu_o H M_{Gd}\sin\theta - \mu_o\lambda M_{Co}M_{Gd}\sin(\varphi+\theta) - \mu_o M_{Co}M_{Gd}\cos\varphi\sin\theta \quad \textbf{(1.11.b)}$$
$$- (\mu_o M_{Gd}^2)\sin\theta\cos\theta = 0$$

The equations (1.11) have no analytical solution and must be solved by numerical methods. The Matlab computing program is used to find the two angles φ and θ as functions of the applied field and anisotropy (K_{Co}). H_{sf} and H_{S2} can be found by investigating the sum $\alpha = \varphi + \theta$. H_{sf} is the applied field where α start decreasing from 180^{o}, and H_{S2} is the applied field where α start increasing from zero.

1.3.3. The specimen for simulation: $Gd_{0.20}Co_{0.80}$ alloy

The $Gd_{0.20}Co_{0.80}$ alloy is chosen as a model material in our simulation for the following reasons: The composition of this alloy (x = 0.8) is close to the composition of $Gd_{1-x}Co_x$ alloys experimentally studied in this thesis. The available experimental parameters (N, T_C, T_{comp}, λ_{GdCo}) of $Gd_{1-x}Co_x$ crystalline compounds can be used to calculate the input parameters (λ, λ_{CoCo}) in the mean-field calculation for $Gd_{0.20}Co_{0.80}$ alloy:

$J_{Co} = 0.84$, $g_{Co} = 2 \Rightarrow \mu_{Co} = 1.68\mu_B = 1.5580\times10^{-23}$ Am^2.

$J_{Gd} = 3.5$, $g_{Gd} = 2 \Rightarrow \mu_{Gd} = 7\mu_B = 6.4890\times10^{-23}$ Am^2.

The atom density of $Gd_{0.20}Co_{0.80}$ can be deduced from its mass density $D(GdCo_4)$ = 8.50×10^6 g/m^3 [15], we find: $N(Gd_{0.20}Co_{0.80}) = 6.51\times10^{28}$ at/m^3.

$M_{Co} = 4N\mu_{Co}/5 = 8.12\times10^5$ A/m and $M_{Gd} = N\mu_{Gd}/5 = 8.46\times10^5$ A/m.

The intersublattice molecular field coefficient for $Gd_{0.20}Co_{0.80}$ can be taken from Fig. 1.7 for crystallised alloys (x = 0.8): $\lambda = 190$.

The Curie temperature of $Gd_{0.20}Co_{0.80}$ from Fig. 1.5 is about T_C = 900 K, this T_C corresponds to the Co-Co intrasublattice molecular field coefficient: $\lambda_{CoCo} = 900$.

Neglecting the Gd-Gd interaction, the mean-field theory has been applied using the parameters listed above to calculate the temperature dependence of the sublattice magnetisations and the total magnetisation of the $Gd_{0.20}Co_{0.80}$ alloy. The calculated results are presented in Fig. 1.10.

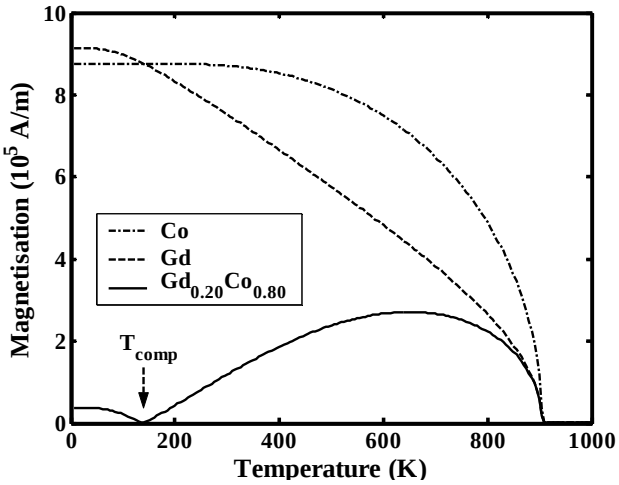

Fig. 1.10. Temperature dependence of the spontaneous magnetisation of $Gd_{0.20}Co_{0.80}$ alloy (solid curve) calculated by the mean-field theory when the Gd-Gd interaction is neglected.

A compensation temperature T_{comp} = 128 K is obtained. This T_{comp} quite agrees with literature data for $Gd_{0.20}Co_{0.80}$ alloy in Fig. 1.4. These results will be used to calculate the critical fields (H_{sf} and H_{S2}) for both cases with and without anisotropy.

1.3.4. The critical fields (H_{sf}, H_{S2})

a. The critical fields (H_{sf}, H_{S2}) of $Gd_{0.20}Co_{0.80}$ in case of no anisotropy

The calculated critical fields (H_{sf} and H_{S2}) of the $Gd_{0.20}Co_{0.80}$ alloy in the case of no anisotropy are shown on Fig. 1.11. Below room temperature, the ferromagnetic saturation field B_{S2} is several hundred Tesla, therefore, the ferromagnetic saturation state of $Gd_{0.20}Co_{0.80}$ cannot be experimentally reached.

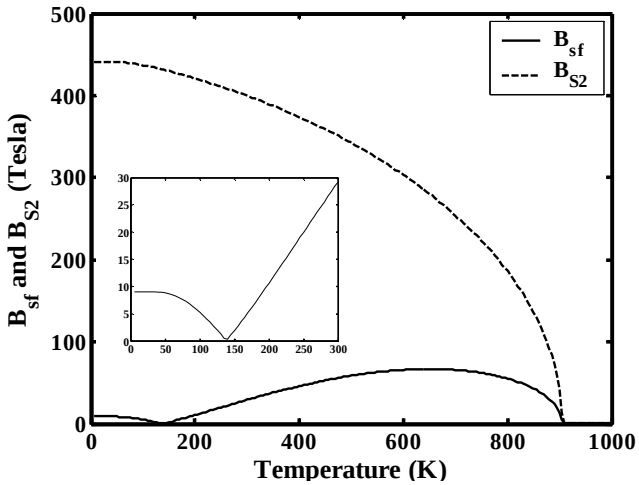

Fig. 1.11. Temperature dependences of the spin-flop field ($B_{sf} = \mu_o H_{sf}$) and the ferromagnetic saturation field ($B_{S2} = \mu_o H_{S2}$) of $Gd_{0.20}Co_{0.80}$ alloy calculated using formula (1.10) taking the demagnetising energy into account. The anisotropy is neglected ($K_{Co} = 0$). The insert is B_{sf} zoomed close to $T_{comp} = 128$ K.

However, the spin-flop field decreases significantly near T_{comp} and gets to zero at T_{comp}. This characteristic (with K = 0) enables us to observe the spin-flop of $Gd_{0.20}Co_{0.80}$ in vicinity of T_{comp} using the fields available in the laboratory. At temperatures far from T_{comp}, the B_{sf} increases very quickly to several tens Tesla, that is why there has been no study which observed the spin-flop field in $Gd_{1-x}Co_x$ alloys except a very recent study of Kuz'min et al (2006) on a $GdCo_5$ single crystal.

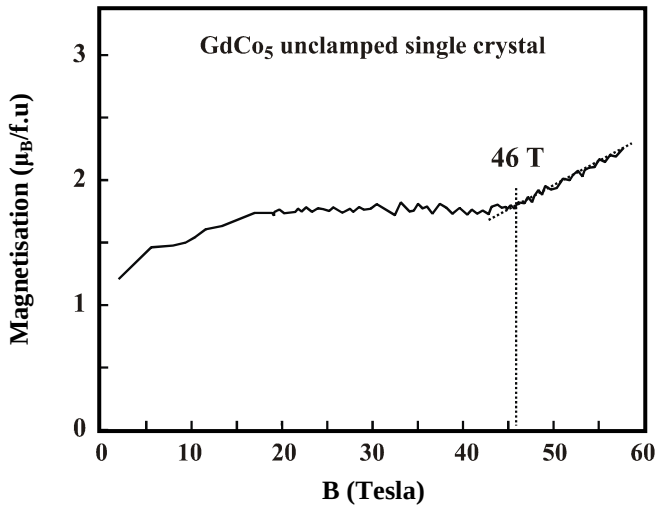

Fig. 1.12. The magnetisation curve at 5 K of an unclamped single crystal of a $GdCo_5$ in a pulsed magnetic field published in ref. [17], $B_{sf} = 46 \pm 1$ Tesla.

In their work, Kuz'min et al [17] undertook a high-field magnetisation study of a single crystal of $GdCo_5$ (x = 0.83, its magnetisation is Co-dominant at all temperatures, i.e. T_{comp} does

not exist) in magnetic fields up to 60 Tesla. The anisotropy of the Gd sublattice is negligible. In order to eliminate the influence of the strong magnetic anisotropy of Co, the sample was shaped as a sphere and could freely orientate itself in space. In this way it was achieved that, during the magnetising process, while the total magnetic moment was directed along the applied field, the moment of the Co sublattice remained parallel to its easy-axis [001] even after spin-flop. The system is equivalent to an isotropic ferrimagnet and the magnetising process is similar to the case of zero anisotropy. The result presented in Fig. 1.12 lets one know that the spin-flop field of $GdCo_5$ crystal is B_{sf} = 46 ± 1 Tesla. So far, this is the unique measured value of B_{sf} in $Gd_{1-x}Co_x$ alloys and compounds.

The intersublattice molecular field coefficient λ of $Gd_{1-x}Co_x$ alloys can be calculated if the spin-flop field is known. For instance, the spin-flop field of $GdCo_5$ crystal is B_{sf} = 46 ± 1 Tesla. The measured spontaneous moment of $GdCo_5$ in ref. [17] is μ = (1.72 ± 0.05) μ_B/f.u. The mass density of $GdCo_5$ crystal is D = 8.80×10^6 g/m^3 [15], we find the corresponding atom density of $GdCo_5$ crystal N = $6N_AD/451.92 = 7.04\times10^{28}$ at/m^3. Finally, by using equation (1.10.a), we find the intersublattic molecular field coefficient of $GdCo_5$ crystal: $\lambda(GdCo_5) = 6B_{sf}/(\mu_o\mu N)$ = 195 ± 10.

b. The influence of anisotropy on the spin-flop field (H_{sf})

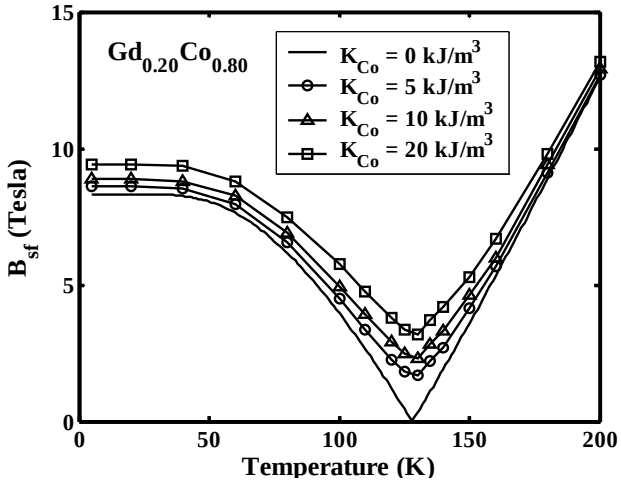

Fig. 1.13. The K_{Co} dependence of the spin-flop field (B_{sf}) calculated for $Gd_{0.20}Co_{0.80}$ alloy. The applied field is parallel to the easy axis of the sample.

In order to evaluate the role of anisotropy in the magnetisation process, in our simulation the anisotropy K_{Co} is varied from 0 kJ/m^3 to 20 kJ/m^3, This range of K_{Co} agrees well with the perpendicular anisotropy of sputtered amorphous $Gd_{1-x}Co_x$ thin films published in refs. [5] and [18]. The calculated K_{Co} dependence of B_{sf} is shown in Fig. 1.13. The applied field is still parallel to the easy axis of sample (it is likewise the easy axis of Co sublattice). The obtained results prove that the anisotropy K_{Co} strongly influences the spin-flop of $Gd_{1-x}Co_x$,

especially in the vicinity of T_{comp}. At T_{comp}, the spin-flop field is not zero anymore if the anisotropy is taken into calculation.

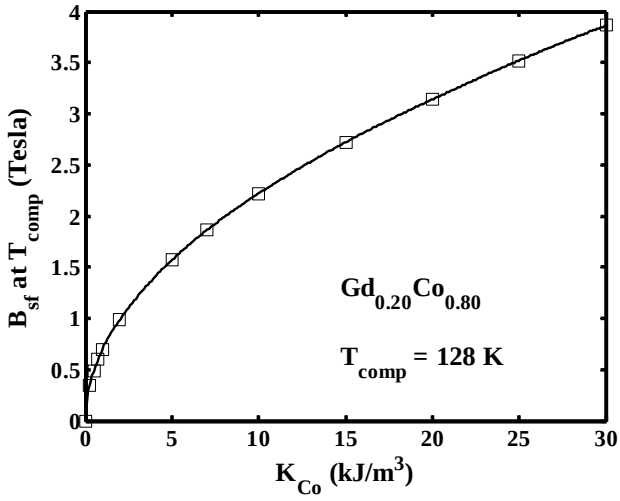

Fig. 1.14. The K_{Co} dependence of the spin-flop field (B_{sf}) of $Gd_{0.20}Co_{0.80}$ alloy at T_{comp} = 128 K. The applied field is parallel to the easy axis of the sample.

The value of B_{sf} at T_{comp} as a function of K_{Co} is presented in Fig. 1.14. We can see that the larger the anisotropy is, the larger the spin-flop field at T_{comp} is.

1.3.5. Rotations of the Gd and Co sublattice magnetisations in magnetisation process of $Gd_{1-x}Co_x$ alloys

a. In the case of no anisotropy (K_{Co} = 0)

In the case of no anisotropy, whatever the direction of applied field is, the total magnetisation is always parallel to the applied field. After spin-flop, the antiferromagnetic configuration is broken, so the angle α between Gd and Co moments is not 180° anymore, i.e. the Gd and Co sublattice magnetisations are no longer collinear.

The rotation of the Gd and Co magnetisations of $Gd_{0.20}Co_{0.80}$ alloy at 5 K under an applied field is shown in Fig. 1.15. Although the slopes of φ(B) and θ(B) curves are very large right after spin-flop, the slope of α(B) curve is small. The change of the total angle α (= φ + θ) when the applied field varies from 0 T to 30 T is smaller than 10°. It means that the net magnetisation of $Gd_{0.20}Co_{0.80}$ alloy changes very little below 30 T even when the spin-flop occurs, therefore the spin-flop phenomenon is quite difficult to observe with conventional magnetometers (VSM, SQUID).

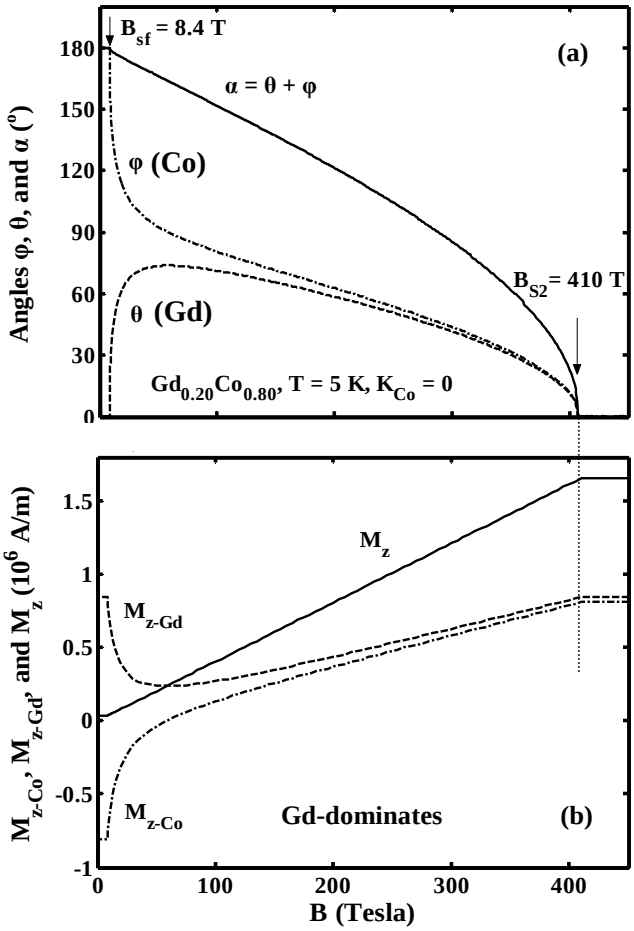

Fig. 1.15. (a) The rotations of the Gd and Co magnetisations from the applied field direction, and (b) the field dependences of the projection of sublattice magnetisations on the applied field direction (z-components) during the magnetisation process at 5 K. Because of zero anisotropy, the total magnetisation is parallel to the applied field ($M_z = M$).

On the opposite, since the angles φ and θ vary rapidly right after spin-flop, i.e. the directions of Gd and Co magnetisations rotate rapidly, it is easy to observe the magnetic structure and the spin-flop phenomenon with the polar Kerr imaging and the extraordinary Hall effect, which are very sensitive to the direction of magnetisation of the Co sublattice. These observation techniques will be explained later in detail.

b. The influence of anisotropy on the rotation of sublattice magnetisations

Assuming that the external magnetic field is applied parallel to the easy axis of the sample, in the intermediate state (when $B_{sf} \leq B \leq B_{S2}$) the sublattice magnetisations are not parallel to the applied field. The angles φ and θ depend not only on the amplitude of the applied field but also the anisotropy. Nevertheless, the main difference compared to the case of $K_{Co} = 0$ happens in low fields near the spin-flop field B_{sf}. For example, below 20 T, the moment

rotations in two cases K_{Co} = 0 and K_{Co} = 20 kJ/m^3 quite deviate from each other, but they coincide above 20 T (see the solid and dash curves in Fig. 1.16).

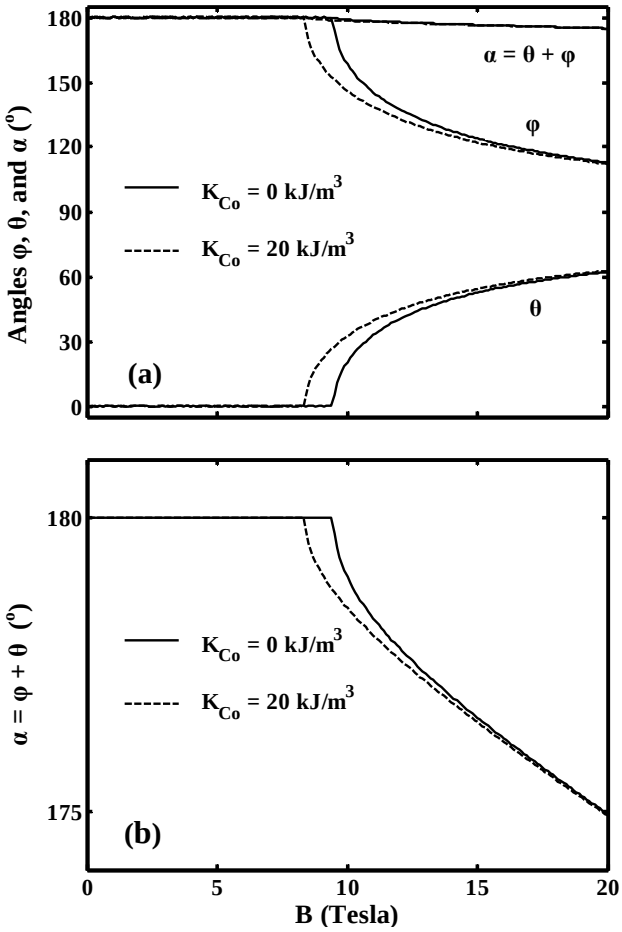

Fig. 1.16. The rotations of Gd and Co magnetisations from the direction of applied field, and (b) the field dependence of α (= θ + φ) calculated at 5 K for two cases: K_{Co} = 0 (dash lines) and K_{Co} = 2 kJ/m^3 (solid lines). The applied field is parallel to the easy axis of sample. Above 20 T, both rotations coincide.

Additionally, during rotation, because of the Co-dominant anisotropy, the Co magnetisation is more difficult to rotate from the easy axis than the Gd one (K_{Gd} = 0), therefore, the total magnetisation is not parallel to the applied field. The deviation of the total magnetisation from the direction of applied field makes a difference between total magnetisation M and its projection M_z on the direction of applied field as shown in Fig. 1.17. We can see that the larger K_{Co} is, the more tilted from the applied field's direction the magnetisation is. When K_{Co} = 20 kJ/m^3, M and M_z curves almost coincide. The deviation just happens in the range of applied field near spin-flop field. For example, when K = 500 kJ/m^3, above 30 T, the curves of M and M_z are superimposed.

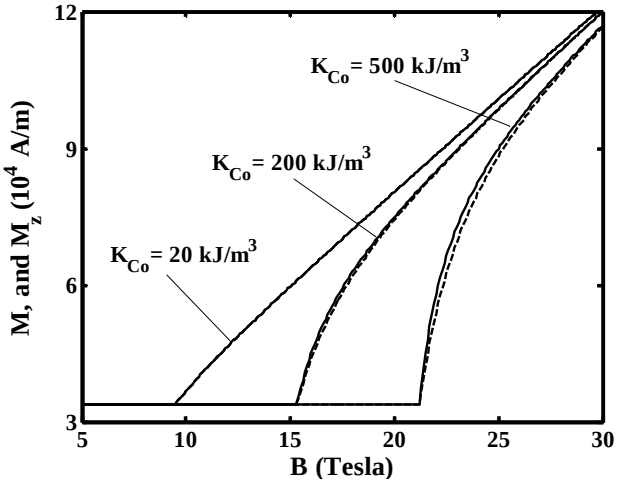

Fig. 1.17. The total magnetisation M (three solid lines) and its projection M_z on the direction of applied field (three dash lines) calculated at 5 K for three cases: K_{Co} = 20 kJ/m^3, K_{Co} = 200 kJ/m^3, and K_{Co} = 500 kJ/m^3. The applied field is parallel to the easy axis of sample.

Because, the anisotropies of amorphous $Gd_{1-x}Co_x$ alloys are below 100 kJ/m^3 (see refs. [17] and [19]), the directional deviation between magnetisation and applied field is very small and can be neglected. That is why, in calculation for amorphous $Gd_{1-x}Co_x$ alloys, the total magnetisation can be considered parallel to the applied field ($M = M_z$).

1.4. The extraordinary Hall effect (EHE) in amorphous $Gd_{1-x}Co_x$ alloys

1.4.1. Introduction of Hall effects

a. The ordinary Hall effect (OHE)

Consider a rectangular plate with a thickness t, carrying a current $\overrightarrow{I_X}$ (i.e. a current density $\overrightarrow{J_X}$) along the length of the plate, with a field $\vec{B}$ perpendicular to the plate (Fig. 1.18). A carrier (electron or hole) moves with average velocity $\overrightarrow{v_X}$, and is subject to the Lorentz force. This force deviates the carriers in the y direction, resulting in an accumulation of charge on the lateral faces. A Hall voltage V_H appears between the faces such that the resulting electric field $\overrightarrow{E_H}$ compensates the Lorentz force. If n is the volume concentration of carriers, the transverse electric field at the equilibrium state is calculated to be $E_H = B_z J_x/nq$. So the Hall effect is sensitive to the component of magnetic field perpendicular to the plane containing the Hall contacts and the current. It is an odd function of the applied field, with hysteresis in a magnetic material. The ordinary Hall resistivity, $\rho_H = E_H/J_x = R_H B_z$, is proportional to the field, with the slope defining the Hall coefficient:

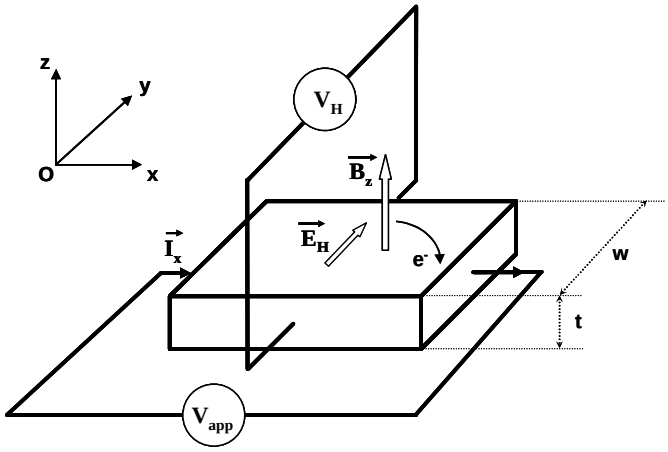

Fig. 1.18. Geometry of the Hall voltage measurement where I_x is the applied current, E_H is the Hall electric field, and B_z is the external magnetic field.

$$R_H = \frac{E_H}{J_x B_z} = \frac{V_H t}{I_x B_z} = \frac{1}{nq} \qquad \textbf{(1.12)}$$

This coefficient is negative for electrons ($q = -e = -1.6\times10^{-19}$ C), and positive for holes ($q = +e$), and is expressed in Ωm/T or equivalently in m^3/C. If B is known, OHE is used to characterise carriers (sign and density). If n is known, it is used as a field sensor.

b. The planar Hall effect (PHE) in magnetic materials

In case of a magnetic conductor when the magnetic field is parallel to the contacts-current plane (i.e. the plate), a component of electric field can exist within the plate, perpendicular to the current. This is called the planar Hall effect and it is related to the anisotropy of the magnetoresistance, i.e. the anisotropic magnetoresistance (see section 5.3.2), in a magnetic conductor (refs. [20] and [21]). In applications, the planar Hall effect can be used to make magnetic field sensors (refs. [22] and [23]). The origin of the planar Hall effect is interpreted in Fig. 1.19. In the saturation state of a magnetic conductor, the magnetisation $\vec{M}$ is parallel to the applied field $\vec{B}$ and makes an angle φ with the applied current density $\vec{J}$. The applied current density can be represented as $\vec{J} = \vec{J}_{//} + \vec{J}_{\perp}$ where $\vec{J}_{//}$ and $\vec{J}_{\perp}$ are respectively the current densities in two in-plane directions perpendicular and parallel to the direction of magnetisation $\vec{M}$. The corresponding electric fields are $\vec{E}_{//} = \rho_{//}\vec{J}_{//}$ and $\vec{E}_{\perp} = \rho_{\perp}\vec{J}_{\perp}$ where $\rho_{//}$ and $\rho_{\perp}$ are the resistivities along both directions.

Because of the anisotropic magnetoresistance, the resistivities parallel and perpendicular to magnetisation are different ($\frac{\rho_{//}-\rho_{\perp}}{\rho_{//}+\rho_{\perp}} \sim \pm 1\%$), therefore, the total electric field $\vec{E} = \vec{E}_{//} + \vec{E}_{\perp}$ is not parallel to the applied current density $\vec{J}$. The Planar Hall voltage is

measured in the direction perpendicular to the applied current. The amplitude of the planar Hall electric field $\overrightarrow{E_{PH}}$ can be calculated as:

$$E_{PH} = E_{//}\sin\varphi - E_{\perp}\cos\varphi = \frac{J_{//}}{\rho_{//}}\sin\varphi - \frac{J_{\perp}}{\rho_{\perp}}\cos\varphi = J\cos\varphi\sin\varphi\frac{\rho_{\perp}-\rho_{//}}{\rho_{//}\rho_{\perp}} \qquad \textbf{(1.13)}$$

and the planar Hall resistivity can be found as:

$$\rho_{PH} = \frac{E_{PH}}{J} = \frac{\rho_{\perp}-\rho_{//}}{2\rho_{//}\rho_{\perp}}\sin 2\varphi \qquad \textbf{(1.14)}$$

In case of no anisotropic magnetoresistance ($\rho_{//} = \rho_{\perp}$) or when the magnetisation is perpendicular to the plate, the planar Hall effect is zero. The maximum planar Hall effect is obtained when the angle between magnetisation and current) is 45°. It is zero when the magnetisation is parallel or perpendicular to the current.

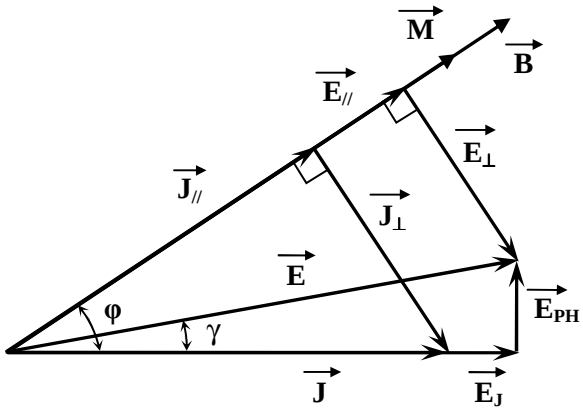

Fig. 1.19. The origin of the planar Hall effect in a magnetic material.

Notice that the planar Hall effect is an even function of the applied field. When the direction of the applied field is reversed, the planar Hall voltage is not changed. Even if it is called Hall, it is a magnetoresistance effect.

c. The extraordinary Hall effect (EHE) in magnetic materials

Let us now come back to the measurement configuration presented in Fig. 1.18 where the applied field is perpendicular to the plate of a magnetic conductor. In this case, because of the influence of a very strong internal magnetic field and the magnetic scattering centers inside the magnetic material, a new Hall effect appears called the extraordinary Hall effect (EHE), it is very different from OHE in magnitude as well as in mechanism. Since most ferromagnetic materials are metals, OHE is still present but it has usually a smaller amplitude than EHE.

Hall is the first person who studied the Hall effect in a magnetic material (Fe foil) in 1880 [24]. His name was later used to name the effect. He found that the Hall coefficient of Fe is about ten times larger than that of Au or Ag and of opposite sign. In 1881, he proceeded to

research on Ni and Co and then stated an important feature of the Hall effect of ferromagnets [25]: *the Hall voltage is not proportional to the external field B. Instead, it tends to become constant at field values comparable to those where magnetisation itself saturates*. The similar measurements made by A. W. Smith and R. W. Sears [32] for Ni are reproduced in Fig. 1.20. Before saturation, the Hall voltage depends on the magnetisation rather than on the applied field. When the magnetic saturation state is achieved or all the domains have been aligned with the direction of the applied field, the magnetisation is almost constant. The Hall voltage continues to increase following the increase of the applied field, but more slowly than its low field variation.

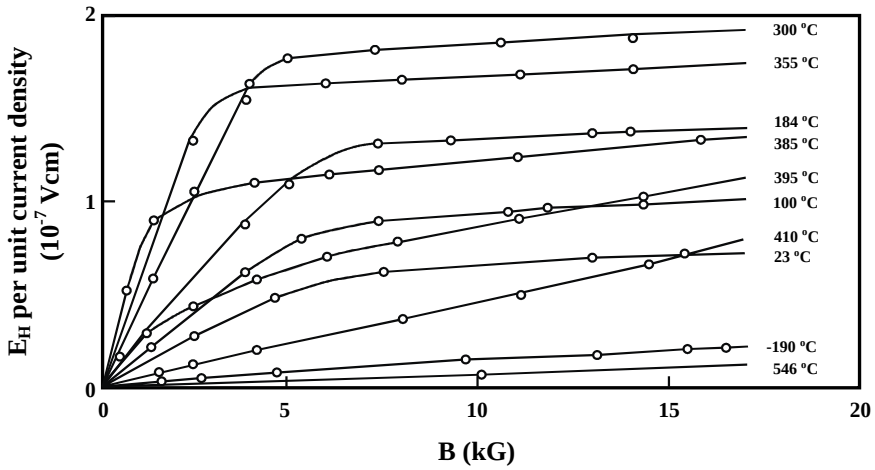

Fig. 1.20. The Hall effect in Ni published by A. W. Smith and R. W. Sears in ref. [32].

In every case of ferromagnetic metallic alloys studied after that time, the Hall effect consists of a sum of two terms [33]. The first term is proportional to the magnetising field and has been called the ordinary Hall effect (OHE). Its order of magnitude and sensitivity variations in temperature and in composition are comparable with the Hall effect in non-ferromagnetic metals. The second term is proportional to magnetisation and has been called the extraordinary Hall effect (EHE). The Hall resistivity of magnetic elements and alloys can be represented as:

$$\rho_H = R_o \mu_o H + R_s \mu_o M \qquad \textbf{(1.15)}$$

Where H, M, R_o and R_s are the applied field, the magnetisation of the sample, the ordinary Hall coefficient, and the extraordinary Hall coefficients, respectively [30]. In terms of magnitude, the extraordinary coefficient R_s is usually at least one order larger than the ordinary coefficient R_o (1/nq). In case of metallic magnetic compound, different from the case of semiconductor, the density of conduction electrons n is very large, R_o becomes very small and can be neglected, that is why in the rest of this thesis, we sometimes leave aside the ordinary Hall effect, in order to concentrate on the truly magnetic part of the effect.

1.4.2. The mechanism of extraordinary Hall effect

Two different types of scattering events have been proposed to be the microscopic origins of EHE [30]. One is referred to as "skew scattering" and is characterised by a constant spontaneous angle θ_S at which the scattered carriers are deflected from their original trajectories. The predicted correlation between the skew scattering Hall resistivity (ρ_H^{skew}) and the longitudinal resistivity (ρ) is: $\rho_H^{skew} = A\rho + B\rho^2$ where ρ is measured in zero applied field. The second term is frequently neglected and a linear ratio between ρ_H^{skew} and ρ is mentioned (refs. [28], [30], and [45]). The other scattering mechanism, so-called "side-jump", is quantum mechanical in nature and results in a constant lateral displacement Δy of the charge's trajectory at the point of scattering. For the side-jump mechanism: $\rho_H^{side-jump} = C\rho^2$ [29].

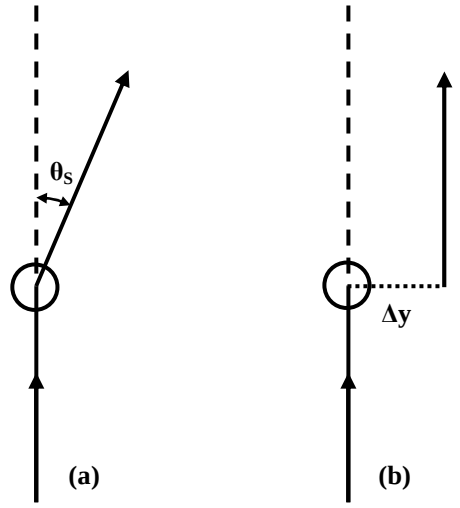

Fig. 1.21. Comparison of skew scattering (a) characterised by Hall angle θ_S and side-jump characterised by a constant lateral displacement Δy of carrier trajectory.

Because the ρ-dependences of both mechanisms are different, one may try to separate them. The EHE is usually attributed to the skew scattering when ρ is small (low temperatures and/or pure metals) and to the side-jump when ρ is large (high temperatures, concentrated alloys, and disordered materials). Superposition of the two mechanisms is represented as:

$$\rho_H = a\rho + b\rho^2 \qquad \textbf{(1.16)}$$

where a and b are constants. The first term is believed to relate to the skew scattering and the second term relates to the side-jump mechanism with a possible contribution of the skew scattering as well. A simplified alternative form of presentation is:

$$\rho_H = \alpha\rho^n \qquad \textbf{(1.17)}$$

with n = 1 corresponding to skew scattering, n = 2 to the side-jump, and intermediate values 1 < n < 2 accepted as a superposition of both mechanisms. For example, in case of Ni (n = 1.5) both skew scattering and side-jump are present, while there is only side-jump (n = 2) present in cases of Fe and Gd [30].

1.4.3. The extraordinary Hall effect in $Gd_{1-x}Co_x$ ferrimagnetic materials

Different from a ferromagnet, in a ferrimagnet there are two magnetic sublattices with different contributions to the extraordinary Hall effect. $Gd_{1-x}Co_x$ is the first rare-earth amorphous alloy in which the extraordinary Hall effect was studied. Experiments on $Gd_{1-x}Co_x$ were stimulated by the proposed use of this material for bubble domain devices [42]. In $Gd_{1-x}Co_x$, the complexity caused by two interacting magnetic ions gave rise to several models to explain the Hall behaviour.

The first papers on the Hall effect in $Gd_{1-x}Co_x$ alloys were those of Ogawa et al (1974), and Okamoto et al (1974), which assign a dominant role to only one sublattice in describing the temperature dependence of the Hall effect.

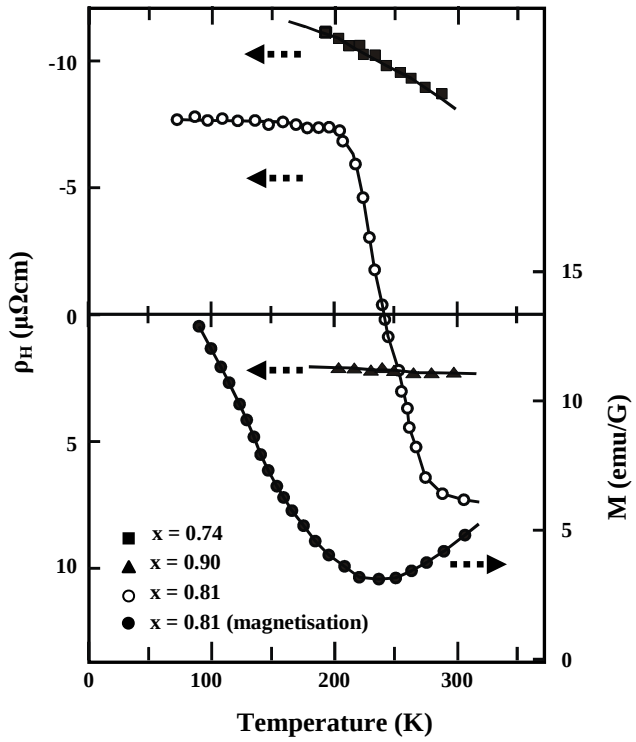

Fig. 1.22. The Hall resistivity of sputtered $Gd_{1-x}Co_x$ films and the magnetisation of a $Gd_{0.19}Co_{0.81}$ film as a function of temperature (Ogawa et al 1976 [39]).

Ogawa et al (see ref. [34] and [39]) assigned the sign of Hall resistivity (ρ_H) to Gd moment alone. They supposed that Gd contribution to the Hall effect is negative. Below T_{comp}, the Gd moments are parallel to the applied field, so they make a negative Hall effect. On the

contrary, above T_{comp}, the Gd moments are antiparallel to the applied field, therefore the signe of the Hall effect is positive. This model was based on the observation that the magnitude of ρ_H does not depend on the magnetisation of the sample but varies in proportion to the amount of Gd present in the $Gd_{1-x}Co_x$ alloys. When x decreases, the absolute value of ρ_H increases as illustrated for three compositions in Fig. 1.22.

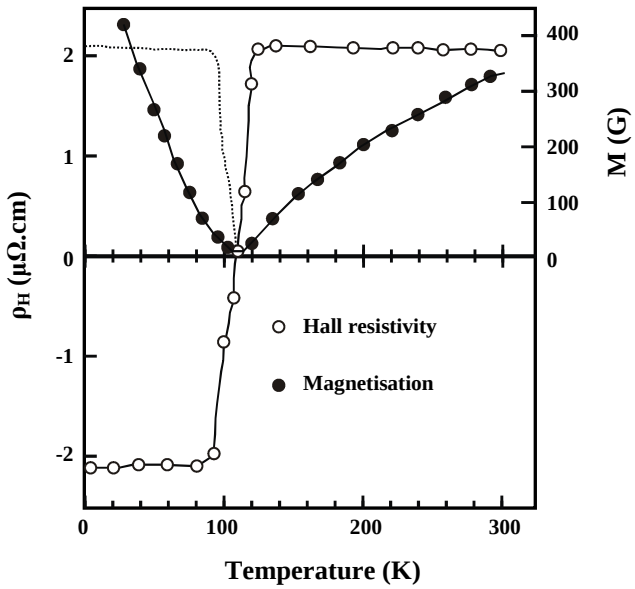

Fig. 1.23. Temperature dependence of magnetisation and Hall resistivity of a sputtered $Gd_{17}Co_{83}$ film (Shirakawa et al 1976 [36]).

In contrary, Okamoto et al [35], and later Shirakawa et al (1976) [36] assign a dominant role to the Co moment. The parallel-to-field Co moment (above T_{comp}) makes a positive Hall effect, and the antiparallel-to-field Co moment (below T_{comp}) gives a negative Hall effect. This interpretation came about because the temperature dependence of ρ_H and the Kerr magneto-optic rotation are similar. It was known from previous work that the main contribution to the Kerr effect is Co and not Gd. The typical result from Shirakawa for $Gd_{17}Co_{83}$ is shown in Fig. 1.23 with T_{comp} = 100 K illustrating the sharp change in sign for the Hall voltage at T_{comp} [36]. This reversal of Hall effect is attributed to the reversal of Co moment from antiparallel-to-field to parallel-to-field at T_{comp}. In this case, however, the saturation value of Hall resistivity is quite small, ρ_H = 2 μΩ.cm in comparison with previous data (Fig. 1.22).

In 1976, Asomoza et al [37] carried out a research on the extraordinary Hall effect of RCo_3 thin films, where R is rare-earth element. Those alloys include $GdCo_3$ with T_{comp} somewhere between 173 K and 263 K. This T_{comp} is different from the data of Hansen (ref. [4], page 368: T_{comp} = 400K for amorphous $GdCo_3$ alloy, and the $GdCo_3$ crystal is Gd-dominant at all temperatures). This difference may be attributed to the error of composition determination.

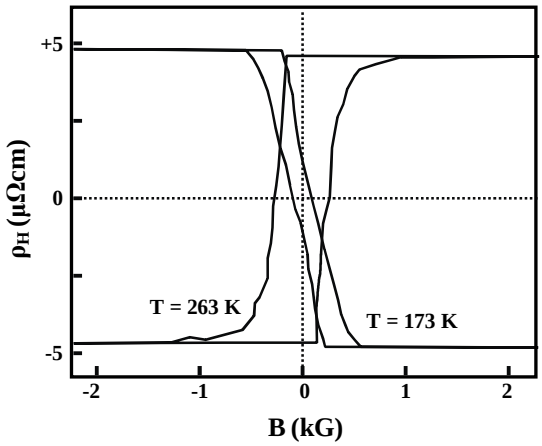

Fig. 1.24. Hall resistivity of $GdCo_3$ from Asomoza et al [37].

The Hall resistivity here is ρ_H = 5 μΩ.cm for amorphous $GdCo_3$ alloys. The research confirmed the sign reversal of Hall effect at T_{comp} (see Fig. 1.24) and contributed a conclusion that it is only the Co which contributes to ρ_H in $GdCo_3$ and other RCo_3 alloys. These results showed that the Hall resistivity is practically the same whether the R is magnetic (Gd, Er, Ho) or nonmagnetic (Y). Moreover, the replacement of Co by Ni makes the Hall resistivity decrease (see Fig. 1.25).

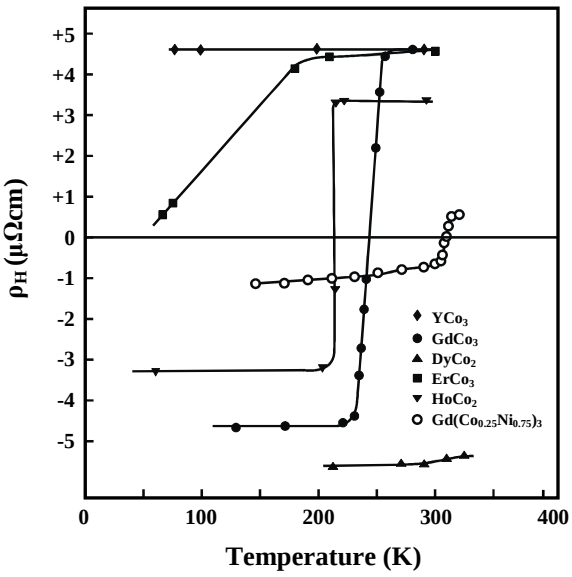

Fig. 1.25. The saturation Hall resistivity as a function of temperature for various RCo_3 and $Gd(Co_{0.25}Ni_{0.75})_3$ sample imported from Asomoza et al [37].

In 1977, McGuire et al [40] reported that the Hall effect in amorphous $Gd_{1-x}Co_x$ ferrimagnetic thin films is associated with both the Gd sublattice and the Co sublattice. They studied the Hall effect in the amorphous ternary ferrimagnets GdCoMo and GdCoAu, which exhibit compensation temperatures (T_{comp}). Similar to publications earlier, above T_{comp} the Hall

coefficient R_s (see formula (1.15)) is positive, and reverses below T_{comp}. The sign of R_S was attributed to the combined effect of a negative Gd Hall coefficient and a positive Co one as presented in Fig. 1.26. At temperatures below T_{comp}, the parallel-to-field Gd magnetic moments are associated with a negative Hall scattering. However, above T_{comp}, the Gd moments are now antiparallel-to-field and their Hall voltage reverses. The same analysis can be made for the Co moments except the parallel-to-field Co moments have a positive Hall coefficient to the Gd coefficient. Their Hall effects should add together in both T ranges as illustrated in Fig. 1.26.

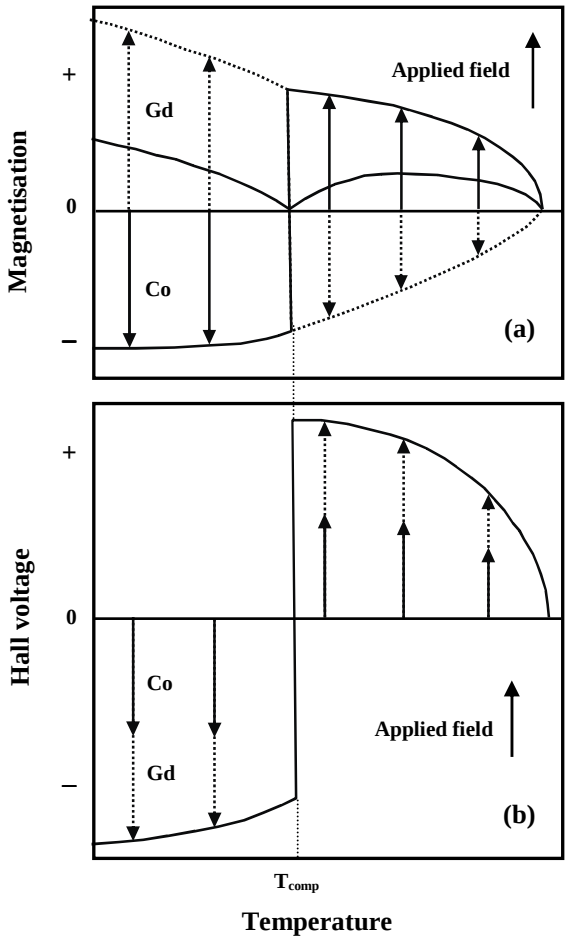

Fig. 1.26. Schematic diagrams of magnetisation (a) and Hall voltage (b) versus temperature for a two-sublattices system (imported from McGuire et al [40]).

So far, most publications on the extraordinary Hall effect of RT systems (R = rare earth elements as Tb, Gd,… and T = transition metals as Co, Fe, Ni) prove the dominant role of transition metal on the extraordinary Hall effect. Mimura et al (1976) investigated the strong effect of Ni in Gd-Ni alloys and suggested the transition metal plays the more important role [38]. In 1983, R. Malmhäll carried out a study on the extraordinary Hall effect of several TbFe alloys and attributed the dominant role to Fe sublattice [43].

In short, the Hall resistivity for $Gd_{1-x}Co_x$ can be written as:

$$\rho_H = \mu_o R_o H + \mu_o R_{Gd} M_{Gd} + \mu_o R_{Co} M_{Co} \quad \textbf{(1.18)}$$

where M_{Gd} and M_{Co} are respectively the Gd and Co sublattice magnetisations. The corresponding extraordinary Hall coefficients are R_{Gd} and R_{Co}. Because $R_{Gd} < 0$ and $R_{Co} > 0$, and $\overrightarrow{M_{Gd}}$ and $\overrightarrow{M_{Co}}$ are antiparallel, the contributions of Gd and Co moments to EHE have the same sign but their amplitudes are still open to discussion.

1.5. Conclusion

1.5.1. About magnetic behaviour of $Gd_{1-x}Co_x$

Although there were many studies about magnetic properties of $Gd_{1-x}Co_x$ alloys, they have always been performed in low fields. That is why no one has done any research on the spin-flop and the spin reorientation process of $Gd_{1-x}Co_x$ magnetisation except for the unique research of Kuz'min et al [17] on the spin-flop of $GdCo_5$ crystal (just a magnetic study, no transport, and not a film) performed with pulsed magnetic fields.

Our mean-field calculations show that the anisotropy has a strong influence on the spin-flop field and the magnetisation process of $Gd_{1-x}Co_x$ alloys in vicinity of T_{comp}. Moreover, near T_{comp}, the spin-flop field decreases significantly and gets a minimum value at T_{comp}. Using high fields above the spin-flop field, we can obtain more information about anisotropy and the exchange interaction between Gd and Co moments in our $Gd_{1-x}Co_x$ films.

1.5.2. About the extraordinary Hall effect of $Gd_{1-x}Co_x$

Although there have been many studies on the extraordinary Hall effect of $Gd_{1-x}Co_x$ alloys, the relative orders of magnitudes of both R_{Co} and R_{Gd} are still open questions.

Mean-field calculation shows that, after spin-flop the sublattice magnetisations are not collinear any more and rotate from the direction of applied field in different manners. Therefore, the behaviour of extraordinary Hall effect can be very interesting after spin-flop. Since all studies about the extraordinary Hall effect of $Gd_{1-x}Co_x$ alloys have been performed in low magnetic fields smaller than the spin-flop field, and all theoretical studies which mention the spin-flop phenomenon just concentrate on the magnetic properties of alloys, we can use the spin-flop to get new information about the EHE behaviour of $Gd_{1-x}Co_x$ alloys.

Chapter. 2. Experimental Procedures

2.1. Introduction

In this chapter, the techniques for fabricating, processing, and characterising the samples are introduced. They include:

- Sputtering technique for depositing thin films.
- Dektak profilometer for thickness measurements.
- The vacuum furnace for annealing samples at high temperature.
- X-ray diffractometer for structure analysis.
- Energy Dispersive X-ray Analysis (EDX) for measuring the composition.
- Polar Kerr Microscope (PKM) for imaging the domains structure.
- Vibrating Sample Magnetometer (VSM) and Superconductor Quantum Interference Device Magnetometer (SQUID) for measuring magnetic moments.
- UV Lithography and Ion Beam Etching for patterning samples.
- Transport measuring system for investigating the transport properties of films and structures including magnetoresistance and extraordinary Hall effect.

In the case of $Gd_{1-x}Co_x$ ferrimagnetic alloys, the vanishing of magnetisation at T_{comp} usually causes a problem for magnetometry measurements. However, transport (the extraordinary Hall effect - EHE) measurements and magneto-optical (the polar Kerr effect - PKE) measurements are not sensitive to the total magnetic moment. Because EHE depends on the conduction band polarisation and PKE depends on the polarisation of sub-bands involved in the optical transitions, both effects (EHE and PKE) maintain large contrasts at T_{comp}. In this chapter, the PKE microscope and transport measuring system will be presented in greater details because they are the main techniques used in this thesis.

2.2. Sample fabrication: DC - magnetron sputtering

The samples in our studies have been fabricated using the facing-target magnetron sputtering technique at Institut Néel (all $Gd_{1-x}Co_x$ based samples) and the magnetron sputtering technique at Vietnam National University in Hanoi (Fe/Cr multilayers).

2.2.1. At Institut Néel (IN)

There are four DC sputtering sources in the facing target sputtering system at Institut Néel (IN). Each source uses two targets of the same size, 30 mm in diameter and around 4 mm in thickness. Substrates are mechanically held using kapton on the substrate holder during

deposition. There are four couples of $SmCo_5$ permanent magnets arranged on the substrate holder confronting the four sputtering sources to create an applied magnetic field parallel to the substrates during deposition. Before deposition the chamber is pumped down to 1×10^{-7} mbar as a base pressure, and then Ar gas is introduced into the chamber and pressure is kept at 3×10^{-3} mbar during deposition. The power supplies are then turned on to ignite the Ar plasma. The sputtering current was set at 35 mA for all samples and all the substrate holders are grounded. All substrates for the films based on $Gd_{1-x}Co_x$ layers are 300 µm-thick Si wafer. During deposition, the substrate temperature is room temperature.

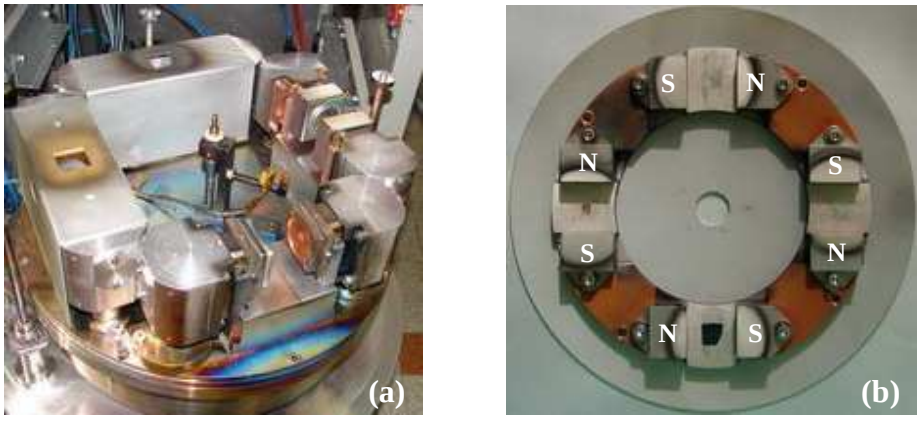

Fig. 2.1. The distribution of four sputtering sources (a) and four substrate positions (b) on the substrate holder in the facing target sputtering system at IN.

Actually the substrates are kept hidden from the sources during the first 5 - 10 minutes after the ignition of the plasma, so that the targets can be cleaned and get rid of any oxide layer that may form when the targets are exposed to air or not used for a few hours. The substrate holder is rotated automatically to expose the substrates to the sources and a shutter allows deposition for a chosen duration depending on the sputtering rate and the required thickness. From initial pumping and gas control to deposition the process is controlled by a computer program (shutter on/off). It allows automatic multilayer deposition.

2.2.2. At Vietnam National University in Hanoi (VNUH)

The sputtering system at Vietnam National University in Hanoi (VNUH) is magnetron type and has three sputtering sources, one DC source and two RF sources. Each source uses one target. The two RF plasmas are created using a frequency of 13.56 MHz. The targets are disks of 75 mm in diameter and around 1 mm thick. The Fe/Cr multilayers were deposited using two RF sources with two targets of Fe and Cr. During a typical sputtering process, substrates are mounted on the top plate by kapton. All targets and substrates are water-cooled at room temperature. The base pressure is 10^{-7} mbar. Ar gas pressure is 3×10^{-3} mbar during deposition.

The power supply is set at 200 W to ignite the argon plasma. The targets are always cleaned with 5 mn of presputtering to get rid of any oxide layer. The substrate holder is rotated manually to expose the substrates to the sources for a certain amount of time calculated depending on the required thickness of the film and the deposition rate.

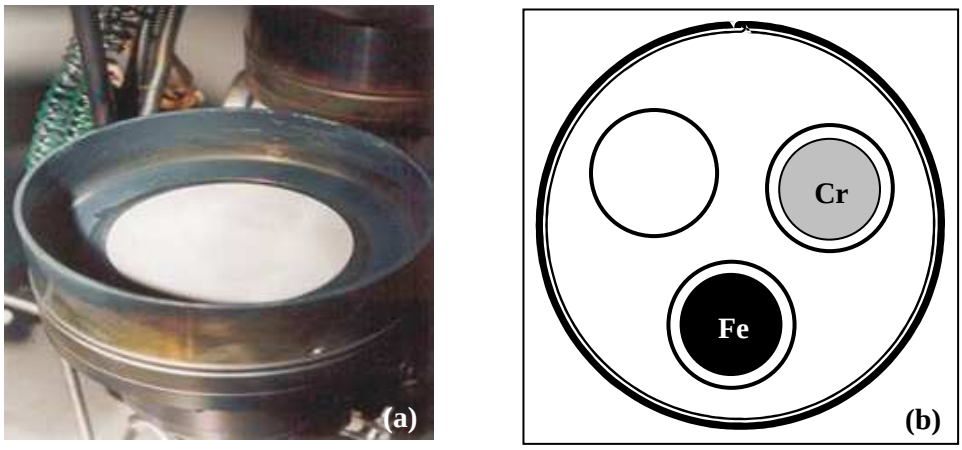

Fig. 2.2. One of three sputtering sources (a) and three targets distribution (b) in the magnetron sputtering system at VNUH.

2.3. Thickness measurement

2.3.1. At Institut Néel (IN)

Before depositing the $Gd_{1-x}Co_x$ based samples, several thickness calibrations have been carried out to get the deposition rates for all targets in the same sputtering conditions (3×10^{-3} mbar of Ar, 35 mA). Some standard samples were deposited with different sputtering times. Several narrow kapton bands were pasted on the surface of substrates before deposition to create steps between the film and the substrate during deposition. The kapton stripes are removed after deposition and the samples are cleaned with acetone before measuring the thickness.

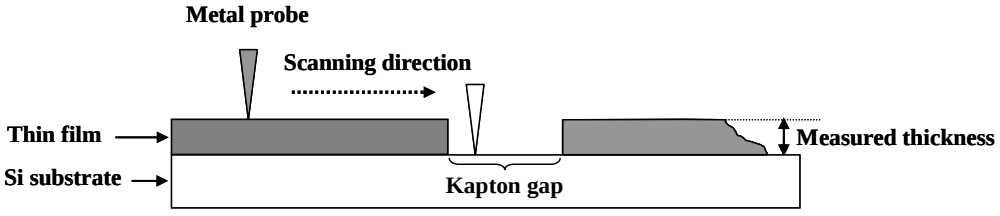

Fig. 2.3: The principle of thickness measurement.

The thickness of thin films were measured by using a Dektak profilometer at IN. The

principle of measurement is shown in Fig. 2.3. A metal tip (thickness detector) is scanned over the surface of the film in the direction across the kapton gap. At the edge of the gap, the probe will climb from the surface of film down to the surface of substrate. The movement of metal probe is turned into an electric signal and processed by computer. The real position of the probe on the sample is monitored by a video camera included in the machine. The vertical offset of the probe when it scans across the edge of kapton gap is the thickness of the thin film.

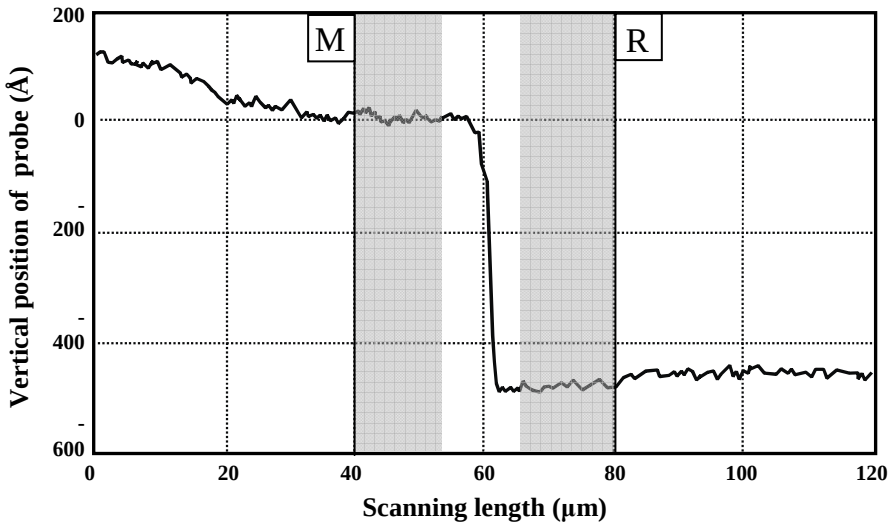

Fig. 2.4. Scanning results of a Si\Ta thin film measured by Dektak profilometer

An example of thickness measurement is presented in Fig. 2.4 for a Si\Ta thin film. The noise of measurement is about 40 Å. The measured thickness is about 480 Å. The relative accuracy is 40/480 = 8.3%. In order to get the mean thickness of the film, several measurements have to be carried out at different areas on the film. All the measured thicknesses are then averaged to get the mean thickness of thin film.

Table. 2-1: The deposition rates of different targets in the sputtering condition of 35 mA and 3×10^{-3} mbar Ar measured for facing targets sputtering system at IN.

Target	Deposition rate (Å/s)	Target	Deposition rate (Å/s)
Ta	0.92	$Gd_{14}Co_{86}$	1.20
$Fe_{19}Ni_{81}$ (Py)	1.23	$Gd_{10}Co_{90}$	0.95
Cu	2.29	$Gd_{10}Co_{90}$ + $Gd_{14}Co_{86}$	1.20

Because the error in measurement (40 Å) is the same for all measured samples, the relative accuracy of thickness measurement depends on the thickness of the film. The thicker the film is, the more accurate the measurement is. That is why all standard samples are quite

thick (above 200 nm) in comparison with the samples studied in this thesis (below 120 nm). The deposition rates of several materials for the sputtering system at IN are presented on Table. 2-1. All $Gd_{1-x}Co_x$ based layer samples in this thesis were fabricated in the same sputtering condition with a current of 35 mA and an Ar pressure of 3×10^{-3} mbar.

2.3.2. At Vietnam National University in Hanoi (VNUH)

The magnetron sputtering system in VNUH automatically performs the thickness of the film during deposition by using a quartz oscillator. The frequency of the oscillator changes depending on the thickness of the material layer deposited on it. The thickness of the film is automatically calculated from the change of frequency.

2.4. Heat treatment

After deposition, the Fe/Cr samples have been annealed for a duration of 1 hour at different temperatures ranging between T_A = 200 °C and 500 °C in a high vacuum chamber with a base pressure of 5×10^{-5} mbar. The samples have been inserted into the hot zone of the furnace equilibrated at the annealing temperature, held during the chosen time, and then cooled down to room temperature in the furnace for a few hours. These experiments were performed in VNUH.

2.5. Composition measurement: Energy Dispersive X-ray Analysis (EDX)

EDX Analysis is a technique used for identifying the elemental composition of a specimen. The EDX analysis system works as an integrated feature of a scanning electron microscope (SEM). During EDX Analysis, the sample is bombarded with an electron beam inside the scanning electron microscope. The bombarding electrons collide with the sample atoms' own electrons, ejecting some of them off in the process. A position vacated by an ejected inner shell electron is eventually occupied by a higher-energy electron from an outer shell. To be able to do so, however, the transferring outer electron must give up some of its energy by emitting an X-ray.

The amount of energy released by the transferring electron depends on which shell it is transferring from, as well as which shell it is transferring to (this is an intra atomic transition). Furthermore, the atom of every element releases X-rays with unique amounts of energy during the transferring process. Thus, by measuring the energy of the emitted X-rays, the identity of the emitting atom can be established.

The output of an EDX analysis is an EDX spectrum (see Fig. 2.5). The EDX spectrum is just a plot of count rates as a function of X-ray energy. An EDX spectrum normally displays peaks corresponding to the energy levels for which the most X-rays have been received. Each of these peaks is unique to an atom, and therefore corresponds to a single element. The higher a peak in a spectrum is, the more concentrated the element in the specimen is. An EDX spectrum plot not only identifies the element corresponding to each of its peaks, but the type of X-ray to

which it corresponds as well. For example, a peak corresponding to the amount of energy possessed by X-rays emitted by an electron in the L-shell going down to the K-shell is identified as a K-Alpha peak. The peak corresponding to X-rays emitted by M-shell electrons going to the K-shell is identified as a K-Beta peak (see inset of Fig. 2.5).

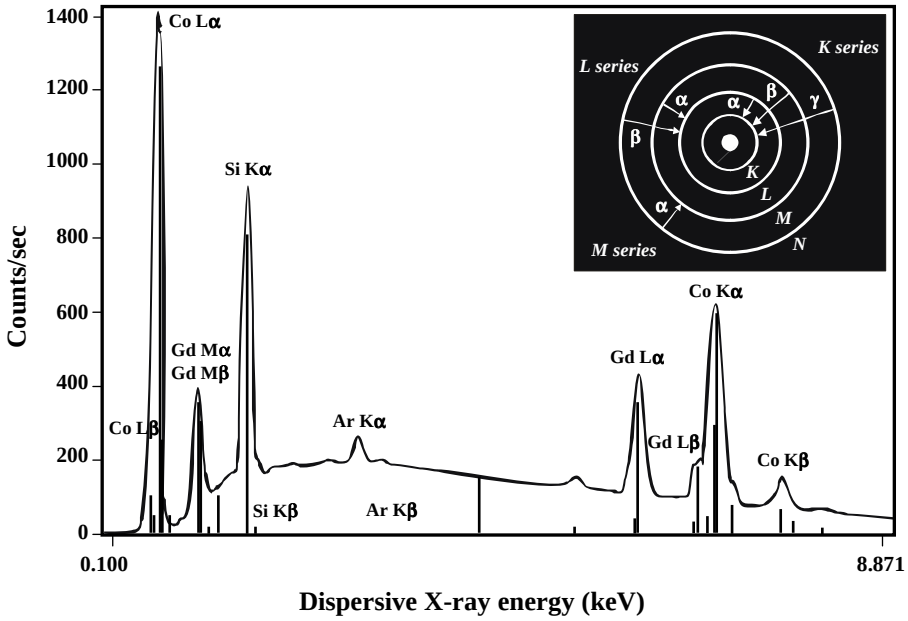

Fig. 2.5: An EDX spectrum of a Si\$Gd_{1-x}Co_x$ thin film sputtered in Ar^+ ion gas. The insert is the diagram of the intra atomic transition inside electron shell of an atom.

The quantitative element composition of $Gd_{1-x}Co_x$ alloys has been analysed by using EDX technique in IN with an accuracy of 1%.

2.6. Structure characterisation: X-ray Diffractometer

The phase composition and phase transformation of Fe/Cr multilayers were examined by means of X-ray diffraction (XRD). The X-ray diffraction patterns were taken using a Siemens D5000 with a Co K_α radiation (λ_{Co} = 1.78897 Å) at VNUH. This diffractometer is equipped with diffracted-beam Soller slits. A diffraction range 2θ between 20° and 110° was chosen using a 0.01°/3 s continuous scanning speed. The computer program was used to subtract the background and remove the data of Co $K_{\alpha 2}$ radiation. The reflections were indexed and the phases were determined by comparing the experimental positions and intensities of the reflections with the corresponding standard patterns. The average crystalline size <d> in the samples can be evaluated from the XRD line broadening by using the Scherrer's formula through the full width at half maximum of a diffraction peak :

$$< d > = \frac{k\lambda}{w \cos\theta} \qquad \textbf{(2.1)}$$

where λ is the X-ray wavelength, θ is the peak position, w is the peak width in units of radians and k is a geometry factor (k = 0.9).

The microstructure of the samples based on $Gd_{1-x}Co_x$ layer has been measured by X-ray diffractometer at Institute Néel. The measurement parameters are the same as the ones used at VNUH.

2.7. Magnetometry

The macroscopic magnetic properties of samples have been investigated by using the Vibrating Sample Magnetometer technique (at VNUH and IN) and a Superconductor Quantum Interference Device Magnetometer (at IN).

2.7.1. Vibrating sample magnetometer (VSM)

The magnetometry data of Fe/Cr multilayers were recorded at room temperature by a DSM Model 880 VSM with resolution of 10^{-5}-10^{-7} emu and a magnetic field range between –1.4 T and 1.4 T at VNUH.

The magnetic properties of GMR samples using $Gd_{1-x}Co_x$ layers were measured by a VSM Oxford instrument at IN. The measurements were carried out with resolution of 10^{-5} emu in the range of temperature from 10 K to room temperature. An external magnetic field between -8 T and 8 T is created with a superconducting coil inside a cryostat of liquid helium.

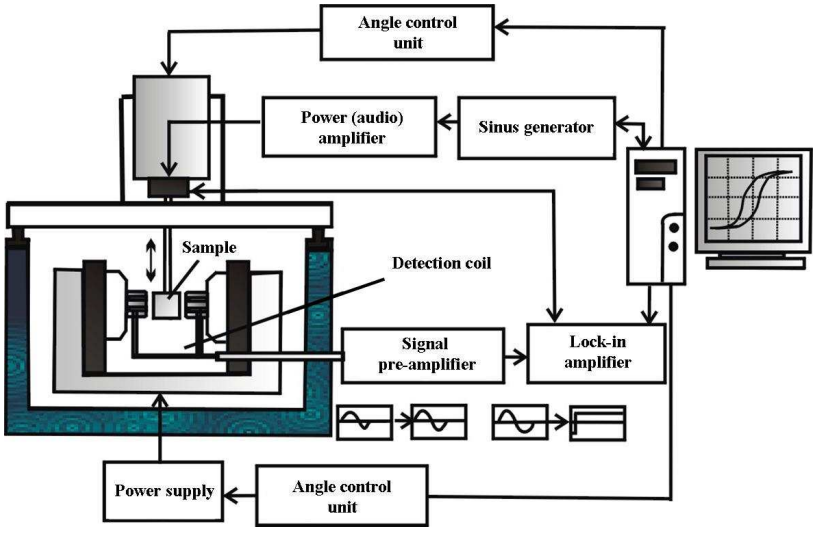

Fig. 2.6: Schematic of vibrating sample magnetometer (VSM) with electromagnet.

The schematic presentation of a vibrating sample magnetometer (VSM) using an electromagnet is shown in Fig. 2.6. In the VSM system at IN, the applied field is parallel to the vibration axis.

2.7.2. Superconducting quantum interference device magnetometer (SQUID)

The magnetisation of the $Gd_{1-x}Co_x$ films (in case of small samples or/and near compensation temperature) have been measured on a Quantum Design Properties Measurement Systems (MPMS) XL SQUID magnetometer at IN. The d.c. magnetic field is as high as 6 T with an accuracy of 10^{-5} T thanks to the use of superconducting coils. The temperature of sample can be varied from 1.9 K to 400 K with a resolution of 0.01 K. The SQUID uses an extremely sensitive detection method that is able to measure the magnetisation values in the range of 10^{-8} emu to 10^{-6} emu.

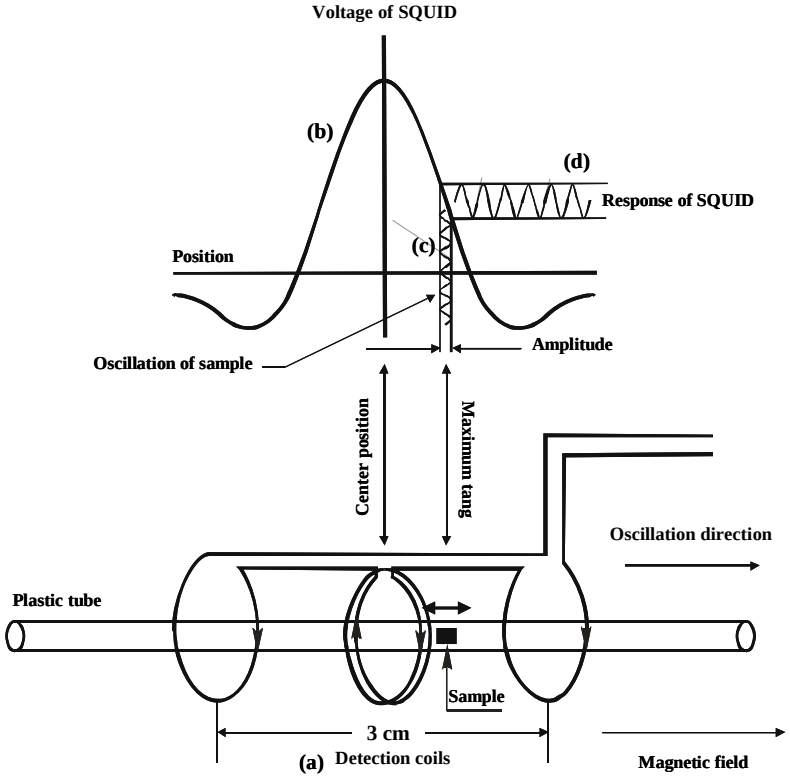

Fig. 2.7: Schematic of a SQUID magnetometer.

2.7.3. The problem of substrates and sample holder

The total magnetic moment (m_{total}) measured on magnetometers (VSM and SQUID) can be written as $m_{total} = m + m_{sub} + m_{hold}$ where m is the magnetic moment of the thin film, m_{sub} is the magnetic moment of the Si substrate, and m_{hold} is the magnetic moment of the sample holder. In order to get the magnetic moment of thin film, the contributions from sample holder and Si substrate must be subtracted.

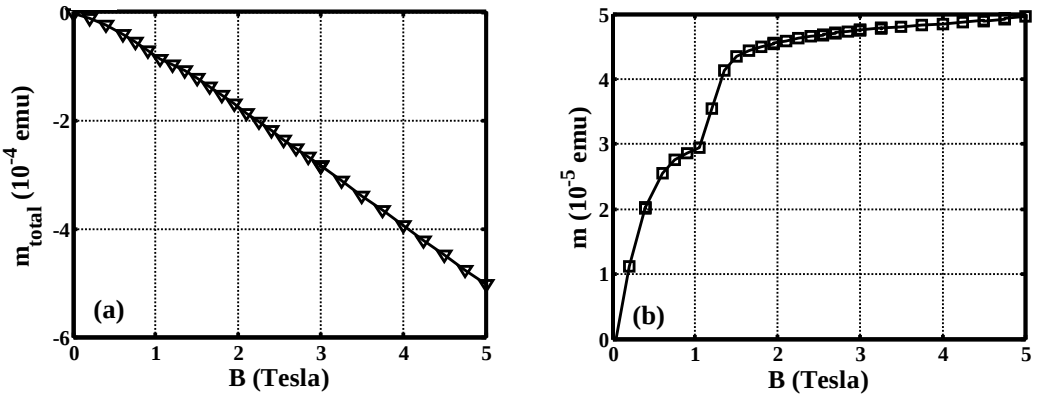

Fig. 2.8. The applied field dependence of the magnetic moment of a Si\ $Gd_{1-x}Co_x$ sample measured at 250 K by the SQUID magnetometer: (a) the total magnetic moment and (b) the magnetic moment of thin film after correction.

Firstly, the total magnetic moment m_{total} is measured by VSM or SQUID. Then the sample is taken off and the sample holder is installed again into the magnetometer to measure its magnetic moment m_{hold} in the same condition. Secondly, the sample is weighed to find the mass D of substrate (the mass of film is very small in comparison with the mass of substrate and can be neglected, so the mass of sample can be considered as the mass of substrate). In case of Si substrate, the density at room temperature is D_o = 2.336 g/cm^3. The induced magnetic moment of Si substrate m_{sub} can be calculated by using formula $m_{sub} = \chi_{Si}\mu_o H.D/D_o$ where H is the applied field, μ_o is the permeability of vacuum, and $\chi_{Si} = -1.4\times10^{-7}$ is the diamagnetic susceptibility of Si [41]. Finally, the magnetic moment of the thin film is calculated using the formula $m = m_{total} - m_{sub} - m_{hold}$. An example for a Si\$Gd_{1-x}Co_x$ thin film is displayed in Fig. 2.8 showing the total magnetic moment as measured and the magnetic moment of thin film obtained after correction.

2.8. Polar Kerr Microscope

2.8.1. The magneto-optical Kerr effect

The magneto-optical effect in reflection geometry is called the magneto-optical Kerr effect. Its description involves three basic geometries: polar Kerr effect, longitudinal Kerr effect, and transverse Kerr effect [44].

Polar Kerr effect: A beam of light with rectilinear polarisation falls under normal incidence on a surface which is magnetised in a direction perpendicular to the surface (Fig. 2.9-a). After reflection, the polarisation has turned by an angle typically less than a degree, and some ellipticity has appeared. Reversing the magnetisation leads to the opposite rotation. This case corresponds, in magnetostatic terms, to an unfavored situation. It occurs only if the magnetisation is forced to be perpendicular to the surface, under the effect either of a sufficient

strong field, or of a perpendicular anisotropy. For symmetry reason, the rotation does not depend on the in-plane component of magnetisation. Thus polar Kerr effect is suitable for the present $Gd_{1-x}Co_x$ samples with perpendicular anisotropy.

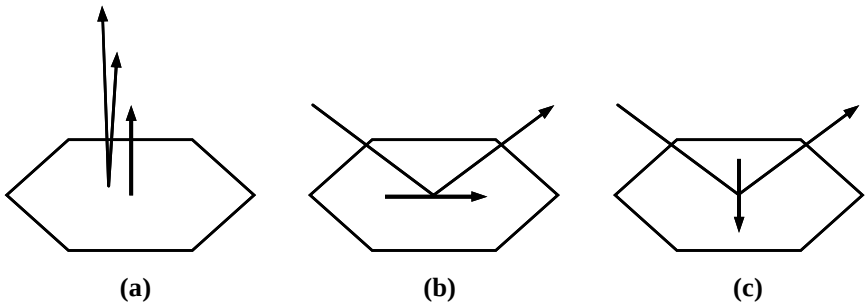

Fig. 2.9: The three basic configurations for the magneto-optical Kerr effect (a) polar - (b) longitudinal - (c) transverse [44].

The longitudinal Kerr effect: A beam strikes a surface which is magnetised in its plane under oblique incidence (Fig. 2.9-b), the magnetisation being in the plane of incidence. If the polarisation (the electric field vector $\vec{E}$) of the incident beam is perpendicular or parallel to the plane of incidence of the light, then the polarisation of the reflected beam is slightly elliptical, with a major axis rotated with respect to the incident polarisation by an angle of generally less than a degree. If the incident polarisation is neither parallel nor perpendicular to the plane of incident, then the phase shift due to ordinary reflection will make the magneto-optical effect much less noticeable. Here again, the rotation reverses when the magnetisation is reversed.

The transverse Kerr effect: The geometry is the same as in the longitudinal case, except that the magnetisation, although it is still in the plane of the specimen surface, is perpendicular to the plane of incidence (Fig. 2.9-c). Now there is no rotation for perpendicular or parallel incident polarisation, and in fact there is no effect at all for perpendicular polarisation. However, reversing the magnetisation leads, if the incident polarisation is perpendicular, to a change in the intensity of reflected light. So the measurement is a change of reflectivity and not the appearance of a rotated polarisation.

2.8.2. Polar Kerr microscope (PKM)

Since the polar Kerr effect reveals the magnetic domains when the magnetisation has an appreciable component in the direction normal to the illuminated surface of the sample, it is very suitable for imaging domain structure of magnetic thin films with perpendicular anisotropy. Polar Kerr effect has been applied for making polar Kerr microscope (PKM). The most common PKM is sketched in Fig. 2.10.

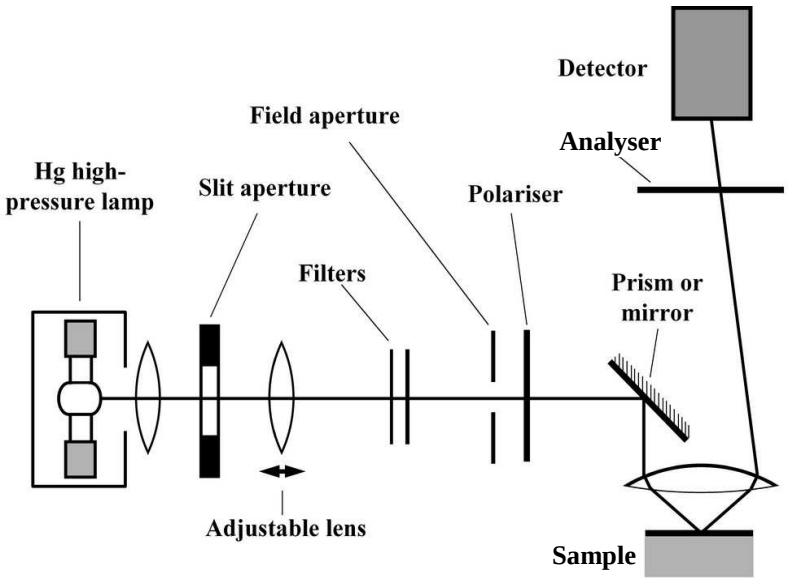

Fig. 2.10: Scheme for a common Kerr effect microscope (see ref. [80] p. 35)

The magnetic domain structure of the samples with $Gd_{1-x}Co_x$ layers in this thesis has been observed by using PKM (Hg lamp) at IN with a resolution of 2 μm. The sample holder can be heated from room temperature to 200 ^oC and a magnetic field can be applied by using a Cu coil for ac field or a $SmCo_5$ permanent magnets for dc field (see Fig. 2.11). Images recorded with opposite contrasts by tilting the analyser are subtracted to reduce the non-magnetic contrast in the images.

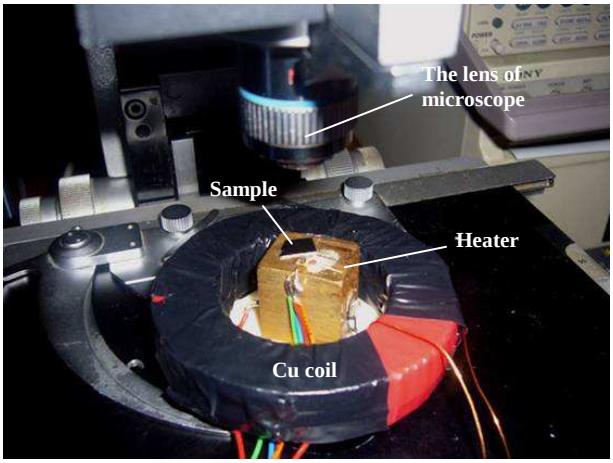

Fig. 2.11. The setup for measuring the perpendicular domain structure by the polar Kerr microscope at IN with the variation of temperature and applied field.

In the case of thin films with Ta capping layer, the $Gd_{1-x}Co_x$ layer is always deposited on the top, right under the Ta capping layer. The perpendicular domain structure can be observed through Ta capping layers thinner than 15 nm. The thinner the Ta capping layer is, the

easier the observation of the domain structure of $Gd_{1-x}Co_x$ thin film is. The Ta capping layers in this thesis are 8 nm thick.

2.9. Patterning the sample

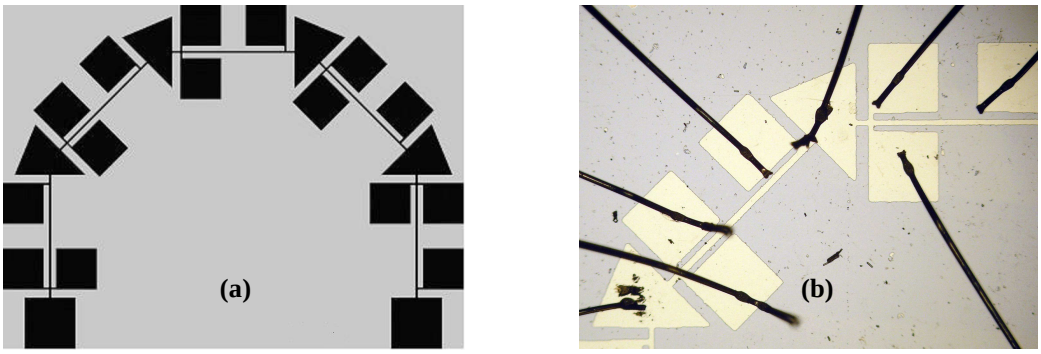

Fig. 2.12. (a) A lithography mask and (b) a picture of a patterned area on a sample.

In order to pattern the sample at the micron scale for this thesis, UV optical lithography and Ar ion beam etching have been used.

2.9.1. UV Lithography

Firstly, the sample is spin-coated by a photoresist layer namely S1818 (it is a positive resist) 2 µm thick. Then a corresponding mask is placed in close contact (Fig. 2.12.a). The shape of protected area on the sample is defined by the shape of the lithography mask. Continuously, a UV beam illuminates the sample for an appropriate duration (45 seconds). The area of photoresist obstructed by the mask is not modified by the UV beam. Finally the sample is immersed into a specific solution (this is a specific solution for the positive resist of S1818 including 50% volume of Microposit Developper Concentrate) for a specific duration (50 seconds). Because the exposed area of S1818 photoresist (which was not protected by the mask) on the sample, under the effect of the UV beam, is chemically changed, it is easily cleared off in the solution after a specific duration (50 seconds) while the protected area of photoresist is still stable. After lithography, the sample with a photoresist area reproducing the shape of the mask is obtained (positive photoresist).

2.9.2. Ion beam etching (Ar)

In this stage of etching, the sample with patterned photoresist area on top will be bombarded by a high energy Ar^+ ion beam. The material in the exposed area on the sample which is not protected by photoresist will be removed from the sample after a specific time of exposure to the Ar beam. After this etching stage, a thin film of the same shape as the mask is

created. The final step is to remove the patterned photoresist area from the sample by using acetone, i.e. lift-off step, so the patterned area of thin film is revealed (see Fig. 2.12.b).

2.10. Magnetoresistance and Hall effect measurements

Transport properties of samples have been investigated by means of magnetoresistance and Hall effect. The magnetoresistance measurements for Fe/Cr multilayers were all carried out at VNUH. The Hall effect and magnetoresistance measurements for the $Gd_{1-x}Co_x$ based layer samples were all made at IN. The overview of measurement techniques will be described hereafter.

2.10.1. Temperature control and the external magnetic field regulation

The sketch of giant magnetoresistance measurement system at VNUH is presented in Fig. 2.13. The lowest temperature, 77 K, can be reached by using liquid nitrogen. He gas is used to allow a good thermal conduction between liquid nitrogen and sample holder. The temperature is controlled from 77 K to 300 K with a heating coil. The external magnetic field can be varied from -0.8 T to +0.8 T with a resolution of 0.2 mT by using an electromagnet with a Cu coil at room temperature.

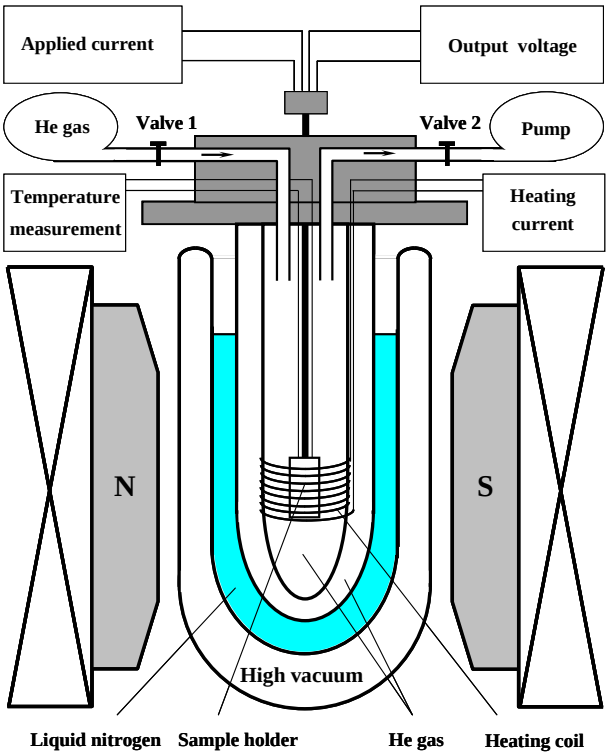

Fig. 2.13: Measurement configuration of magnetoresistance in the range 77-300 K at VNUH.

All the magnetoresistance and Hall effect measurements of the samples based on $Gd_{1-x}Co_x$ layer have been carried out in a transport measuring system at Institut Néel. The system

consists of a pumped helium cooled cryostat in which the sample can be placed and the temperature can be varied between 1.5 K and 300 K. The cryostat is equipped with a superconducting magnet which can reach a maximum magnetic field of 6 Tesla. The orientation of the sample with respect to the magnetic field can be varied manually before the measurement, such that the applied field can have an orientation parallel or perpendicular to the sample surface.

2.10.2. Contact distribution on the sample for measuring magnetoresistance (MR) and Hall effect (HE)

The contact distribution for measuring magnetoresistance and Hall effect of thin film is sketched in Fig. 2.14. The external magnetic field can be applied in the directions of Ox, Oy, or Oz depending on measurement. A dc voltage is applied to A and B to make a dc current I in Ox direction.

Magnetoresistance must be measured in the direction parallel to the current, so the MR output voltage V_{mr} is measured between C and D ($R_{mr} = R_{CD}$, $V_{mr} = V_{CD}$). The resistance between C and D can be derived from: $R_{CD} = V_{CD}/I_{AB} \Leftrightarrow R_{mr} = V_{mr}/I$.

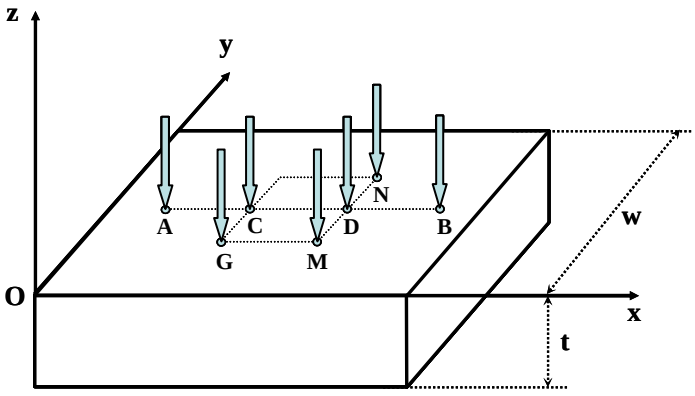

Fig. 2.14: The contact distribution for measuring magnetoresistance and Hall effect of thin film.

The Hall effect is measured in the direction perpendicular to the current, so the output Hall voltage will be taken from M and N (MN // Oy). The Hall resistance can be derived from: $R_{Hall} = R_{MN} = V_{MN}/I_{AB} \Leftrightarrow R_{Hall} = V_{Hall}/I$.

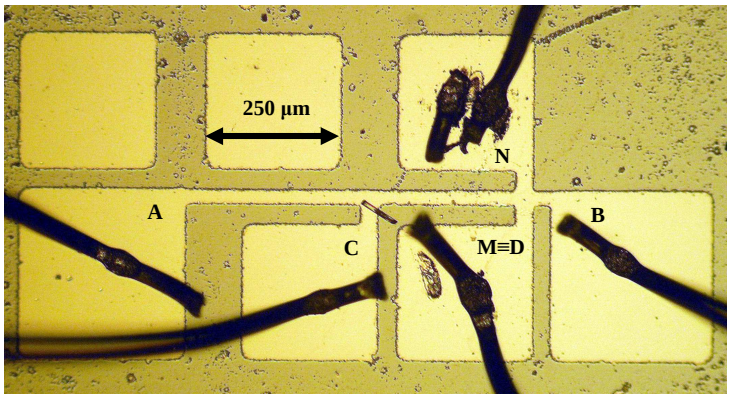

Fig. 2.15: Aluminium wire contacts on a patterned thin film of $Gd_{1-x}Co_x$.

In the case of large-enough samples, the contacts can be made by spring-loaded metallic probes contacting directly the surface of thin film. When samples are small or patterned, the metal probes are substituted by aluminium wires with diameter of 50 µm (Fig. 2.15). The contacts between aluminium wires and films are made by using a microbonding machine at IN.

2.10.3. Data processing

a. Zero field offset in the transport measurement system at IN

In the transport measurement system using a superconducting coil at IN, the computer regulates the applied field by setting a corresponding voltage on the input of superconducting coil. In order to make a zero applied field, the input voltage is set to zero. However, there is an offset during the variation of the field. The causes may be the remanence of the superconducting coil (vortices in the coil) and/or the offset in the electronic system. This offset makes shift of the applied field in the output data (saved data) in comparison with the real applied field in the cryostat. Experiments show that the magnitude of the shift (ΔB) depends on the earlier maximum applied field (B_{max}). The larger the B_{max} is, the larger the amplitude of ΔB is.

In our measurements using cryostat with the superconducting coil, only two measuring regimes (low-field and high-field regimes) of the cryostat have been used. The low-field regime has a maximum applied field of 0.6 T with a finest step of 1 mT, and the high-field regime has a maximum applied field of 6 T with a finest step of 10 mT. In order to correct the zero field problem of cryostat, a GMR sample based on $Gd_{1-x}Co_x$ layer has been chosen as a standard sample to measure the magnetoresistance at room temperature using the cryostat first. Then the standard sample is measured again (with the same electric contacts) by using a Cu solenoid coil at room temperature. There is no offset of applied field (other than the Earth field) in the measurement using the Cu solenoid coil because it is not superconductor and the current is

measured directly. By comparing the two magnetoresistance curves, the shift of applied field ΔB can be found.

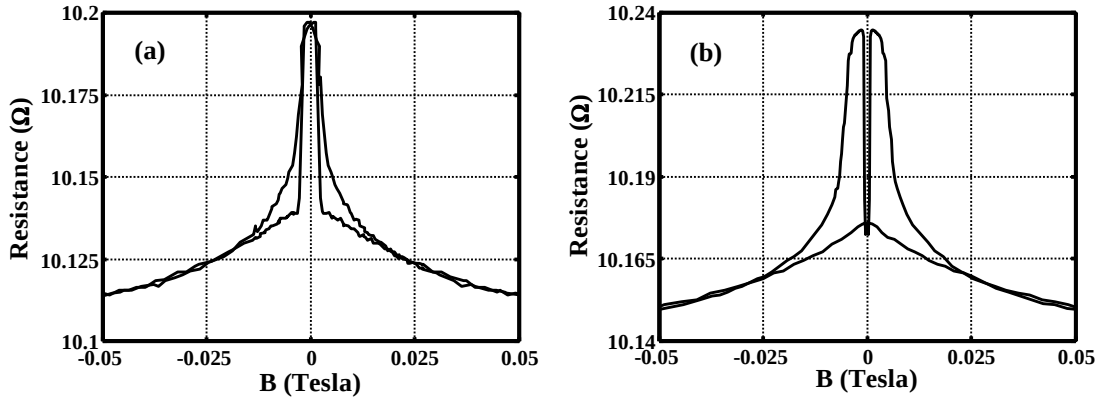

Fig. 2.16. The GMR curves at 300 K of the standard sample measured using cryostat in the low-field regime (B_{max} = 0.6 T) (a) and using the Cu solenoid coil (b). The shift of applied field is ±3 mT.

The magnetoresistance curve of the standard sample measured using the cryostat in low-field regime (B_{max} = 0.6 T) is presented in Fig. 2.16.a. Comparing to the curve measured with Cu solenoid coils at room temperature (Fig. 2.16.a), we found the shift of applied field ΔB for the low-field regime of cryostat as presented in Table. 3-1. In order to get the real applied field B in the cryostat, the field in the output data files B_{data} must be corrected using formula $B = B_{data} + \Delta B$.

Table. 2-2: The shift of the applied field in the low-field regime (B_{max} = 0.6 T) of the transport measurement system using superconducting coil at IN.

The applied field range	The shift of applied field ΔB (Tesla)
from +0.6 to -0.6	-0.003
from -0.6 to +0.6	0.003

In the high-field regime of cryostat, because the shift is smaller than the finest step (10 mT) of the regime, it is impossible to find the real ΔB in this case. However, since the aim of the high-field measurement is to investigate the high field behaviours of sample, the small shift of the field is not important and can be neglected.

b. Separating the magnetoresistance signal and the Hall signal from each other

In transport measurements, it is impossible to install the two contacts for measuring magnetoresistance in the direction exactly parallel to the current. Similarly, we are not able to lay the two contacts for measuring Hall effect in the direction exactly perpendicular to the

current. So the MR signal and HE signal are always mixed in experiment, even with patterned samples, therefore, they always need to be separated from each other. Taking advantage of the fact that MR effects (OMR, AMR, GMR, and PHE) are even functions of the applied field while the Hall effects (OHE and EHE) are odd functions, we can separate MR signal and HE signal from each other by using the following technique.

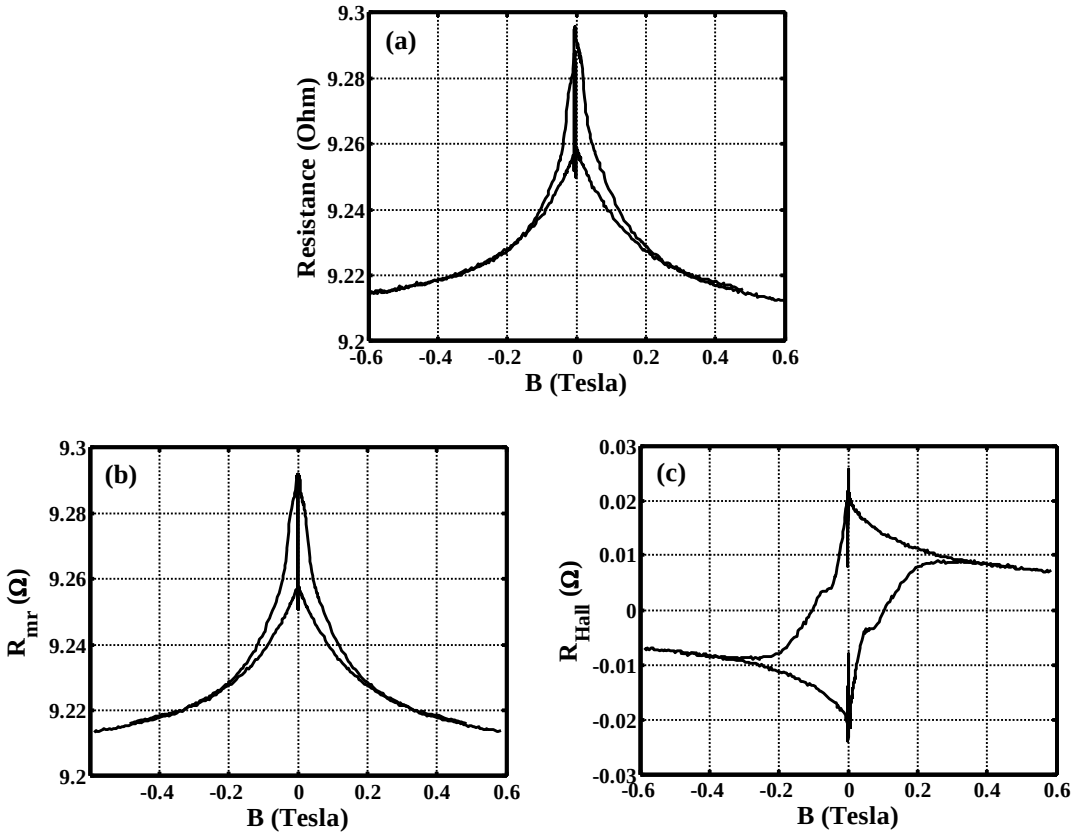

Fig. 2.17: The MR and HE superposed data (a) before processing. The MR data (b) and HE data (c) become obvious after being separated by using formula (2.2).

During measurement, the applied current is kept constant and the voltage between G and N (Fig. 2.14) is measured as a function of applied field. Because GN is neither parallel nor perpendicular to the applied current (in AB direction), the measured signal (V_{GN}) is a superposition of MR signal (V_{mr}) and HE signal (V_{Hall}): $V_{GN} = V_{GM} + V_{MN} = V_{mr} + V_{Hall}$. For separating MR signal and HE signal from each other, the measurement must be carried out twice in two opposite applied fields ($+\vec{H}$ and $-\vec{H}$), we find:

$$V_{GN}(+\vec{H}) = V_{GM}(+\vec{H}) + V_{MN}(+\vec{H}) = V_{mr}(+\vec{H}) + V_{Hall}(+\vec{H}).$$

$$V_{GN}(-\vec{H}) = V_{GM}(-\vec{H}) + V_{MN}(-\vec{H}) = V_{mr}(-\vec{H}) + V_{Hall}(-\vec{H}).$$

where $V_{mr}(+\vec{H}) = V_{mr}(-\vec{H}) = V_{mr}$, and $V_{Hall}(+\vec{H}) = -V_{Hall}(-\vec{H}) = -V_{Hall}$. Eventually the calculation formulas for MR and HE signal are found as:

$$V_{mr} = \frac{V_{GN}(+\vec{H}) + V_{GN}(-\vec{H})}{2} \quad \text{and} \quad V_{Hall} = \frac{V_{GN}(+\vec{H}) - V_{GN}(-\vec{H})}{2} \qquad \textbf{(2.2)}$$

An example of MR and HE superposition is shown on Fig. 2.17. The data processing above is used to separate the MR and HE signal from each other. The MR data (Fig. 2.17.b) and HE data (Fig. 2.17.c) become obvious after being separated by using formula (2.2).

This data processing is used for all magnetoresistance and Hall effect measurements of all samples studied in this thesis. Such a processing cannot be applied to minor loops, where the symmetry hypothesis is not valid.

Chapter. 3. Composition-controlled compensation domain wall in $Gd_{1-x}Co_x$ thin films

3.1. Introduction

In micromagnetism, magnetisation is usually considered to have a constant amplitude, which is a correct assumption since the temperature of materials studied or used is usually much lower than their Curie temperature. In order to reduce the demagnetising energy, a multidomain structure can exist, and domain walls are created between neighbouring magnetic domains. So the creations of domain walls relate to and always come with the demagnetising energy, i.e. the magnetisation of the samples.

Domain nucleation, domain wall, and magnetisation reversal by domain wall propagation have recently become the focus of interest because the detailed access to a single wall has become experimentally feasible. This allows us to address fundamental physical questions, such as the geometry-dependent spin structure ([59]-[60]), pinning of domain walls at constrictions ([61]-[64]) and the details of the domain wall propagation processes ([65]-[66]). These fundamental questions have become relevant to present recording industry because the individual magnetic bit has shrunk to such a scale. Additionally, devices based on manipulating a single domain wall have been suggested for storage and logic [67].

In this chapter, special 180° domain walls will be created without the existence of demagnetising field by using $Gd_{1-x}Co_x$ ferrimagnetic alloys in vicinity of their compensation temperatures (T_{comp}). The domain walls with no magnetisation, i.e. no demagnetising energy, could be very useful for studying the role of magnetisation in magnetic effects including the spin torque, which goes beyond the aim of this thesis. Moreover, rather than using conventional magnetic fields (to reverse magnetisation) or spin polarised currents (in the current-induced domain wall motion ([68]-[69]) to move domain walls, in this chapter, compensation domain wall will be moved by changing the temperature under a fixed applied field.

3.2. Experimental details for making and characterising $Gd_{1-x}Co_x$ thin films

There are four $Gd_{1-x}Co_x$ targets in the same size (30 mm in diameter and around 4 mm in thickness), two of them are $Gd_{0.10}Co_{0.90}$, and the other two are $Gd_{0.14}Co_{0.86}$. Since each facing-target sputtering source requires two targets (see Fig. 3.1.a), we can organise three different sources from the four targets: $Gd_{0.10}Co_{0.90}$+$Gd_{0.10}Co_{0.90}$, $Gd_{0.10}Co_{0.90}$+$Gd_{0.14}Co_{0.86}$, and $Gd_{0.14}Co_{0.86}$+$Gd_{0.14}Co_{0.86}$. The film compositions are measured using the EDX microanalysis.

Actually, the composition of films is always different from the composition of targets. The films are always Gd-rich compared to the targets as presented in Table. 3-1. It proves that there is a difference between the ratio of Gd and Co deposition rates and the ratio of Gd and Co percentages in the targets. The origin may be the differences in the atom masses, different sputtering solid angles, resputtering yields or, less likely, in the magnetic moments of Gd and Co elements.

Table. 3-1. The composition of $Gd_{1-x}Co_x$ thin films sputtered at 3×10^{-3} mbar of Ar gas and 35 mA of current depends on the composition of targets. The composition of thin film is measured by EDX technique with an accuracy of $\Delta x = 1\%$.

Target couple	Co fraction (x)
$Gd_{0.10}Co_{0.90}$+$Gd_{0.10}Co_{0.90}$	0.78 ÷ 0.81
$Gd_{0.14}Co_{0.86}$+$Gd_{0.14}Co_{0.86}$	0.72 ÷ 0.75
$Gd_{0.10}Co_{0.90}$+$Gd_{0.14}Co_{0.86}$	0.76 ÷ 0.79

Moreover, the in-plane compositional homogeneity of GdCo thin film strongly depends on the position of substrates on the substrate holder. The most homogeneous samples are obtained when the substrates are installed at the center of substrate holder (position I in Fig. 3.1.b). When the substrates are installed away from the center of substrate holder (position II in Fig. 3.1.b), an in-plane composition gradient is induced. The composition measurement shows that the further from the center the substrate is, the higher the Co fraction is.

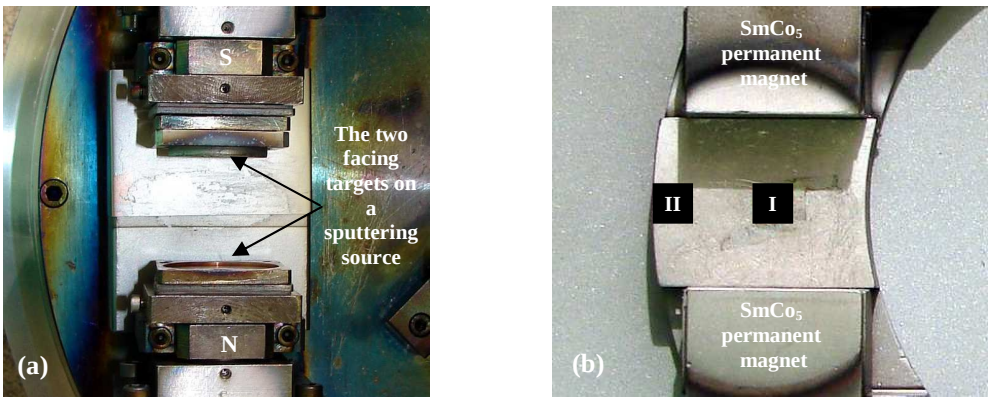

Fig. 3.1. Pictures of a sputtering source with two facing targets (a) and a substrate holder (b). Positions I (center) and II (left) on the substrate holder correspond to the most homogeneous and inhomogeneous thin films, respectively.

$Gd_{1-x}Co_x$ films (5 to 200 nm thick) were deposited onto Si(001) substrates using the

facing-target sputtering technique at Institute Néel in the same deposition conditions: Base pressure 1-2×10^{-8} mbar; Ar pressure P_{Ar} = 3×10^{-3} mbar; Sputtering current I = 35 mA. From 8 to 14 nm thick tantalum layers were deposited as buffer layer and capping layer to protect the films. In order to make $Gd_{1-x}Co_x$ thin films with a large in-plane gradient of composition, the substrates are installed about 1 cm away from the center of the substrate holder. The target couple $Gd_{0.14}Co_{0.86}$+$Gd_{0.14}Co_{0.86}$ was used to get an average compensation temperature close to room temperature. The experimental results for a Si\Ta (14 nm)\GdCo (100 nm)\Ta (8 nm) thin film with a gradient of composition will be reported in this chapter.

The perpendicular domain structure and the domain wall movement under the variations of temperature and applied field have been investigated by the polar Kerr microscope at IN (see section 2.8.2). Transport measurements of the samples with an in-plane gradient of composition have been carried out at room temperature in applied fields up to 0.1 Tesla.

3.3. The composition dependence of domain size

The deposition at room temperature of $Gd_{1-x}Co_x$ films induces a uniaxial perpendicular anisotropy K. The origin of this anisotropy is still unclear, anisotropic microstructure [70], dipolar interaction [71], stress-induced anisotropies ([72]-[73]), pair ordering ([5], [74]), anisotropic exchange [75], bond-orientational anisotropies [76], or local inelastic deformation [77] being some possible origins.

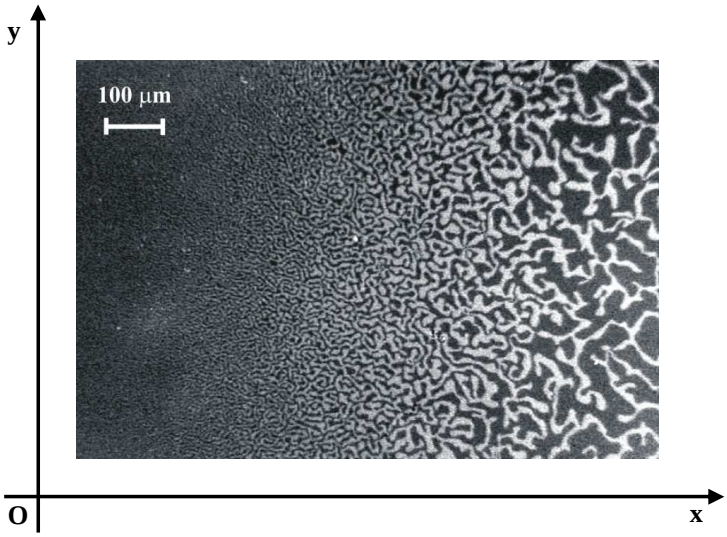

Fig. 3.2. Polar Kerr image at 300 K of a multidomain structure shows the perpendicular anisotropy and the existence of an in-plane gradient of domain size.

The polar Kerr image at room temperature of an as-deposited sample with an in-plane composition gradient in zero applied field shown in Fig. 3.2 proves the perpendicular anisotropy of $Gd_{1-x}Co_x$ layer. Because PKE with visible light is sensitive to the Co moments, black and white zones in the image display the two opposite directions of Co moments. The contrast here

is good enough to see clearly the perpendicular multidomain structure of the film.

For a thin film, magnetised out of plane, the domain size is determined by the demagnetising energy, the domain wall energy, and the film thickness. It was confirmed that, in 1 cm^2 area of sample, the thickness homogeneity is better than 5%. It means that in the area of this picture (about 1 mm^2), the impact of thickness variation on the domain size is negligible. So the in-plane variation of domain size showing in Fig. 3.2 confirms the existence of an in-plane composition gradient. The in-plane composition gradient makes an in-plane gradient of magnetisation. This magnetisation gradient makes a variation of demagnetising energy, and thereby, makes the gradient of domain size. In addition, in Fig. 3.2 the domain size does not change in the Oy direction, this suggests a uniaxial in-plane gradient of composition in Ox direction.

3.4. The compensation surface, compensation domain wall, and compensation zone in the $Gd_{1-x}Co_x$ thin film with an in-plane gradient of composition

In order to interpret experimental results, a mean-field model has been used to calculate the temperature dependence and the composition dependence of $Gd_{1-x}Co_x$ magnetisation. The Co-Co intrasublattice and the Gd-Co intersublattice molecular field coefficients were chosen as those used in the calculation for $Gd_{0.22}Co_{0.78}$ thin film in section 4.5.1, i.e. $\lambda_{CoCo} = 850$ and $\lambda_{GdCo} = 118$. All other required parameters are the same as already presented in the calculation for $Gd_{0.20}Co_{0.80}$ in section 1.3.3.

3.4.1. Compensation surface

Let us consider the composition dependence of the spontaneous magnetisation of $Gd_{1-x}Co_x$ alloys at a fixed temperature T. There is a Co fraction x_{comp} which corresponds to the alloy with zero spontaneous magnetisation, i.e. the Gd and Co sublattice magnetisations are compensated, therefore x_{comp} is called the Co compensation fraction at temperature T. Near x_{comp}, the spontaneous magnetisation of $Gd_{1-x}Co_x$ is small and varies linearly with x. When $x < x_{comp}$ the spontaneous magnetisation of alloy is Gd-dominant and it turns into Co-dominant when $x > x_{comp}$. This is due to the larger temperature dependence of Gd magnetisation compared to the Co one. For illustration, the composition dependences of the Gd and Co sublattice magnetisations calculated at 300 K are presented in Fig. 3.3. It turns out from this figure that the compensation fraction at 300 K is $x_{comp} = 0.765$.

When an in-plane composition gradient exists, at temperature T, a compensation surface can exist on the film. It is the 2D surface perpendicular to the film where the net magnetisation of alloy is zero, i.e. the Co fraction on the surface is the compensation fraction ($x = x_{comp}$). For example, on the compensation surface of a $Gd_{1-x}Co_x$ thin film at 300 K, the composition of alloy is $Gd_{0.235}Co_{0.765}$.

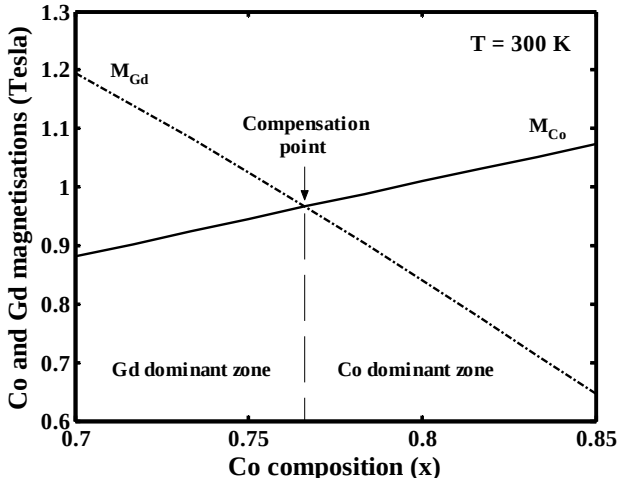

Fig. 3.3. Composition dependence of the Gd and Co sublattice magnetisations of $Gd_{1-x}Co_x$ alloys at 300 K calculated by the mean-field model. The compensation fraction is $x_{comp} = 0.765$.

Because x_{comp} is a function of temperature, one can expect that, in a $Gd_{1-x}Co_x$ thin film with in-plane gradient of composition, the compensation surface will move when the temperature changes. When x_{comp} is out of the composition range of the sample, there is no compensation surface on the sample.

3.4.2. Compensation domain wall and compensation zone

We now consider a $Gd_{1-x}Co_x$ thin film having an in-plane gradient of composition and a compensation surface at a specific temperature T. Under an applied field perpendicular to the film (H_{max}), the Gd-rich part will align Gd moments with the field, and Co-rich part will align Gd moments antiparallel to the field, so a 180^o domain wall is created parallel to the compensation surface. It is called a compensation domain wall (see Fig. 3.4).

As will be shown in section 4.7.4 for $Gd_{1-x}Co_x$ thin films, the coercive field is a function of magnetisation, the smaller the magnetisation is, the larger the coercive field is. It is also well known for ferrimagnetic compounds that there is a maximum of the coercivity in the neighbourhood of compensation points. Because the compensation domain walls are taking place where the coercive field is equal to the applied field, the position of compensation domain wall depends on the applied field. Close to the compensation surface, the coercive field may be large enough that the magnetic configuration does not change with field but depends on the film history. Due to the fact of no (net) magnetisation, the coercive field of the compensation surface is very large as long as the spin-flop does not happen, so that the compensation domain wall usually does not coincide with the compensation surface. The larger the applied field is, the closer to the compensation surface the compensation domain wall is. When the applied field is reversed into the opposite direction ($-H_{max}$), another compensation domain wall is created but on the other side with respect to the compensation surface. Thank to the perpendicular anisotropy

of $Gd_{1-x}Co_x$ thin film, the compensation domain wall can be observed by using polar Kerr imaging as it is sensitive to Co.

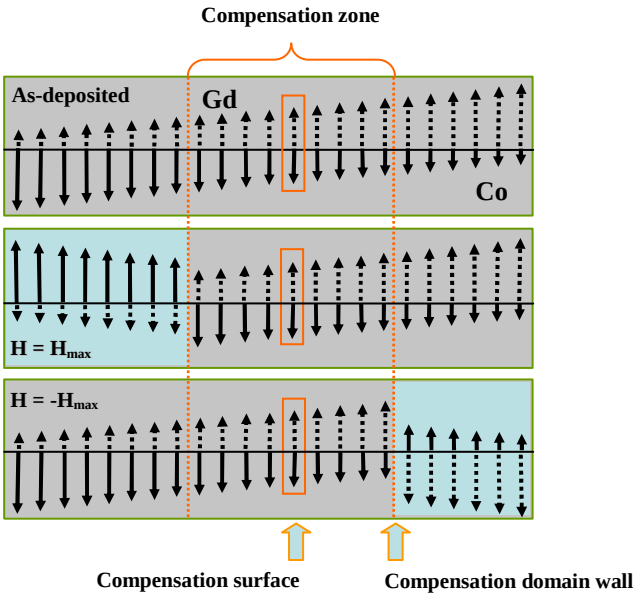

Fig. 3.4. The creations of compensation domain walls and compensation zone in the $Gd_{1-x}Co_x$ thin film. Gd and Co sublattice magnetisations are respectively described as the dash and solid arrows. The applied field H is perpendicular to the film.

Although there are two compensation domain walls at each temperature, they cannot be seen at the same time. Since the walls only exist with the applied field, which only creates one type of wall, if the first compensation domain wall is observed with a perpendicular applied field of H_{max}, the other can be seen with the opposite applied field $-H_{max}$. The zone of thin film surrounded by the two compensation domain walls is called compensation zone. Because the width of compensation zone is the distance between the two compensation domain walls, it depends on the applied field. The larger the applied field is, the narrower the compensation zone is. The creations of compensation walls and compensation zone are illustrated in Fig. 3.4. The compensation surface is always located in the middle of the compensation zone.

3.4.3. Experimental results of $Gd_{1-x}Co_x$ thin films with compensation surface, compensation domain wall, and compensation zone

In order to locate the position of the compensation domain walls on the sample, a dc field (0.1 Tesla) was applied perpendicular to the film plane. The polar Kerr image at room temperature of compensation zone is shown in Fig. 3.5. The two compensation domain walls (dash lines) are observed very clearly when the applied field is reversed from H_{max} to $-H_{max}$. The compensation surface cannot be directly imaged but it always locates in the middle of the compensation zone and between the two compensation domain walls. The existence of two

compensation domain walls proves the existence of a compensation surface on our sample. When looking in detail at Fig. 3.5, the compensation zone embedded between both compensation domain walls keeps a constant contrast when applying the field. The compensation zone is unaffected by the applied field because of its larger-than-H_{max} coercive field. However, the width of the compensation zone depends on the maximum value of applied field. The increasing of H_{max} makes the width of compensation zone decrease.

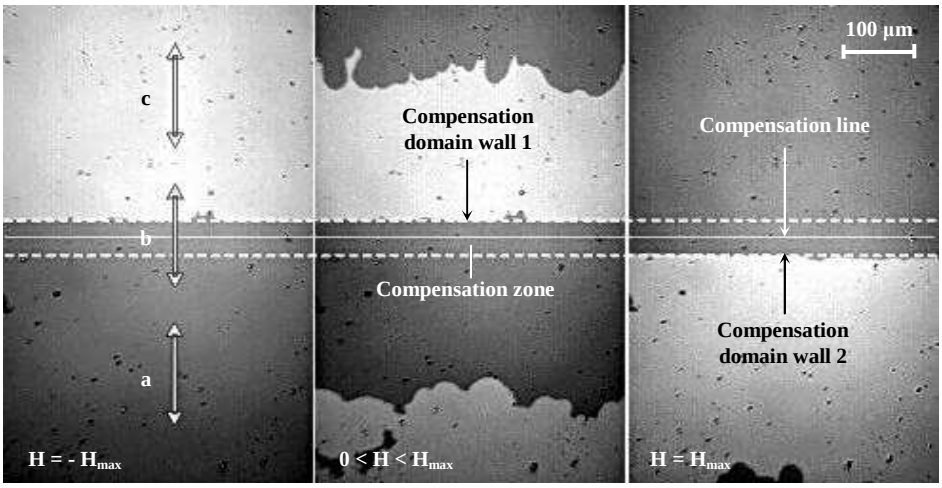

Fig. 3.5. Polar Kerr images at room temperature of the compensation zone under an applied field perpendicular to the film. (a), (b) and (c) denote three locations for the extraordinary Hall effect measurements.

During the reversal of applied field, the domain propagation always starts from the edge of sample toward the compensation zone (see middle picture in Fig. 3.5), because away from the compensation surface the H_C is lower. So the compensation domain walls are stable, i.e. that created wall is still present when setting the field to zero and when the temperature is kept constant.

3.4.4. Study the compensation surface by means of EHE

In magnetisation, the Gd-dominant and Co-dominant zones are separated by the compensation surface. They produce opposite contrasts not only in PKE but also in EHE. At room temperature, three EHE measurements have been carried out at three specific locations (a), (b), and (c) on the sample. Two locations (a) and (c) are chosen at two different sides with respect to the compensation surface while the location (b) lies across it (Fig. 3.5). As expected the EHE has opposite sign in (a) and (c) locations. The complicated shape of EHE loop measured at location (b) relates to the domain propagation around the compensation zone (Fig. 3.6). The detail study of EHE of the $Gd_{1-x}Co_x$ thin film will be presented in chapter 4.

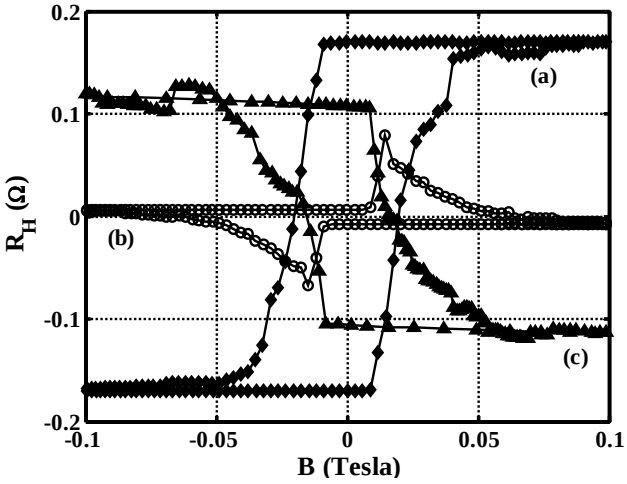

Fig. 3.6. The extraordinary Hall effect loops at room temperature measured at three different locations (a), (b), and (c) presented in Fig. 3.5.

3.5. The displacement of the compensation domain walls and the determination of the in-plane composition gradient

Using mean-field calculation to evaluate the spin-flop regime, a consequence of the uniaxial anisotropy (with $K_1 \approx 1500$ J/m^3) is that the spin-flop transition is not evidenced below 0.8 Tesla (see Fig. 4.18). It means that Gd and Co sublattices always stay antiparallel (the spin-flop does not happen) in applied fields below 0.1 Tesla (PKM field).

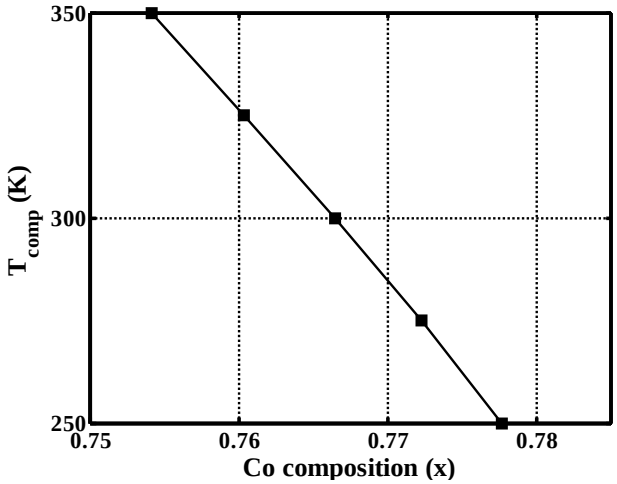

Fig. 3.7. Composition dependence of the compensation temperature (T_{comp}) calculated by mean-field model for $Gd_{1-x}Co_x$ alloys.

The composition dependence of T_{comp} calculated by mean-field model is presented in Fig. 3.7. A 1% change of composition is equivalent to a 40 K shift of the compensation temperature. The displacement of the compensation surface when the temperature is changed can be clearly evidenced by studying it at a fixed applied field. Because the compensation

domain walls always appear near the compensation surface, instead of seeing the movement of the compensation surface, we image the movement of the compensation domain wall when the temperature is changed.

In order to get precise determination of the gradient, the compensation surface is displaced by heating the film under a constant applied field 0.1 Tesla. We measured the in-plane displacement of the compensation domain wall to be 28 μm/K (Fig. 3.8). Comparing with the estimated 40 K/% shift of T_{comp} with composition, we find a 0.9 %/mm composition gradient.

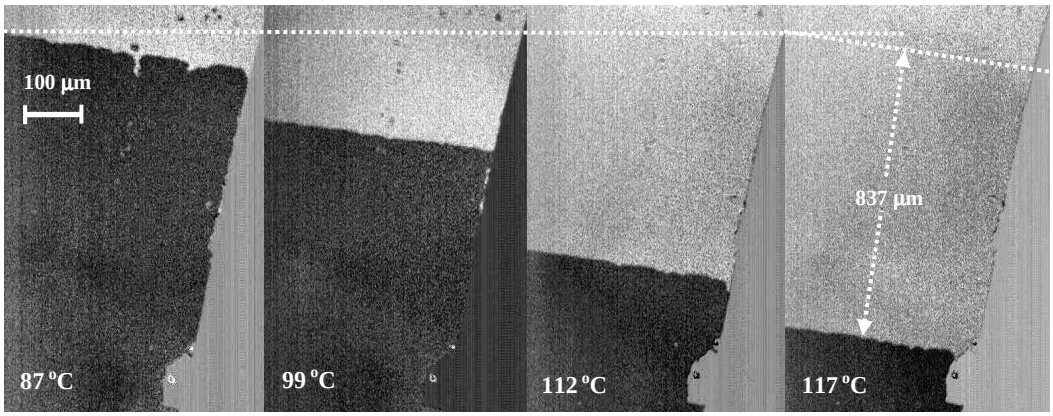

Fig. 3.8. Kerr images of the movement of the compensation domain wall when the temperature is changed under a fixed applied field of 0.1 Tesla.

Since the preferred composition is close to the compensation composition (absence of demagnetising fields) and because of the uniaxial character of anisotropy, compensation walls should be close to ideal 180° Bloch wall, whatever the film thickness. No transition to Néel wall is expected reducing the thickness of in-plane anisotropy GdCo films.

3.6. Conclusion

We have succeeded in designing, in a reproducible way, samples with in-plane composition gradient. It allows to introduce a compensation surface and to manipulate it. So a new micromagnetic object has been introduced for studying the role of magnetisation in magnetic effects relevant to spintronics especially. The in-plane composition gradient associated to a compensation surface allows the tuning of M_S either by heating up or by scanning the sample at constant temperature. Additionally, the compensation domain walls are ideal 180° domain walls because they are very stable and can be moved easily under control by changing the temperature in a constant applied field. They will be useful for studying and controlling a single domain wall as current-induced switching [47] and current-induced RF oscillations [48]. Manipulating a single domain wall has also opened new perspectives in magnetic logic [49] and recording [50].

Chapter. 4. Magnetic properties and the extraordinary Hall effect of amorphous $Gd_{1-x}Co_x$ thin films

4.1. Introduction

The extraordinary Hall effect (EHE) of $Gd_{1-x}Co_x$ alloys has been studied in the 1970s. All of those studies have been carried out in low applied fields where the magnetic sublattices are collinear and the spin-flop phenomenon cannot occur. As regards the relative contributions of the R (Gd) and T (Co) atoms to EHE, no direct experiment has been performed and the literature results are based on the analysis of material series to get the order of magnitude of both contributions.

This chapter describes the study of the EHE of $Gd_{1-x}Co_x$ thin films in applied fields up to 6 Tesla. The magnetic characterisation of samples will be shown and combined with the magnetisation mean-field calculation for interpreting the results of the extraordinary Hall effect. The contributions of Co and Gd sublattice magnetisations to EHE will be quantitatively estimated. Since the spin-flop field decreases significantly in the vicinity of the compensation temperature (T_{comp}), the spin-flop phenomenon can be observed well by means of EHE in our available applied field.

4.2. The amorphous $Gd_{1-x}Co_x$ thin film fabrication and characterisation

The films studied in this chapter were sputtered using a combination of two target compositions $Gd_{10}Co_{80}$+$Gd_{14}Co_{86}$ to get a compensation temperature near 200 K. The sputtering conditions are exactly the same as the conditions used in chapter 3. During deposition, the Si substrates were installed at the center of substrate holders to get the film with highest composition homogeneity. Two different thin films have been used for this work:

- The first thin film, Si\GdCo (100 nm), is named S1. In order to measure the magnetic moment easily by SQUID magnetometer especially near T_{comp}, the film must be large enough, that is why we have not done lithography and etching on sample S1. It has been cut in a square shape of 2×2 mm^2, and then be used for all measurements including SQUID magnetometry and transport properties measurements.
- The second film, Si\Ta (14 nm)\GdCo (100 nm)\Ta (8 nm), has been deposited in the same sputtering condition as S1. By using Ta capping and buffer layer, the film can be protected from oxidation. The sample was then patterned by the UV lithography and the Ar ion beam etching to reduce the effective area of measurement (the width of the

patterned line is 50 μm). The patterned sample is S2 and includes two zones S2a and S2b for measuring Hall effect. The distance between S2a and S2b is about 2 mm (see Fig. 4.1).

The patterned sample S2 is used only for the transport properties measurement, since it is not large enough to be measured by common magnetometers VSM or SQUID. The experimental results of patterned sample S2 will be compared to the results measured on unpatterned sample S1 for evaluating the influence of compositional inhomogeneity on the transport properties of $Gd_{1-x}Co_x$ thin films.

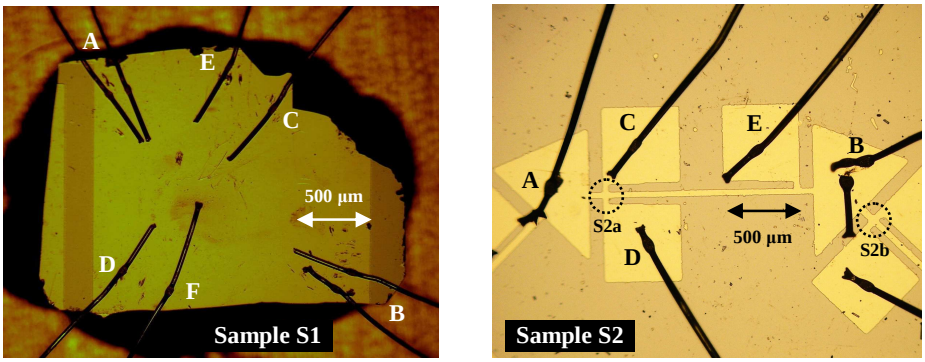

Fig. 4.1. The electric contacts on the samples S1 and S2 (including two zones S2a and S2b with the same measurement area of 50×50 μm^2). A dc current is applied to A and B. Hall voltage is measured from contacts C and D. The resistance can be measured also from contacts C and E.

All the Hall effect measurements have been carried out in two directions of applied field, perpendicular and parallel to the film plane. The applied field can be adjusted from -6 T to 6 T with a minimum step of 0.001 T by using a superconducting coil. The temperature dependence of EHE has been measured from 5 K up to 300 K. In order to separate MR signal and EHE signal from each other, the data processing method described in section 2.10.3.a has been applied for all experimental data of both sample S1 and S2 (Hall signal is odd, MR signal is even).

4.3. Microstructure of sputtered $Gd_{1-x}Co_x$ thin films

The X-ray diffraction patterns at room temperature are shown in Fig. 4.2. There is no fundamental difference between the film spectrum and the one of a bare substrate. The largest peak near 82^o is Si(004). All the narrow peaks are due to other wavelengths (e.g. 74^o is Co K_β) because the X-ray beam is filtered, not monochromated. No Bragg peak potentially arising from a crystalline $Gd_{1-x}Co_x$ alloy is identified. This confirms the amorphous structure of the sputtered $Gd_{1-x}Co_x$ thin films. Finer measurements using a monochromated beam and better signal/noise ratio or EXAFS could be performed to get information about the short range order and local atomic order.

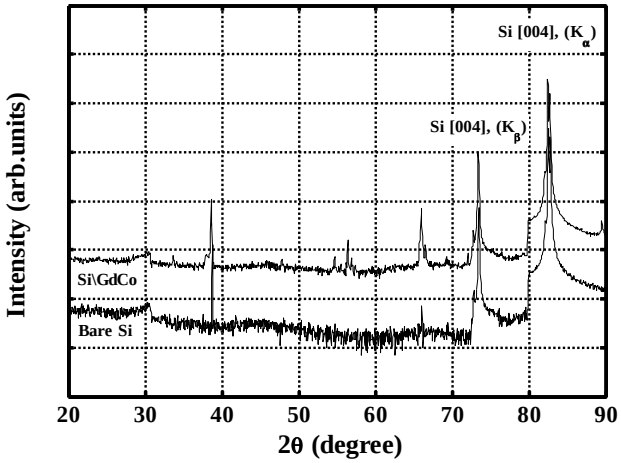

Fig. 4.2. The X-ray diffraction spectra (using a Co anode diffractometer) at 300 K of an as-deposited Si\Gd$_{1-x}$Co$_x$ thin film and a bare Si substrate.

The perpendicular magnetic anisotropy of thin films is investigated by means of Polar Kerr microscopy (PKE) at room temperature. Fig. 4.3 shows the remanent state of the film in PKE microscopy. The contrast shows two directions (up and down) of domain magnetisations. It is a direct proof of spontaneous perpendicular magnetisation at room temperature, so the perpendicular anisotropy here is larger than demagnetising effect.

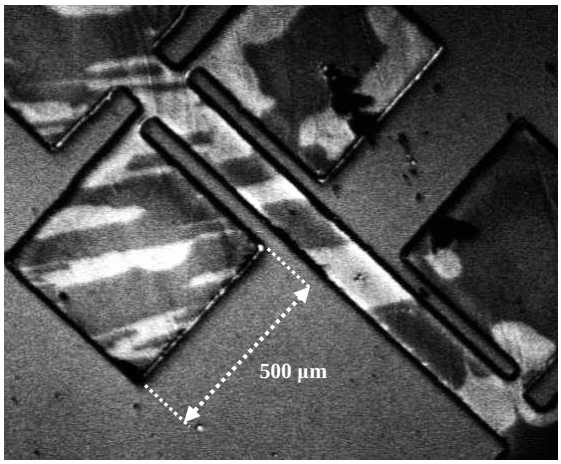

Fig. 4.3. Polar Kerr image of perpendicular domain structure of a patterned Gd$_{1-x}$Co$_x$ thin film at room temperature.

4.4. The sign reversal of the extraordinary Hall effect at T$_{comp}$

The EHE measurements have been carried out on the unpatterned sample S1 between 10 K and 300 K. The Hall resistivity was determined using $\rho_H = V_H t/I$ where t is the film thickness, I is the applied current, and V_H is the Hall voltage. The field dependence of the Hall resistivity (ρ_H) at 10 K and 300 K is sketched in Fig. 4.4. We can see the sign reversal of Hall

effect from negative at 10 K to positive at 300 K. At the field of 0.6 Tesla, the amplitudes of ρ_H at 10 K (ρ_H = 3.4 μΩ.cm) and 300 K (ρ_H = 3.3 μΩ.cm) are nearly the same. However, ρ_H is nearly fully remanent at 300 K while it is zero-remanent at 10 K.

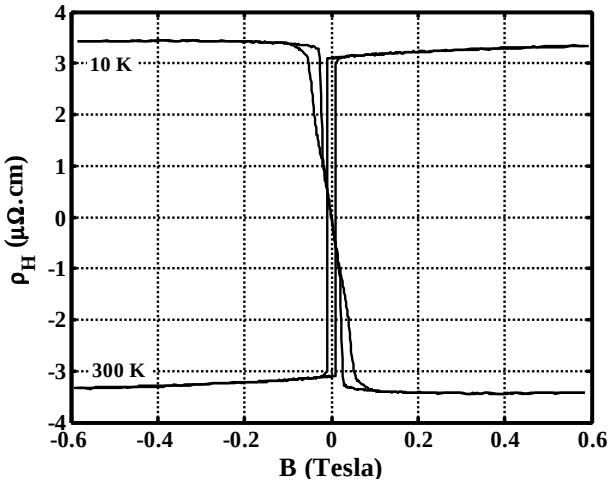

Fig. 4.4. Hall resistivity loops at 10 K and 300 K for S1 sample.

The temperature dependence of the normalised saturation magnetisation of sample S1 under an applied field of 0.1 Tesla measured by SQUID magnetometer is presented in Fig. 4.5. Since there is a significant reduction of magnetisation in vicinity of T_{comp}, the signal becomes noisy in the range of temperature from 200 K to 240 K. However, T_{comp} can be approximately interpolated from both sides to zero and was found as T_{comp} = 225 K for the sample S1. Below 225 K, the magnetisation is Gd-dominant and it turns into Co-dominant above 225K.

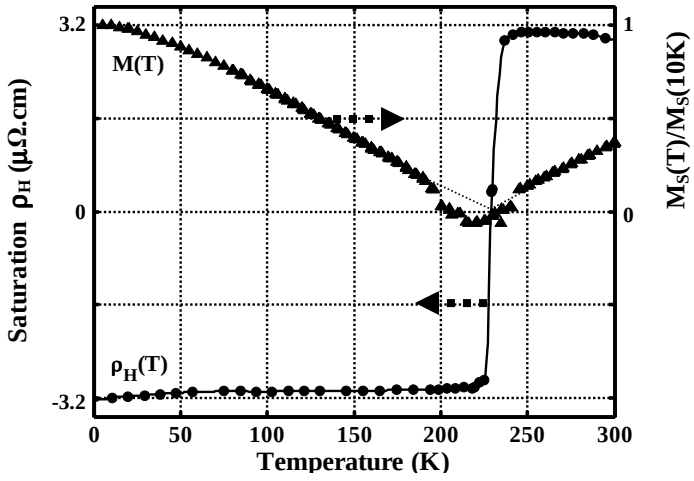

Fig. 4.5. The temperature dependences of the maximum Hall resistivity and the normalised magnetisation of sample S1. A 0.01 Tesla field is applied perpendicular to the film during SQUID measurements.

The temperature dependence of the saturation ρ_H (before spin-flop) imported from EHE

loops is also presented in Fig. 4.5 to compare with the magnetisation curve. Above T_{comp}, the sample magnetisation is Co-dominant and the EHE is positive. EHE is negative below T_{comp} when the magnetisation is Gd-dominant. The sign reversal of EHE at T_{comp} says that the contributions of Co and Gd moments to EHE must fulfil one of the three following hypotheses:

- Co moments contribute a positive EHE relative to their magnetisation while Gd moments contribute a negative EHE. In the saturation state above T_{comp}, because of antiparallel orientation of Gd and Co moments, both of them have positive contributions to the film EHE, so the film EHE is positive above T_{comp}.
- Both Co moments and Gd moments contribute positive senses to EHE. In the saturation state above T_{comp}, when Gd and Co moments are antiparallel, Co moments have a positive contribution while Gd moments have a negative contribution to the film EHE. Therefore, the amplitude of contribution from Gd moments must be smaller than the contribution from Co moments for keeping the film EHE positive above T_{comp}.
- Both Co moments and Gd moments contribute negative senses to EHE. In saturation state above T_{comp}, Co moments have a negative contribution while Gd moments have a positive contribution to EHE. Therefore, the amplitude of contribution from Gd moments must be larger than the contribution from Co moments for keeping EHE positive above T_{comp}.

The most likely scenario will be discussed in the next section (4.5.3) where the temperature dependences of the Gd and Co sublattice magnetisations are compared to the temperature dependence of Hall resistivity.

4.5. The contributions of Gd and Co moments to the extraordinary Hall effect

In this section, to evaluate the contributions of Gd and Co sublattice magnetisations (M_{Gd} and M_{Co}) to the extraordinary Hall effect (EHE), a mean-field simulation is applied to calculate the temperature dependences of M_{Co} and M_{Gd} in both samples S1 and S2a at temperatures from 0 K to 300 K. The temperature dependence of the magnetisation of sample S1 measured by SQUID magnetometer is used to adjust parameters in the mean-field calculation. The experimental temperature dependence of the Hall resistivity (ρ_H) is compared to the mean-field calculated M_{Co} and M_{Gd} to figure out the contributions of Gd and Co moments to EHE.

4.5.1. The temperature dependence of magnetisations

In this section, the mean-field equations (1.3.a) are used again to calculate the temperature dependences of the spontaneous magnetisations of samples S1 and S2a. All the required parameters are exactly the same as the parameters used in the simulation for $Gd_{0.20}Co_{0.80}$ alloys in section 1.3.3 except the Gd-Co intersublattice molecular field coefficient

(λ), the Co-Co intrasublattice molecular field coefficient (λ_{CoCo}), and of course the composition (x). Since the samples S1 and S2 are amorphous and their compositions are also different from the sample $Gd_{0.20}Co_{0.80}$, the amplitude of λ and λ_{CoCo} can be quite different and must be determined again. The temperature dependence of the magnetisation of sample S1 measured by SQUID will be used as a reference for specifying those parameters (λ_{CoCo}, λ, x) in order to get the best agreement between data and the mean-field simulation. The obtained results of M_{Gd} and M_{Co} of the sample S2a will be used later to evaluate the contributions of Gd and Co sublatices to the EHE of $Gd_{1-x}Co_x$ alloys.

In the case of unpatterned sample S1, although the substrate was installed at the center of substrate holder during deposition to get the most homogeneous composition, there is still an in-plane composition gradient. According to EDX composition measurement, the Co composition (x) varies from 0.76 to 0.79 (see Table. 3-1). In our calculation, we use x = 0.79 as an initial value, so the initial composition is $Gd_{0.21}Co_{0.79}$. The Curie temperature of the amorphous $Gd_{0.21}Co_{0.79}$ alloy extrapolated from literature data in Fig. 1.4 is T_C = 800 K. An initial value of λ = 125 is interpolated from Fig. 1.7. Since T_C of $Gd_{1-x}Co_x$ depends strongly on x and λ_{CoCo}, but very slightly on λ, in order to find the consequent value of λ_{CoCo} for amorphous $Gd_{0.21}Co_{0.79}$ alloy, the mean-field simulation with λ = 125 and x = 0.79 is used ajusting λ_{CoCo} to fit T_C = 800 K. At last a 850 value for λ_{CoCo} is determined.

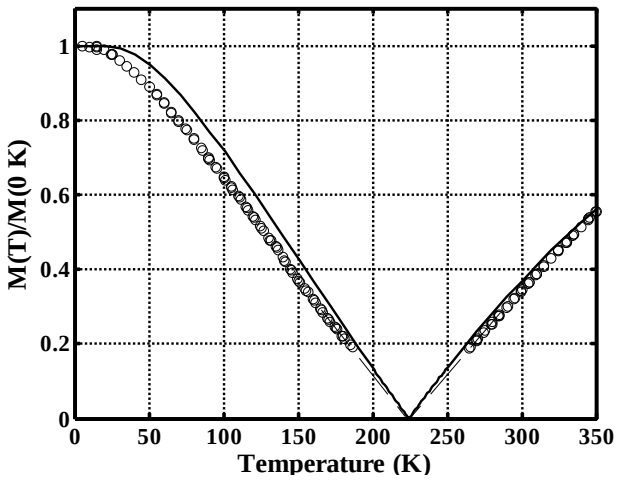

Fig. 4.6. The normalised spontaneous magnetisation of $Gd_{0.22}Co_{0.78}$ (λ_{CoCo} = 850, λ = 118) calculated by the mean-field theory (solid line) and the normalised saturation magnetisation of the sample S1 measured by SQUID (open circles) under an applied field of 0.1 T perpendicular to the film.

Different from the Co-Co intrasublattice molecular field coefficient λ_{CoCo} (having a strong effect on T_C and a slight influence on T_{comp}), the Gd-Co intersublattice molecular field coefficient λ has a more significant influence on T_{comp}. According to the SQUID measurement, the compensation temperature of sample S1 is T_{comp} = 225 K. For getting the most consequent

value of λ, all available parameters (x = 0.79, λ_{CoCo} = 850) are inserted again in the mean-field calculation and λ is adjusted to get T_{comp} = 225 K. Finally we find λ = 120.

In the case of sample S1, for getting the best agreement between the mean-field calculation and experimental results, x and λ continue to be adjusted slowly and precisely. Eventually we obtain x = 0.78 and λ = 118 for the sample S1. The calculated spontaneous magnetisation (λ_{CoCo} = 850, λ = 118, x = 0.78) and the experimental saturation magnetisation are both normalised by the values at 0 K and presented in Fig. 4.6. There is some deviation between calculation and experiment. The maximum deviation is about 8% at temperatures from 50 K to 100 K where the calculated values is larger than the experimental values. The disagreement between mean-field calculation and experiment might be due to the following reasons (see pages 346-352 in ref.[4]):

- The structural disorder in amorphous alloys induces a fluctuation of the exchange coefficients that causes a pronounced flattening of $M_{Gd}(T)$ and $M_{Co}(T)$ curves and makes them lies substantially below the curves calculated by mean-field theory where the fluctuations are not taken into account.
- At low temperature, the impact of spin-wave excitation is very important. So the experimental M(T) curve has a stronger T-dependence comparing to the curve calculated by the mean-field model which does not account for the spin-wave excitation, i.e. the experimental M(T) curve lies substantially below the mean-field calculated M(T) curve (see Fig. 1.3 and refs. [3]-[4] for further evidences).

Both reasons above make the experimental magnetisation M(T) curve more flat and lying below the curve calculated by mean-field theory. Therefore, in our calculation, the calculated values of normalised magnetisation are always larger than the experimental values. The deviation is smaller than 10%.

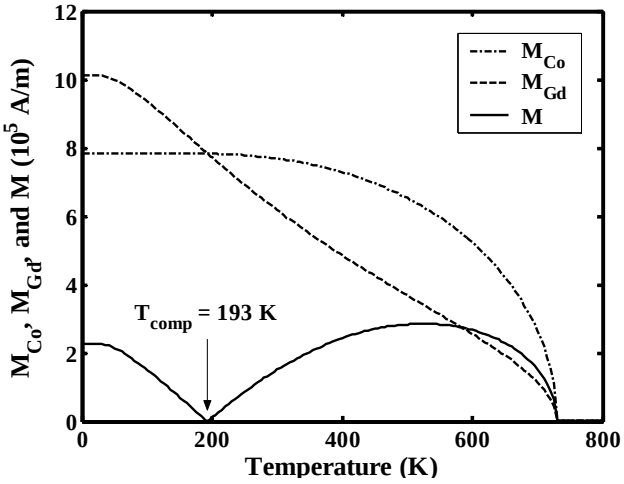

Fig. 4.7. The temperature dependence of the magnetisations M_{Gd}, M_{Co}, and M of the sample S2a

($Gd_{0.21}Co_{0.79}$) calculated by the mean-field model with λ_{CoCo} = 850, λ = 118.

In the case of patterned sample S2, because of its very small area, its magnetisation cannot be measured by SQUID magnetometry. However, because the samples S1 and S2 were deposited in the same sputtering condition, the difference between S1 and S2 should be small. It means that all parameters (λ_{CoCo} = 850, λ = 118, …) except x of sample S1 can be used in the calculation for sample S2a. According to the EHE measurement of sample S2a, a compensation temperature T_{comp} = 193 K has been found. By adjusting the composition x in the mean-field calculation, we find T_{comp} = 193 K with x = 0.79, it is corresponding to the alloy composition of $Gd_{0.21}Co_{0.79}$. The mean-field calculation result of sample S2a (λ_{CoCo} = 850, λ = 118, x = 0.79) is presented in Fig. 4.7. So a difference of 1% in composition between S1 and S2 is expected.

Noticing that the compensation temperature (T_{comp}) imported from magnetisation curves is sometimes different from the T_{comp} imported from EHE curves. The reason is that the magnetisation measurement is macroscopic (averaged over the film) whereas the EHE measurements is localised (the EHE measurement area is quite small in comparison with the whole sample). The T_{comp} taken from EHE curves and magnetisation curve must coincide if the composition gradient is zero. That is why, in the case of sample S1, the magnetisation curve gives T_{comp} = 225 K (Fig. 4.6) while the EHE curve gives T_{comp} = 235 K (Fig. 4.20). In order to get a compensation temperature T_{comp} = 235 K, i.e. to achieve a good agreement with EHE, the composition of sample S1 must be adjusted to x = 0.777 (instead of 0.78).

4.5.2. Temperature dependences of the Hall resistivity (ρ_H) and the longitudinal resistivity (ρ) of $Gd_{1-x}Co_x$ thin films

The ordinary part of Hall effect in metallic alloys such as $Gd_{1-x}Co_x$ can be neglected because the conduction carrier density is very large (Assuming that there is one conduction electron per atom, the conduction electron density of $GdCo_4$ crystal will be $n \approx 6.5128\times10^{28}$ e/m^3. The ordinary Hall coefficient, in this case, will be $R_o = 1/(ne) = 1/(6.5128\times10^{28}\times1.6022\times10^{-19}) = 0.9583\times10^{-10}$ Ωm/T = 0.9583×10^{-2} $\mu\Omega$.cm/T. Under an applied field of 1 Tesla, the ordinary part of Hall resistivity is about 0.01 $\mu\Omega$.cm, this is very small and negligible in comparison with the EHE part of $Gd_{1-x}Co_x$ thin film with about 3 $\mu\Omega$.cm in magnitude). So the formula (1.18) can be written again for $Gd_{1-x}Co_x$ alloys as:

$$\rho_H = \mu_o R_{Gd} M^z_{Gd} + \mu_o R_{Co} M^z_{Co} \qquad \textbf{(4.1)}$$

Where M^z_{Gd} and M^z_{Co} are the z-components of Gd and Co sublattice magnetisations, respectively. The Hall resistivity (ρ_H) is also governed by the longitudinal resistivity (ρ) as described in formula (1.17). During the variation of temperature, M^z_{Gd}, M^z_{Co}, and ρ change

and lead to the T-dependence of EHE amplitude.

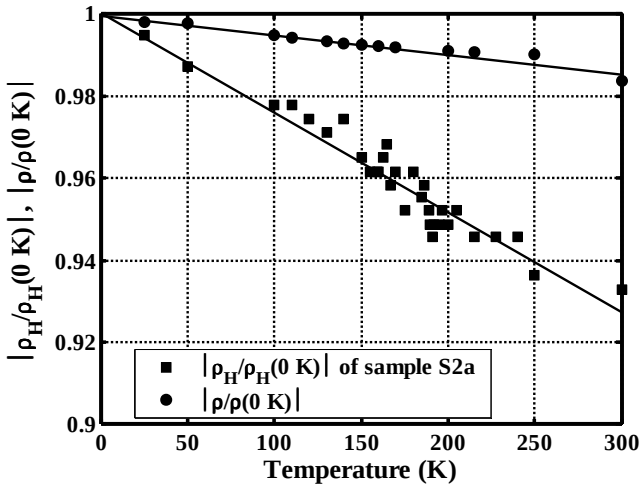

Fig. 4.8. The temperature dependences of the ratios ρ/ρ(0 K) (solid circles) and ρ_H/ρ_H(0 K) (solid squares) of the patterned sample S2a. The solid lines present the linear approximations.

In our transport measurement system, the lowest temperature is about 2 K. The results at 0 K of ρ and ρ_H extrapolated from the experimental results of samples S1 and S2 are ρ(0 K) = 200 μΩcm and ρ_H(0 K) = 3.2 μΩcm. The temperature dependence of two ratios ρ_H/ρ_H(0 K) and ρ/ρ(0 K) of the patterned sample S2a are presented in Fig. 4.8. In the linear approximation, ρ and ρ_H can be fitted as (solid lines in Fig. 4.8):

$$\rho/\rho(0\ K) = (1 - 0.383\times10^{-4}\times T) \text{ and } \rho_H/\rho_H(0\ K) = (1 - 2.417\times10^{-4}\times T) \quad \textbf{(4.2)}$$

When the temperature increases from 0 K to 300 K, the variation of ρ is about -1.5%, it is much smaller than that of ρ_H (-7.5%). In an effort to estimate the quantitative contributions of Gd and Co to EHE, in our calculation, ρ will be considered as a constant in this range of temperature, i.e. the impact of the T-dependence of ρ on the T-dependence of ρ_H will be neglected. So the T-dependence of ρ_H is mainly subject to the T-dependences of the z-components of Gd and Co sublattice magnetisations.

4.5.3. The contribution of Gd and Co moments to EHE

In order to estimate the contributions of Gd and Co moments to EHE, R_{Gd} and R_{Co} are assumed constants below 300 K. This assumption is reasonable because the longitudinal resistivity ρ is nearly constant below 300 K.

Fortunately, below 300 K the temperature dependences of M_{Gd} and M_{Co} are very different. (The T-dependence of M_{Gd} is stronger than the T-dependence M_{Co}), so the contributions of Gd and Co to EHE can be estimated by comparing the M_{Gd}(T) and M_{Co}(T) curves to the ρ_H(T) curve in the range of temperature from 0 K to 300 K as presented hereafter.

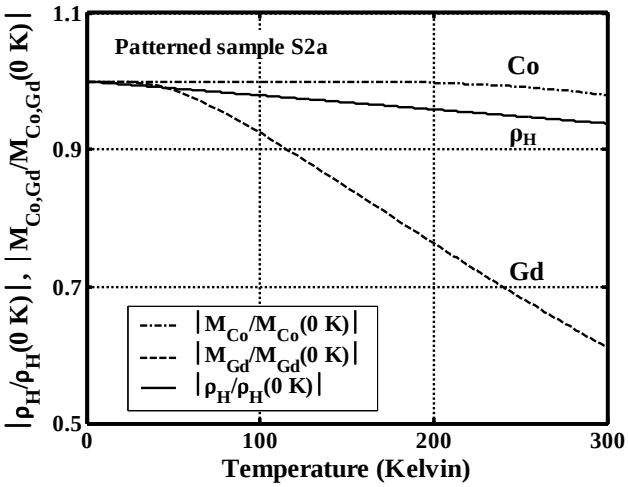

Fig. 4.9. The temperature dependences of the term $\rho_H/\rho_H(0\ K)$ (solid line) calculated by using formula (4.2) and the normalised Gd (dashed line) and Co (dash-dot line) sublattice magnetisations calculated by mean-field theory for the patterned sample S2a ($Gd_{0.21}Co_{0.79}$).

Although the Hall resistivities (ρ_H) of both samples S1 and S2 (S2a and S2b) have been investigated as a function of temperature, in this section, only the $\rho_H(T)$ curve of patterned sample S2a is used to compared to the M_{Gd} (T) and $M_{Co}(T)$ curves calculated by mean-field model (see Fig. 4.7). In order to compare easily M_{Gc}, M_{Co} and ρ_H, they are normalised by their values at 0K and then presented in Fig. 4.9. At low temperature (below 50 K) the mean-field calculation is not very correct because the magnetic excitation such as spin waves is not taken into calculation, it looks "too flat" while the normalised ρ_H keeps decreasing. In the range of temperature from 50 K to 300 K, we find $d\rho_H/dT$ = -2.4%/100K, dM_{Co}/dT = -0.7%/100K, dM_{Gd}/dT = -13.0%/100K.

As a new expression, the formula (4.1) can be written again as:

$$\rho_H / \rho_H(0\ K) = a.M^z_{Gd} / M^z_{Gd}(0\ K) + b.M^z_{Co} / M^z_{Co}(0\ K) \qquad \textbf{(4.3)}$$

where $a = \frac{\mu_o M^z_{Gd}(0\ K) R_{Gd}}{\rho_H(0\ K)}$ and $b = \frac{\mu_o M^z_{Co}(0\ K) R_{Co}}{\rho_H(0\ K)}$. Please notice that in the cases of our thin films with perpendicular anisotropy, when an external field ($\vec{H}$) smaller than the spin-flop field is applied perpendicular to the film, the vectors $\overrightarrow{M_{Gd}}$, $\overrightarrow{M_{Co}}$, and $\vec{H}$ are collinear. It means that $\left|M^z_{Gd}\right| = \left|\overrightarrow{M_{Gd}}\right| = M_{Gd}$ and $\left|M^z_{Co}\right| = \left|\overrightarrow{M_{Co}}\right| = M_{Co}$ (e.g. when T > T_{comp}, $M^z_{Gd} = -M_{Gd} < 0$ and $M^z_{Co} = -M_{Co} > 0$), i.e. we can investigate the T-dependences of $M_{Gd,Co}$ instead of their z-components $M^z_{Gd,Co}$ but taking into account the sign reversal of $M^z_{Gd,Co}$ at T_{comp}.

Because the signs of ρ_H, M^z_{Gd}, and M^z_{Co} all reversed at T_{comp}, the equation (4.3) is equivalent to

$$\left|\rho_H / \rho_H(0\,\mathrm{K})\right| = a\left|M^z_{Gd} / M^z_{Gd}(0\,\mathrm{K})\right| + b\left|M^z_{Co} / M^z_{Co}(0\,\mathrm{K})\right| \qquad \textbf{(4.4)}$$

$$= a\left|M_{Gd} / M_{Gd}(0\,\mathrm{K})\right| + b\left|M_{Co} / M_{Co}(0\,\mathrm{K})\right|$$

Using formula (4.4) and the values of $d\rho_H/dT$, dM_{Co}/dT, and dM_{Gd}/dT at temperatures from 50 K to 300 K, the constants a and b can be found as: a = 0.14 and b = 0.86.

According to the experiment, the Hall resistivity of sample S2a at 0 K is $\rho_H(0\ \mathrm{K}) = -3.2\times10^{-8}\ \Omega\mathrm{m}$. Using mean-field calculation and taking into account the antiparallel alignment between $\overrightarrow{M_{Gd}}$ and $\overrightarrow{M_{Co}}$ for the sample S2a (Gd-dominant) we find: $M^z_{Co}(0\,\mathrm{K}) = -M_{Co}(0\ \mathrm{K}) = -7.8456\times10^5$ A/m and $M^z_{Gd}(0\,\mathrm{K}) = M_{Gd}(0\ \mathrm{K}) = +10.126\times10^5$ A/m. So the sublattice Hall coefficients can be found as:

$$R_{Gd} = \frac{a\rho_H(0\,\mathrm{K})}{\mu_o M^z_{Gd}(0\,\mathrm{K})} = -3.5\times10^{-9}\ (\Omega\mathrm{m}^2/\mathrm{A}). \qquad \textbf{(4.5.a)}$$

$$R_{Co} = \frac{b\rho_H(0\,\mathrm{K})}{\mu_o M^z_{Co}(0\,\mathrm{K})} = 27.9\times10^{-9}\ (\Omega\mathrm{m}^2/\mathrm{A}). \qquad \textbf{(4.5.b)}$$

In summary, we can conclude for $Gd_{1-x}Co_x$ alloys that, Co moments make positive sense ($R_{Co} > 0$) while Gd moments make negative sense ($R_{Gd} < 0$) to the extraordinary Hall effect. Above T_{comp}, because the magnetisation is Co dominant, both of Co and Gd moments have positive contributions to EHE, so EHE is positive. In the contrary, EHE is negative below T_{comp}. In magnitude of EHE, the contribution from Gd moments is quite small comparing to the contribution from Co moments ($|R_{Gd}/R_{Co}| = 12\%$).

4.6. The extraordinary Hall effect at low temperatures

4.6.1. The EHE of the unpatterned sample S1 at low temperatures

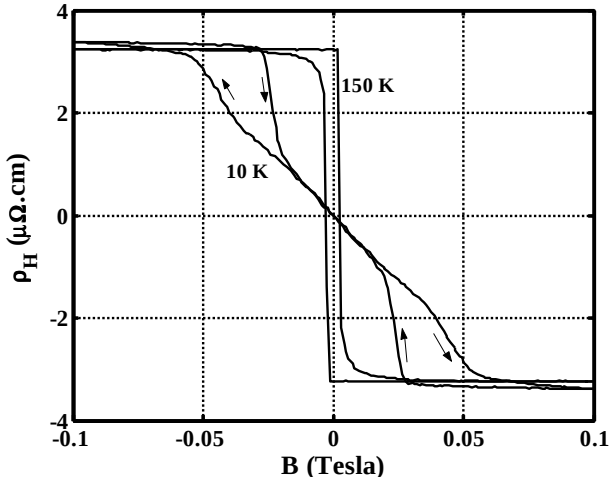

Fig. 4.10. The low field EHE hysteresis curves of the unpatterned sample S1 (T_{comp} = 235 K) at 10 K and 150 K. B is perpendicular to the film.

The EHE loops of the unpatterned sample S1 at 10 K and 150 K (Fig. 4.4) are zoomed in vicinity of zero applied field and presented in Fig. 4.10. The remanent ρ_H at 10 K is zero whereas ρ_H is fully remanent at 150 K. Two possibilities can be thought of to explain the decrease of the remanent ρ_H at low temperature:

- The first: At low temperatures, the increase of the spontaneous magnetisation increases the demagnetising energy. When the demagnetising field is strong enough to overcome the anisotropy, the spontaneous magnetisation tilts in-plane. Because the perpendicular component of remanent magnetisation is zero, the remanent EHE becomes zero as a consequence.
- The second: The film still has still perpendicular magnetisation at 10 K. However, with the increase of spontaneous magnetisation, at zero field the sample becomes multidomain to decrease the total demagnetising energy. The magnetic structure in this case is similar to the case of magnetic bubble or stripe films. On account of this magnetic structure (50% domains up and 50% domains down), the remanent magnetisation and the remanent EHE become zero.

The real magnetic structure of sample S1 at low temperature will be discussed in the next sections where the in-plane EHE curves of the sample S1 at low temperature and the specific magnetisation curve of bubble thin film are shown and compared.

4.6.2. The low-temperature EHE of the sample S1 under an in-plane applied field

In order to determine the magnetism of sample S1 at low temperature, the EHE has been measured with an in-plane applied field. The applied magnetic field is parallel to the film

and varies from -6 T to 6 T in the temperature from 5 K to 300 K. The EHE loops at 10 K, 100 K, 150 K, and 230 K are shown in Fig. 4.11.

At 150 K and above (Fig. 4.11.b), the remanent ρ_H is equal to the saturation ρ_H in the cases of perpendicular applied field measurements (ρ_H = 3.2 μΩ.cm) presented in Fig. 4.4. It proves that, without applied field, the magnetisation of sample S1 is fully perpendicular to the film, i.e. the sample has perpendicular anisotropy. When the in-plane applied field increases and overcomes the anisotropy field, the total magnetisation is turned in to in-plane. Therefore, the perpendicular component of magnetisation is decreased, and EHE is consequently decreased. Recently, similar phenomenon was reported by N. H. Duc et al for the amorphous TbFeCo thin films [51].

Noticing that, experimentally it is impossible to apply the external field exactly parallel to the film plane (the applied field is tilted a few degrees from the film plane), so the out-of-plane symmetry of magnetisation is broken. The sign of ρ_H therefore depends on the deviation between the applied field and the film plane. That is why the remanent ρ_H can be positive or negative, not depending on the temperature above or below T_{comp} (Fig. 4.11 shows a positive ρ_H at 150 K and 230 K even though these temperatures are below T_{comp} = 235 K), nevertheless, the sign of ρ_H always reverse at T_{comp}. Since only the out-of-plane components of Gd and Co magnetisations contribute to EHE, ρ_H is expected to be zero when the film is really in-plane saturated. However, because of the slight misalignment applied field in the in-plane magnetisation process, the EHE is not zero even in saturation state.

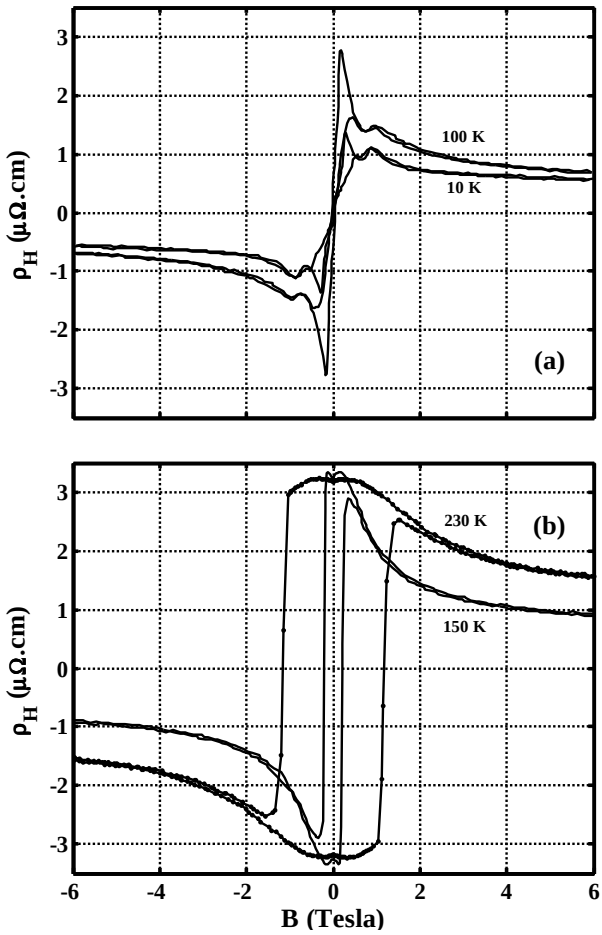

Fig. 4.11. The in-plane applied field EHE loops at 10 K, 100 K, 150 K, and 230 K of the unpatterned sample S1 (T_{comp} = 235 K).

At 100 K and below (Fig. 4.11.a), the remanent ρ_H is zero. However, when an in-plane external field is applied, the EHE is not zero anymore. The EHE reaches its maximum at about 0.3 Tesla, and decreases after. The maximum ρ_H at 100 K is equivalent to 85% of the maximum ρ_H in the out-of-plane measurement. This phenomenon will be interpreted in the next section.

4.6.3. The perpendicular multidomain structure of sample S1 at low temperatures

Let's assume that the sample has in-plane anisotropy at 100 K and below. In the case of zero applied field, since there is no perpendicular component of magnetisation, the EHE must be zero. When an in-plane external field is applied, in order to reach EHE values at 0.3 Tesla close to the maximum ρ_H (85% at 100 K and 50% at 10 K), the sublattice magnetisations of Gd and Co must be out-of-plane oriented. There is one and only possibility: The spin-flop occurs at 0.3 Tesla, and after spin-flop, the total magnetisation is still in-plane but the Gd and Co sublattice magnetisations must be out-of-plane. Nevertheless, the spin-flop phenomenon is unlikely to happen at 0.3 T for the following reasons:

- A minimum spin-flop field B_{sf} as large as 0.8 Tesla (calculated with K = 1500 J/m^3)

is obtained at T_{comp} = 225 K. Therefore, B_{sf} would be several tens of Tesla at 100 K (B_{sf} = 35 T calculated at 100 K). A spin-flop field of 0.3 T at 100 K is impossible.

- Because the total magnetisation of the sample at 10 K is much larger than the magnetisation at 100 K, B_{sf} at 10 K must be very much larger than B_{sf} at 100 K (B_{sf} = 48 T calculated at 10 K). This is completely different from the experimental results where the B_{sf} is equal to 0.3 Tesla for both temperatures 10 K and 100 K.

So that the sample S1 cannot have in-plane anisotropy at 100 K and below. On the contrary it must have perpendicular anisotropy. In order to have zero remanent ρ_H, the magnetism of sample S1 at low temperature must be a multidomain structure with zero-remanence and 50% of domains are up and 50 % of domains are down. Furthermore, the domain size must be much smaller than the EHE measurement area to have an out-of-plane symmetry of multidomain structure in the EHE measurement area (about 2×2 mm^2 in the case of sample S1 and 50×50 μm^2 in the case of patterned sample S2).

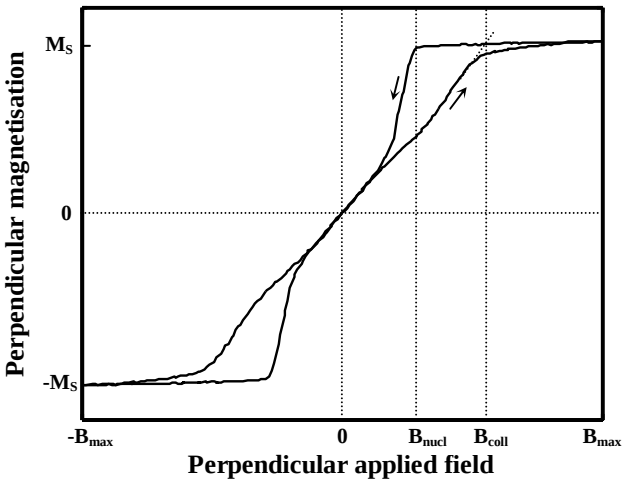

Fig. 4.12. The characteristic out-of-plane applied field hysteresis loop of a bubble thin film where B_{nucl} and B_{coll} are the nucleation field and the collapse field, respectively (see ref. [80] p. 306).

The magnetic structure of sample S1 at low temperature is similar to the magnetic structure of a bubble or stripe thin film. It is obvious if we compare the perpendicular-applied-field EHE loop at low temperatures of the sample S1 (Fig. 4.4) with the characteristic perpendicular-applied-field hysteresis loop of a bubble thin film (Fig. 4.12), the same shape of two loops can be seen clearly where B_{nucl} and B_{coll} are the nucleation field and the collapse field, respectively (ref. [80] p. 306). This similarity and the previous EHE discussion confirm the existence of a perpendicular multidomain structure of the sample S1 at low temperatures and zero-field.

4.6.4. Temperature dependences of the remanent magnetisation and the remanent Hall resistivity of the unpatterned sample S1

The temperature dependence of the remanent ρ_H is presented in Fig. 4.13. The results show that ρ_H is fully remanent above 140 K and its sign reverses at T_{comp} = 235 K. Significantly, the remanent ρ_H starts decreasing from 140 K and nearly disappears at 100 K. It means that below 100 K, there is an out-of-plane symmetry of perpendicular multidomain structure in the EHE measurement area of sample S1, i.e. the domain size in the EHE measurement area is small enough to have 50% domains up and 50% domain down.

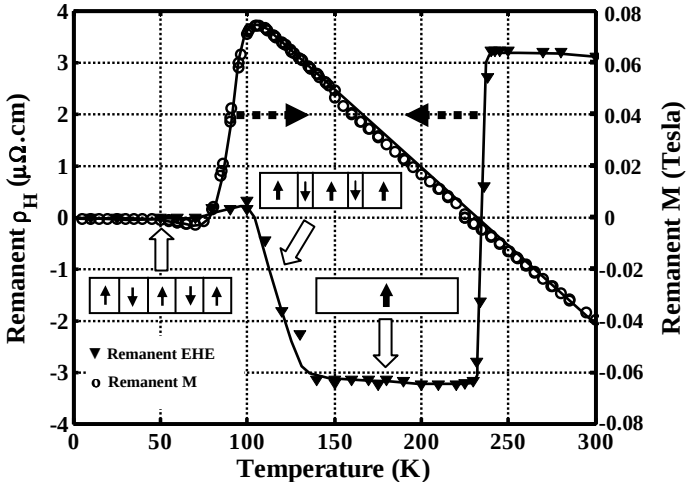

Fig. 4.13. The perpendicular remanent magnetisation M(T, H = 0) (open circles) and the remanent Hall resistivity ρ_H(T, H = 0) (solid triangles) of the sample S1 versus temperature. The insert pictures illustrate the domain structure in the area of EHE measurement.

In order to understand better the domain structrure of sample S1 at low temperatures, its out-of-plane remanent magnetisation has been measured by SQUID in the range of temperature from 5 K to 300 K. This measurement has been divided into two stages of temperature: The temperature decreases from 150 K down to 5 K in the first stage, and in the second stage the temperature increases from 150 K up to 300 K. Before both measurements, the sample was saturated in a perpendicular applied field of 0.1 Tesla at 150 K. The applied field was brought to zero before the beginning of both measurements. The starting temperature of 150 K has been chosen since the sample has a 100% perpendicular remanence at 150 K according to the remanent EHE curve. The perpendicular remanent magnetisation is likewise presented in Fig. 4.13 to compare with the temperature dependence of the remanent ρ_H. The results confirms the disappearance of perpendicular remanent magnetisation at low temperatures. Nevertheless, there is a difference between both curves, it is that the remanent magnetisation start decreasing from 100 K, about 40 K later than the remanent ρ_H does. The cause may be the compositional

inhomogeneity of the sample S1. Actually, the remanent magnetisation is measured on the whole sample while the EHE measurement is just carried out on a small EHE measurement area. When a composition gradient exists on the sample, the measured results of magnetisation overall sample may be different from the results measured on a small area. In summary, if both measurements are carried out on the same area of sample, or if the sample is completely homogeneous in composition, the temperatures where the remanent ρ_H and the perpendicular remanent magnetisation should start decreasing are the same.

4.7. The spin-flop phenomenon and EHE of $Gd_{1-x}Co_x$ alloys in the vicinity of the compensation temperature

A very interesting characteristic of the $Gd_{1-x}Co_x$ thin films in the vicinity of T_{comp} is that the spin-flop field is significantly decreased, therefore it is possible to observe the spin-flop phenomenon with our available applied field. Nevertheless, the closer to T_{comp} the temperature is, the smaller the total magnetisation is, it makes it difficult to investigate the spin-flop phenomenon using magnetometers such as VSM or SQUID, especially in the case of thin films. Fortunately, the extraordinary Hall effect is very sensitive to the perpendicular component of the Co sublattice magnetisation. Once the spin-flop occurs, the Co sublattice magnetisation turns from its direction before spin-flop, so ρ_H is changed as a consequence. That is why the extraordinary Hall effect is very useful for studying phenomena related to rotations of the sublattice magnetisations of $Gd_{1-x}Co_x$ alloys. In this section, EHE will be firstly used as a tool for investigating the spin-flop phenomenon of $Gd_{1-x}Co_x$ thin film. By the way, EHE can be better understood in the non collinear regime after spin-flop.

4.7.1. Critical phenomenon of the extraordinary Hall effect in $Gd_{1-x}Co_x$ thin films

The EHE loops at temperatures below (a) and above T_{comp} (b) for the sample S1 are presented in Fig. 4.14. We can see obviously the jumps of ρ_H at a certain applied field. There is some critical phenomenon occurring inside the sample. The applied fields where the ρ_H jumps occur are called "the critical fields" and abbreviated to B_{crit}. The first question is to know if B_{crit} is the spin-flop field.

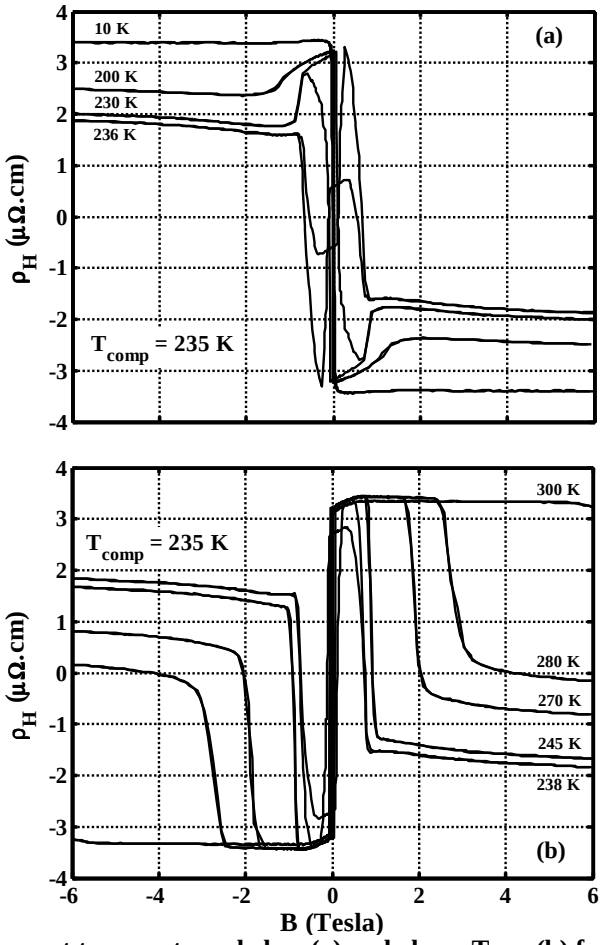

Fig. 4.14. The EHE loops at temperatures below (a) and above T_{comp} (b) for the unpatterned sample S1 with T_{comp} = 235 K. The applied field is perpendicular to the film plane.

We can see that the closer to T_{comp} the temperature is, the smaller the critical field is, this behaviour of the critical field (B_{crit}) is quite similar to the behaviour of the spin-flop field (B_{sf}). In order to check if B_{crit} is B_{sf}, the magnetisation of the sample S1 was measured by SQUID in perpendicular applied fields from 0 T to 5 T at three different temperatures of 270 K, 250 K, and 230 K (close to T_{comp} = 235 K). The dimensions of the unpatterned sample S1 are large enough to have enough signal for the SQUID measurement. The magnetisation curves presented in Fig. 4.15 evidence the spin-flop phenomenon at the three temperatures. This conclusion is based on three sudden increases of magnetisation on three magnetisation curves. The spin-flop fields of sample S1 at 230 K, 250 K, and 270 K are B_1, B_2, and B_3, respectively. The applied field dependences of ρ_H at 230 K, 250 K, and 270 K are also presented in Fig. 4.15 to compare to three magnetisation curves. It can be seen clearly that three jumps of ρ_H(B) curves occur at the three applied fields B_1, B_2, and B_3 where the spin-flop phenomenon happens. This evidence proves that the critical field B_{crit} observed in ρ_H curve is the spin-flop field B_{sf} (If B_{crit} were the anisotropy field then it would scale as K/M and becomes large close to T_{comp}).

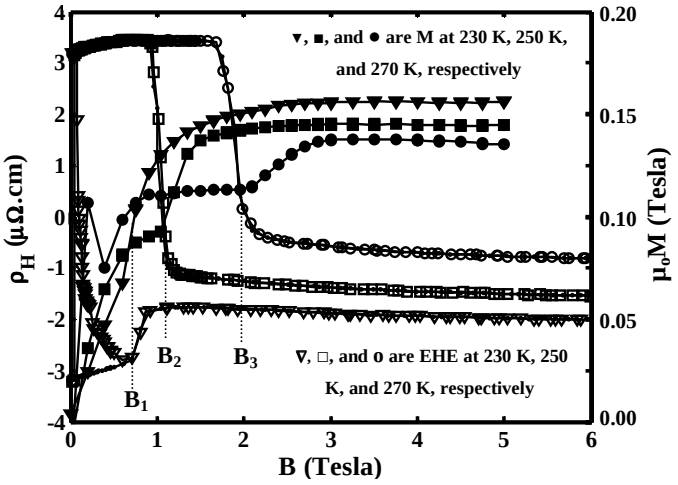

Fig. 4.15. The magnetisation curves (▼, ■, and ●) compared to the EHE curves (∇, □, and o) of sample S1 at temperatures 230 K, 250 K, and 270 K. B is perpendicular to film plane. T_{comp}(EHE) = 235 K while T_{comp}(M) = 225 K. The critical fields are labelled as B_1, B_2, and B_3.

In the cases of small patterned samples as S2, because the EHE measurement area is very small, the magnetisation near T_{comp} cannot be measured by SQUID, so the spin-flop field cannot be specified by means of magnetometry. The extraordinary Hall effect becomes a very effective means to measure the spin-flop field of $Gd_{1-x}Co_x$ thin film in the vicinity of T_{comp}. In all the next sections of thesis, B_{crit} will be abbreviated as the experimental value of B_{sf}.

4.7.2. The magnetisation process of $Gd_{1-x}Co_x$ in calculation

In order to investigate better the spin-flop phenomenon of $Gd_{1-x}Co_x$ alloys, in this section, the magnetisation process of $Gd_{1-x}Co_x$ thin films will be simulated with a Matlab computing program using a numerical method.

In fact, the applied field can be rotated from perpendicular to parallel to the film plane. Furthermore, the easy axis of thin film is not certainly perpendicular to the film plane, it can be tilted from the normal direction of the film. In order to investigate such magnetic configurations in applied field in our simulation, we have to choose a general magnetic configuration of $Gd_{1-x}Co_x$ alloy in applied field as described in Fig. 4.16, where $\vec{z}$ is normal to the film. The easy-axis $\vec{n}$ of $Gd_{1-x}Co_x$ layer is not always parallel to the normal direction $\vec{z}$ but makes an angle δ (δ = 0° for perpendicular easy-axis and δ = 90° for in-plane easy-axis). The external magnetic field $\vec{H}$ is not always perpendicular to the film but makes angle γ with the easy-axis $\vec{n}$. By changing γ and δ, we can consider many magnetic configurations in many magnetisation processes ($\vec{n}$, $\vec{z}$, and $\vec{H}$ are kept in the same plane). Notice that: φ, θ ∈ [0°, 180°], δ ∈ [0°, 90°], and γ ∈ [0°, 90° + δ] where γ and δ are experimental constants.

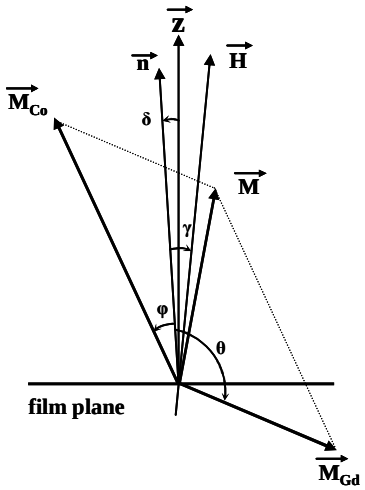

Fig. 4.16. The magnetic configuration of $Gd_{1-x}Co_x$ under an applied field $\vec{H}$. The angles θ, φ, and γ describe the directions of Gd and Co sublattice magnetisations, and the applied field $\vec{H}$ with respect to the easy-axis $\vec{n}$ of the thin film. $\vec{z}$ is the normal direction of the film making an angle δ with the easy-axis $\vec{n}$.

The free energy of $Gd_{1-x}Co_x$ in formula (1.7) can be written again as (K_{Gd} neglected):

$$E = -\mu_o H M_{Co}\cos(\varphi+\gamma) - \mu_o H M_{Gd}\cos(\theta-\gamma) + \mu_o \lambda M_{Co} M_{Gd}\cos(\varphi+\theta) \qquad \textbf{(4.6)}$$
$$+ K_{Co}\sin^2\varphi + \tfrac{1}{2}\mu_o\left(M_{Co}\cos(\varphi+\delta) + M_{Gd}\cos(\theta-\delta)\right)^2$$

The sublattice magnetisations M_{Co} and M_{Gd} will be calculated using our mean-field model. When an external magnetic field is applied, the equilibrium state of magnetism can be found by solving the following equations :

$$\frac{\partial E}{\partial \varphi} = \mu_o H M_{Co}\sin(\varphi+\gamma) - \mu_o \lambda M_{Co} M_{Gd}\sin(\varphi+\theta) + K_{Co}\sin 2\varphi \qquad \textbf{(4.7.a)}$$
$$-\mu_o M_{Co}^2\sin(\varphi+\delta)\cos(\varphi+\delta) - \mu_o M_{Co} M_{Gd}\sin(\varphi+\delta)\cos(\theta-\delta) = 0$$

$$\frac{\partial E}{\partial \theta} = \mu_o H M_{Gd}\sin(\theta-\gamma) - \mu_o \lambda M_{Co} M_{Gd}\sin(\varphi+\theta) \qquad \textbf{(4.7.b)}$$
$$-\mu_o M_{Gd}^2\sin(\theta-\delta)\cos(\theta-\delta) - \mu_o M_{Co} M_{Gd}\cos(\varphi+\delta)\sin(\theta-\delta) = 0$$

Firstly, the spin-flop field can be found by considering the applied field dependence of the angle (φ + θ) between $\overrightarrow{M_{Co}}$ and $\overrightarrow{M_{Gd}}$. So the spin-flop field B_{sf} is the field where the angle (φ + θ) starts decreasing from 180°. Secondly, B_{sf} can be specified by investigating the total magnetisation M, M increases significantly when spin-flop occurs (see Fig. 4.15). Thirdly, B_{sf} can be specified by investigating the applied field dependence of the z-components of Gd and Co sublattice magnetisations M_{Gd}^z and M_{Co}^z (their projections on $\vec{z}$ direction), similar to

M case, sudden changes occur to M_{Gd}^{z} and M_{Co}^{z}.

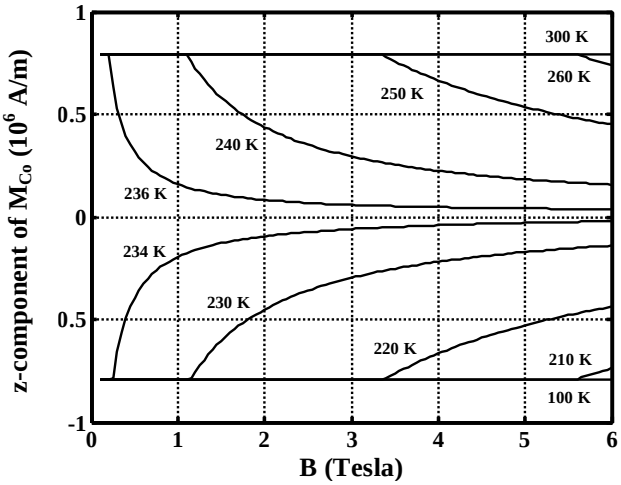

Fig. 4.17. The z-component of Co sublattice magnetisation calculated for sample S1 (T_{comp} = 235 K) with parameters: λ_{CoCo} = 850, λ = 118, x = 0.78, and K_{Co} = 0. The field is perpendicular to the film. The spin-flop field B_{sf} can be evidenced.

In this simulation for sample S1, the sublattice magnetisations M_{Co} and M_{Co} are calculated by the mean-field model using parameters λ_{CoCo} = 850, λ = 118, and x = 0.78. The easy axis of sample is assumed exactly perpendicular to the film (δ = 0). The applied field is perpendicular to film (γ = 0) and varied from 6 T down to 0 T. The angles φ and θ, i.e. the directions of $\overrightarrow{M_{Co}}$ and $\overrightarrow{M_{Gd}}$, are calculated by solving the equations (4.7). The z-component of Co sublattice magnetisation will be calculated as $M_{Co}\cos\varphi$ and presented in Fig. 4.17 for the case of no anisotropy (K_{Co} = 0).

The simulation results show that the z-component of Co magnetisation reverses at T_{comp} (235 K). Furthermore, the spin-flop field where the antiparallel configuration between Gd and Co sublattice magnetisations is broken can be seen obviously as the sudden decrease of the z-component of M_{Co}. By this way, B_{sf} can be calculated in all cases with or without K_{Co} (as mentioned in section 1.3.2, in simple case when K_{Co} is neglected (K_{Co} = 0), the spin-flop field can also be calculated by using formula $B_{sf} = \mu_o \lambda |M_{Co} - M_{Gd}|$). The calculated values of B_{sf} are exposed in Fig. 4.18 for both cases K_{Co} = 0 (solid curve) and $K_{Co} \neq 0$ (dash curve). For K_{Co} = 0, the calculated spin-flop field is zero at T_{comp} whereas the experimental value of spin-flop field (B_{crit}) is 0.7 Tesla at T_{comp}.

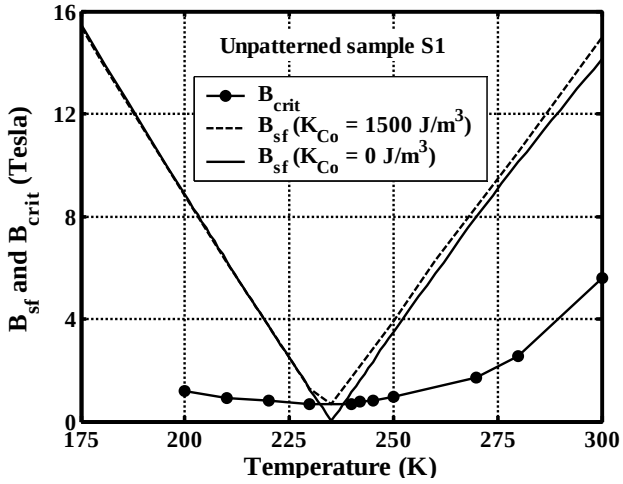

Fig. 4.18. The experimental critical field (B_{crit}) for the unpatterned sample S1 (solid circles) and the spin-flop fields (B_{sf}) calculated for two cases: K_{Co} = 0 (solid curve) and K_{Co} = 1500 J/m^3 (dash curve). The applied field B is perpendicular to the film.

When $K_{Co} \neq 0$ is taken into calculation, B_{sf} still gets minimum at T_{comp} but it is not zero anymore. By turning K_{Co} in the spin-flop simulation, the anisotropy dependence of B_{sf} can be theoretically investigated. When K_{Co} = 1500 J/m^3, the minimum B_{sf} is 0.7 Tesla calculated at T_{comp} (dash curve in Fig. 4.18), right equal to B_{crit}. However, far from T_{comp}, the calculated spin-flop fields B_{sf} are much larger than the experimental B_{crit}. Noticing that, as mentioned in section 4.5.1, the mean-field calculated magnetisation is larger than the real one, so the calculated spin-flop field (B_{sf}) is expected larger than the real one (B_{crit}). Unfotunately, the deviation is too large, e.g. it is about 600% at 200 K (Fig. 4.18), and must originate from other causes such as the composition inhomogeneity.

Since the EHE measurement area of unpatterned sample S1 is about 2×2 mm^2, there must be some compositional variation in this area. Does the large deviation between B_{sf} (calculation) and B_{crit} (experiment) originate from the inhomogeneity of composition? In order to find the answer, the same comparison between calculated B_{sf} and experimental B_{crit} will be carried out for the patterned sample S2a (λ_{CoCo} = 850, λ = 118, and x = 0.79). Because the measurement area of sample S2 is just 50×50 μm^2, much smaller than that of the sample S1, the influence of composition variation must be reduced.

The temperature dependence of the calculated B_{sf} and the experimental B_{crit} of sample S2a are presented in Fig. 4.19. At T_{comp}, it is clear that B_{crit} gets a minimum value of 1.8 Tesla at T_{comp} = 193 K, this value is much larger than 0.7 Tesla in the case of sample S1. By choosing K_{Co} = 9000 J/m^3, we find B_{sf} = 1.8 Tesla at T_{comp}. Away from T_{comp}, the difference between experiment and calculation of B_{sf} is still large but decreased significantly in comparison with the case of unpatterned sample S1. Specifically, in case of sample S1 (T_{comp} = 235 K), at 275 K (40

K away from T_{comp}), the calculation B_{sf} (= 9.5 T) is about 5 times larger than experimental B_{crit} (= 2.5 T). However, in case of patterned sample S2a (T_{comp} = 193 K), at 233 K (40 K away from T_{comp}), the calculation B_{sf} (= 9.5 T) is just about 1.6 times larger than the experimental B_{crit} (= 6.0 T). It is clear that the difference between experiment and calculation decreases a lot in case of patterned sample, i.e. this difference may originate from the compositional inhomogeneity of the film. In the patterned sample, because of the smaller measurement area, the compositional variation decreases, so the agreement between calculation and experiment is improved.

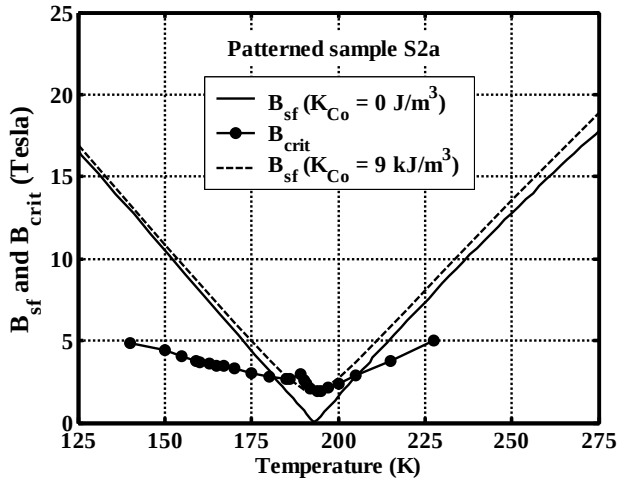

Fig. 4.19. The experimental critical field (B_{crit}) of the patterned sample S2a with T_{comp} = 193 K (solid circles) and the spin-flop fields (B_{sf}) calculated for two cases: K_{Co} = 0 (solid curve) and K_{Co} = 9 kJ/m^3 (dash curve). B is perpendicular to film plane.

According to the previous calculations and experiments on both samples S1 and S2, we can summarise about the spin-flop phenomenon of $Gd_{1-x}Co_x$ thin film that:

- In vicinity of T_{comp}: The spin-flop field B_{sf} is minimum at T_{comp}. B_{sf} is zero at T_{comp} in the case of no anisotropy (K_{Co} = 0). When K_{Co} is taken in to account, B_{sf} is not zero any more. The higher the anisotropy is, the larger the spin-flop field at T_{comp} is. The difference between experimental and calculatied spin-flop fields at T_{comp} can be reduced by choosing a corresponding anisotropy K_{Co}.
- Away from T_{comp}: The addition of K_{Co} to calculation does not make any notable change of B_{sf}. The difference between experiment and calculation increases rapidly at temperatures away from T_{comp}. The comparison between the patterned sample S2 and the unpatterned sample S1 shows the important role of compositional inhomogeneity in the deviation between calculation and experiment of the spin-flop field (the sample could be patterned in smaller dimension to check if the agreement between calculation and experiment is better).

4.7.3. The anomalous temperature range of EHE (ΔT_{rev})

At temperatures above T_{comp}, since Co sublattice magnetisation is larger than Gd sublattice magnetisation, the total magnetisation is expected Co-dominant under any applied fields, even if the spin-flop occurs, so EHE is expected positive as a consequence. Nevertheless, as shown in Fig. 4.14.b, at high fields the EHE can stay negative above T_{comp} = 235 K at several temperatures 238 K, 245 K, 270 K, and 280 K. The temperature dependence of the Hall resistivity under an applied field of 6 Tesla has been measured. The results are presented combined with the saturation ρ_H (before spin-flop) in Fig. 4.20. At 6 Tesla, the EHE is negative at temperatures from 235 K (T_{comp}) to 282 K (47 K above T_{comp}). The width of the anomalous temperature range where the EHE is reversed is ΔT_{rev} = 282 - 235 = 47 K.

In an effort to find the origin of the negative EHE above T_{comp}, many mean-field simulations (x = 0.72 ÷ 0.80, λ = 100 ÷ 200, δ = 0^o ÷ 90^o, K_{Co} = 0 ÷ 100 kJ/m^3) have been carried out for $Gd_{1-x}Co_x$ thin films without composition gradient. The field has been applied in many different directions (γ = 0^o ÷ 90^o) to consider the spin-flop. However, we can not reproduce this behaviour in the homogeneous samples. This makes us suspect that the anomalous behaviour of EHE above T_{comp} originates from the compositional inhomogeneity of $Gd_{1-x}Co_x$ thin films.

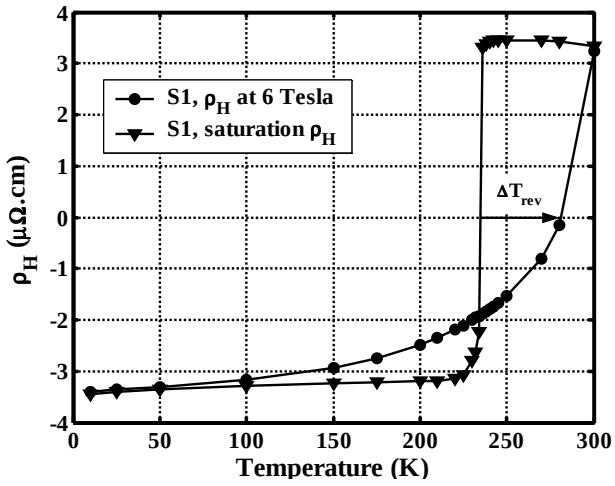

Fig. 4.20. The saturation ρ_H (before spin-flop) and the ρ_H at 6 Tesla for the unpatterned sample S1 (T_{comp} = 235 K). The applied field is perpendicular to the film.

As we saw in Fig. 4.1, there are two EHE measurement locations on the patterned sample S2, namely S2a and S2b with a Hall cross area of 50×50 μm^2. The maximum ρ_H and the ρ_H at 6 Tesla have been measured on both locations S2a and S2b with the applied field perpendicular to film. The experimental results are presented in Fig. 4.21 where the solid and open symbols (triangles are saturation ρ_H and circles are ρ_H at 6 Tesla) are for the sample S2a (T_{comp} = 164 K) and S2b (T_{comp} = 193 K), respectively.

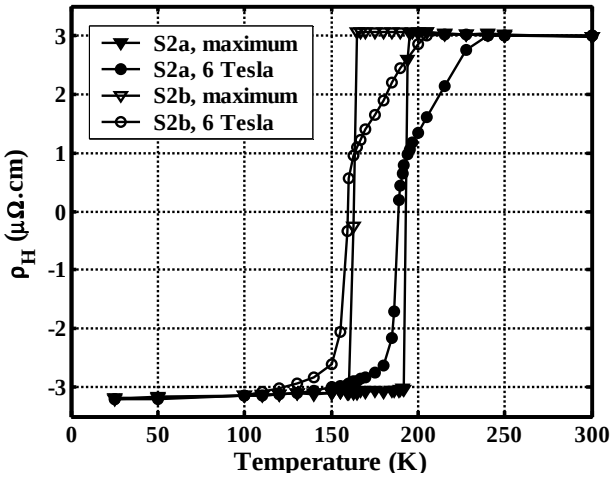

Fig. 4.21. The saturation ρ_H and ρ_H at 6 Tesla of the patterned samples S2a (T_{comp} = 193 K) and S2b (T_{comp} = 164 K). B is perpendicular to film. The measurement area is 50×50 μm^2.

Contrary to the sample S1 where the anomalous temperature range is above T_{comp}, in case of patterned samples S2a and S2b, the ρ_H at 6 Tesla becomes positive at temperature right below T_{comp} where it is expected negative because of a Gd-dominant magnetisation, i.e. the anomalous temperature range is below T_{comp}. Moreover, the width ΔT_{rev} decreases significantly to 5 K, therefore, affirms the influence of composition gradient on the appearance of the anomalous temperature range of EHE.

The composition gradient of sample S2 can be estimated according to the T_{comp} differences of the two EHE measurement areas S2a and S2b. According to Fig. 4.1, the distance between S2a and S2b is about 2mm. The difference of T_{comp} is ΔT_{comp} = 193 K - 164 K = 29 K. Comparing to the composition dependence of T_{comp}, 40 K/% (see Fig. 3.7), we find a composition gradient of 0.38 %/mm in the direction of S2a-S2b on sample S2.

4.7.4. The coercive field

The coercive fields of patterned sample S2a (T_{comp} = 193 K) and S2b (T_{comp} = 164 K) taken from EHE loops are shown in Fig. 4.22. Before spin-flop, magnetisation reversal is mainly controlled by domain wall propagation. Supposing one single type of pinning center, a crude model can be proposed where the Zeeman energy is equal to the pinning energy at the coercive field ($E_{Zeem} = E_p$ at $H = H_C$). We find $\mu_o M H_C = E_P$ where E_P is the pinning energy. The pinning energy has been fitted to get a good agreement between experiment and calculation. The coercive fields are calculated by using $\mu_o H_C = E_P/M$ with E_P = 1500 J/m^3 and the total magnetisation M is calculated by mean-field model for both samples S2a (λ_{CoCo} = 850, λ = 118, and x = 0.79) and S2b (λ_{CoCo} = 850, λ = 118, and x = 0.80). The calculated results are presented in Fig. 4.22 combined with the experimental results.

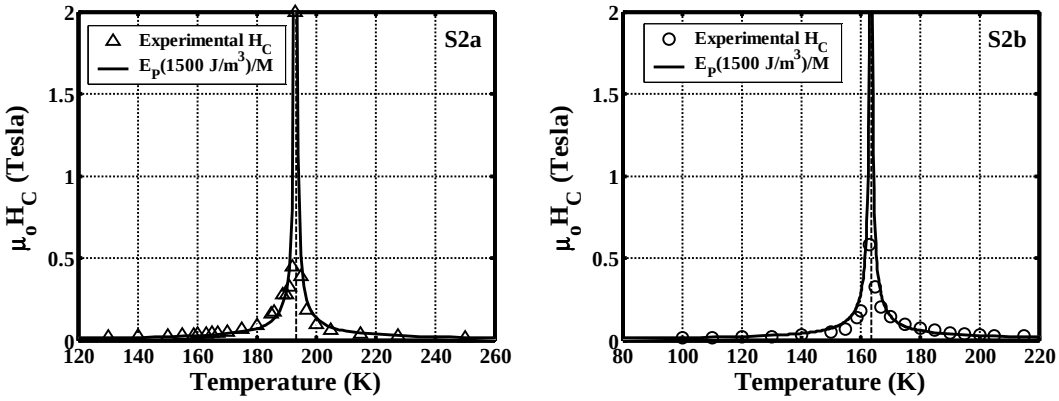

Fig. 4.22. The coercive field of sample S2a (T_{comp} = 193 K) and S2b (T_{comp} = 193 K) measured using EHE loops (open triangles and open circles) and calculated using formula $\mu_o H_C = E_P/M$ with E_P = 1500 J/m^3 (solid curves).

We can see that the calculated coercive fields are always symmetric though the line T = T_{comp} while the experimental values of H_C are not symmetric for both samples. However, in the case of S2a the low-temperature part ($T < T_{comp}$) of experimental $\mu_o H_C$ is higher than the high-temperature part ($T > T_{comp}$), in contrary to the case of S2b where the low-temperature part is lower. This difference implies that the asymmetries around $T = T_{comp}$ of the coercive field in the cases of samples S2a and S2b are not systematic. Again, they may originate from the compositional inhomogeneity of sample.

4.8. Conclusion about EHE and magnetic properties of $Gd_{1-x}Co_x$ thin films

The EHE of amorphous $Gd_{1-x}Co_x$ thin films has been studied theoretically and experimentally in detail following the variation of temperature as well as magnetic field. The mean-field theory has been applied to calculate the temperature dependences of the Gd and Co sublattice magnetisations. By comparing the temperature dependences of the calculated values of M_{Gd} and M_{Co} to the temperature dependence of the experimental values of ρ_H, the study has estimated the contributions of Co and Gd moments to the EHE. The Co moments give a positive contribution ($R_{Co} > 0$) while the Gd moments give a negative one ($R_{Gd} < 0$) to EHE. In the amplitude of ρ_H, a dominant role of Co moments has been determined, the contribution of Co moments (near 90%) is much larger than the contribution of Gd moments (about 10%) to Hall resistivity.

The magnetic properties of amorphous $Gd_{1-x}Co_x$ alloys have been investigated by means of the extraordinary Hall effect under a high applied field up to 6 Tesla. The in-plane-applied-field EHE results have revealed the perpendicular multidomain structure of $Gd_{1-x}Co_x$ thim films at low temperatures. Near the compensation temperature, the spin-flop phenomenon has been clearly observed. The experimental results proved that the spin-flop field B_{sf} is not zero at T_{comp}. A mean-field simulation has been applied to investigate the impact of anisotropy (K_{Co}) on B_{sf},

the calculated results prove that when K_{Co} is taken into calculation, although B_{sf} always get minimum at T_{comp}, this minimum B_{sf} strongly depends on K_{Co}. The larger the anisotropy K_{Co} is, the larger the minimum B_{sf} is.

In spite of the deviation between the calculated results and the experimental results of B_{sf} , which is still large, the comparison between the unpatterned sample S1 and the patterned sample S2 reveals an important impact of the compositional inhomogeneity on the deviation between calculation and experiment. However, the reason of this deviation is still unclear and open for future studies. If it is possible in the future to get a more quantitative agreement between EHE above spin-flop measurement and calculation, a more precise determination of Gd and Co roles is possible.

Chapter. 5. Magnetoresistance in magnetic multilayers

5.1. Introduction

For quite a long time the spin of electrons was not considered when designing an electrical transport device. This can be understood since in non-magnetic conductors, the properties of electrons do not depend on spin. This, however, is no longer valid when considering ferromagnetic conducting materials [89]. Using the spin as an extra parameter or degree of freedom widens the field of electronics and is called spin electronics or spintronics. This is a fast developing field, which was created at the end of the 1980's when Giant Magnetoresistance was discovered and has already given fruitful applications in the field of sensing. Magnetoresistive sensors have rapidly overcome inductive sensors in the field of high-density recording (hard disk heads), and prototypes have appeared in the field of data storage: magnetic-RAM (MRAM) [96].

In this chapter, firstly some general electrical transport properties of magnetic conductors related to the spin of electrons will be introduced. The mechanism of giant magnetoresistance (GMR) will be described in detail including the sign (positive or negative) of the MR ratio.

5.2. The theoretical concepts of electrical transport in magnetic conductors

5.2.1. Spin polarisation

In a magnetic conductor, the electrons, which participate to the conduction of the electrical current, are most often s, d and hybridised sd electrons. Two families of these electrons can be distinguished according to the projection of their spin along the local magnetisation axis: the spin ↑ electrons (respectively the spin ↓ electrons) conventionally have the z-component of their spin parallel (respectively antiparallel) to the local magnetisation. In this description, the z-axis is chosen as the quantisation axis and is parallel to the local magnetisation. Different from the case of normal conductors where the densities of spin ↑ and spin ↓ conduction electrons are the same (Fig. 5.1.a), in magnetic metallic conductors, because of the interaction between free conduction electrons and the localised magnetic electrons (3d, 4f), there is an asymmetry between spin ↑ and spin ↓ electrons in the conduction band (Fig. 5.1.b). Because the densities of state of spin ↑ and spin ↓ electrons at Fermi level are different, it allows for a new parameter called spin polarisation.

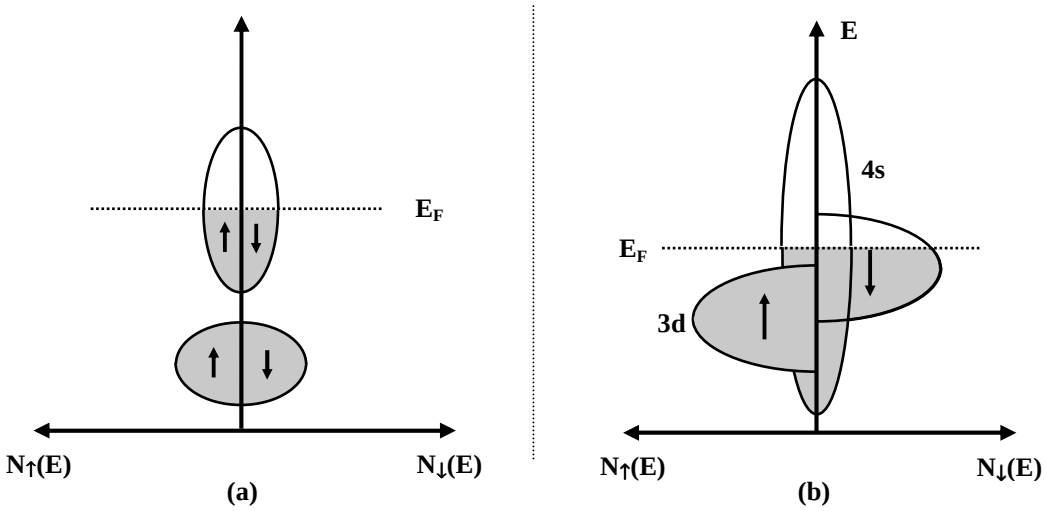

Fig. 5.1. Band structure of a normal metal (a) and a strong ferromagnetic metal (b).

The spin polarisation of electronic states P_N is usually defined as

$$P_N = (N_\uparrow - N_\downarrow)/(N_\uparrow + N_\downarrow) \quad \textbf{(5.1)}$$

Where $N_\uparrow$ and $N_\downarrow$ are the total density of electronic states (DOS), including s and d electrons, at Fermi level for spin ↑ and spin ↓, respectively. In experiments, P_N (DOS spin polarisation) can be determined using spin-polarised photoemission [103].

Noticing that while P_N is only defined by the density of electronic states (DOS) at Fermi level, the transport phenomena are not defined by the DOS alone. This is particularly true for materials which have both heavy d-electrons (more localised) and light s-electrons (more delocalised) at the Fermi level (e.g., transition metals). While the DOS is mostly defined by the former, the electric transport is primarily due to the more mobile s electrons [103].

In experiments, there are several techniques to measure the spin polarisation of conduction electrons P (transport spin polarisation), i.e. the spin-polarised tunneling in various forms [104] including Andreev reflection [105]. However, because the transport spin polarisation P measured in those experiments is mainly contributed by the conduction electrons, P and P_N are different and possibly have opposite signs. Experiments show that traditional transition metals and alloys have positive spin polarisations P of the order of 20% to 50% (Table. 5-1).

Table. 5-1: Typical spin polarisations of ferromagnetic metals (ref. [89]).

Metallic materials	Ni	Co	Fe	$Ni_{80}Fe_{20}$	$Co_{50}Fe_{50}$
P (%)	20 ÷ 30	35 ÷ 45	40 ÷ 44	32 ÷ 48	50

Since magnetoresistive effects are directly related to the spin polarisation (P, P_N), search for higher polarisation is a long-term trend. Experimentally, spin polarisations in excess of 80% have been measured at low temperatures but 3d metals and alloys (shuch as CoFe) are still the best spin-polarised materials at room temperature.

5.2.2. Spin-flip

Spin-flip scattering allows both carrier populations (spin ↑ and spin ↓) to interact. It is a rare event compared to non spin-flip scatterings so both populations are well defined and a two-fluid picture is quite commonly used especially at low temperature. Non-balanced spin populations can be induced by polarised light absorption or when an electrical current passes through an interface between two materials with different spin polarisations. Equilibrium of both populations is restored by the relevant spin-flip scattering mechanisms.

Table. 5-2: Characteristic spin diffusion lengths (ref. [89]).

Metallic materials	Cu	$Ni_{80}Fe_{20}$	Co
Spin diffusion length	140 nm (300 K)	4 nm (4 K)	59 nm (77 K) and 38 nm (300K)

The spin-flip characteristic time is τ_{sf}. The length scale to restore spin equilibrium is the spin diffusion length $l_{sf} = \sqrt{v_F \tau_{sf} \lambda / 3}$ where v_F is the Fermi velocity and λ is the mean free path. In cases of ferromagnetic conductors, the spin diffusion length is significantly decreased (see Table. 5-2).

5.2.3. Spin dependent scattering asymmetric coefficient (β)

In ferromagnetic transition metals and R-T intermetallic compounds (e.g. GdCo), the spin ↑ and spin ↓ electrons have different scattering rates (see [98]-[101]) depending on the nature of the scattering centers (for example magnetic impurities; structural defects such as dislocations, stacking faults or grain boundaries; or even phonons). The spin-dependence of the scattering rates results from the difference of the density of available states at the Fermi energy into which the electrons can be scattered. The difference in the spin ↑ and spin ↓ density of states is itself a consequence of the d-band exchange splitting, characteristic of the magnetism of transition metals, as described by the well-known Stoner model [102]. For example, in Permalloy ($Ni_{81}Fe_{19}$), the mean-free path of spin ↑ electrons has been estimated to be at least 5 times longer than that of spin ↓ electrons [98].

When the spin-orbit coupling and the magnon scattering are negligible (as in transition metal and R-T intermetallic compounds at low temperatures), the spin-flip does not happen, these two species (spin ↑ and spin ↓) of electrons can be considered as carrying electrical

current in parallel, all other scattering events are unable to perturb the spin state of the electrons [97]. Since a two fluid picture is relevant, one introduces the spin dependent scattering asymmetric coefficient (it is also called the asymmetric coefficient) as:

$$\beta = (\rho_{\uparrow} - \rho_{\downarrow})/(\rho_{\uparrow} + \rho_{\downarrow}) \qquad \textbf{(5.2)}$$

where the resistivities of the spin ↑ and spin ↓ channels are $\rho_{\uparrow}$ and $\rho_{\downarrow}$, respectively.

The asymmetric coefficient β directly relates to both spin polarisations P_N (DOS) and P (transport) and depends on materials. For example, $\beta < 0$ for most transition metals because s↓-d↓ scattering is stronger. For Co, the fraction $\rho_{\downarrow}/\rho_{\uparrow}$ is 2 to 3 (β is from -0.3 to -0.5), for FeNi this ratio increases up to 9 (β is about -0.8) [89].

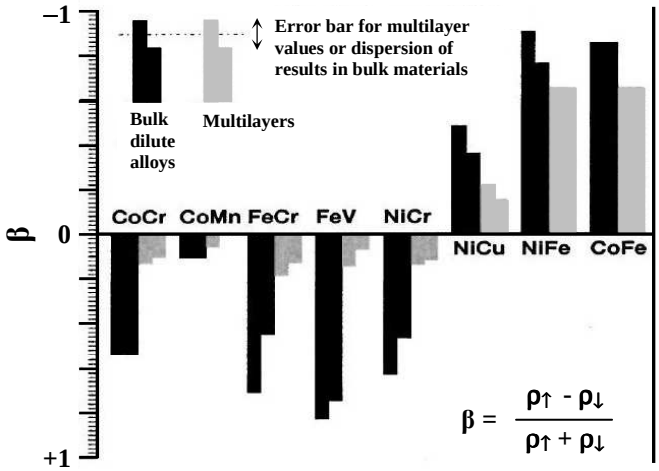

Fig. 5.2. The spin dependent scattering asymmetric coefficients (β) for several dilute alloys imported from ref. [106].

Fig. 5.2 shows the experimental values of spin dependent scattering asymmetric coefficients (β) for several alloys derived from the analysis of GMR in multilayers (measured in current-perpendicular-to-plane configuration) and found in bulk [106]. In the alloys of CoCr, CoMn, FeCr, FeV, and NiCr, β is positive while it is negative in the alloys of NiCu, NiFe, and CoFe.

5.2.4. Interface spin dependent scattering in nanostructures

In nanostructures, e.g. in multilayers, interfaces between materials with different spin polarisations, i.e. different β, can be treated as spin dependent interfacial resistances. This interfacial resistivity is of the order of 10^{-15} Ω.m^2. Its value changes by a factor 5 depending on spin ↑ or spin ↓ in the case of FeNi/Cu interface for example [89]. The asymmetric coefficient β in the interface (the definition of the interfacial β is the same as the formula (5.2) but $\rho_{\uparrow}$ and $\rho_{\downarrow}$ are the interfacial resistivities) and in the bulk can be different in amplitude and sometimes in

sign. For instance, in the case of $\{Fe_{0.70}Cr_{0.30}$ (t nm)/Cu (2.3 nm)/Co (0.4 nm)/ Cu (2.3 nm)$\}_n$ multilayer, $\beta > 0$ in the bulk of a FeCr layer and $\beta = 0$ in Cu layers, however, β is negative at FeCr/Cu interface [109]. For the whole FeCr layer, there is a competition between the FeCr layer core (bulk) scatterings and the FeCr/Cu interface scatterings, so the global asymmetric coefficient β of the FeCr layer (including interface and core) depends on the thickness t of FeCr layer. There is a compensation thickness $t^* = 2$ nm of FeCr layer where the interface scattering is compensated by the core (bulk) one. When $t > t^*$, the global β of FeCr layer is positive, and it is negative if $t < t^*$ (see Fig. 2 in ref. [109]).

According to literature, for the interfaces of ferromagnetic (Fe, Co, and Ni)/noble metals (Au, Ag, and Cu), the asymmetric coefficient β is negative ($\beta < 0$) [106], which might relate to the modification of the DOS of the ferromagnetic surface atomic layer by the noble spacer [117].

5.3. Magnetoresistance

Magnetoresistive (MR) effect is the phenomenon in which the resistivity of a conductor changes under the effect of external magnetic field. The magnetoresistance ratio is usually defined as $(R_0-R_H)/R_0$ where R_0 and R_H are the resistances in zero field and in an applied field $\overrightarrow{\mu_o H}$, respectively. Some MR effects are volume effect (cyclotron and anisotropic magnetoresistances) and have been known for a long time. Since the fabrication of nanostructured materials is technically controlled, especially in multilayer form, new effects related to spin transport through interfaces have been discovered (giant magnetoresistance and tunnel magnetoresistance, spin injection and spin torque effects).

5.3.1. Cyclotron magnetoresistance or Ordinary magnetoresistance (OMR)

In any conductor, an applied magnetic field will disturb the electron trajectories, and longitudinal and transverse cyclotron magnetoresistances can be defined. The effect is small and it corresponds to the increase of resistance under the field. It is generally proportional to the square of the field. Most metals follow Kohler's law i.e. $\Delta\rho/\rho = f(B/\rho)$, with f being a material-dependent function which is close to a quadratic law. The lower the temperature is (smaller ρ) and the higher the field is, the higher is the cyclotron MR is. The order of magnitude of the effect is about 0.1% in a 1 Tesla field. The cyclotron magnetoresistance is also called the ordinary magnetoresistance and abbreviated to OMR.

5.3.2. Anisotropic magnetoresistance (AMR)

AMR is also a volume effect. In ferromagnetic metals, s and d electrons are present in the conduction band. If the asymmetry of the d band is large, s-d scattering depends on the

configuration between the magnetisation $\vec{M}$ (in saturation state, it is parallel to the applied field $\overrightarrow{\mu_o H}$) and the carrier wave-vector $\vec{k}$ (it is parallel to the applied current $\vec{J}$). Two resistivities can be defined: $\rho_{//}$ where the current $\vec{J}$ and the applied field $\vec{B}$ are parallel, and $\rho_{\perp}$ where $\vec{J}$ and $\vec{B}$ are perpendicular (Fig. 5.3).

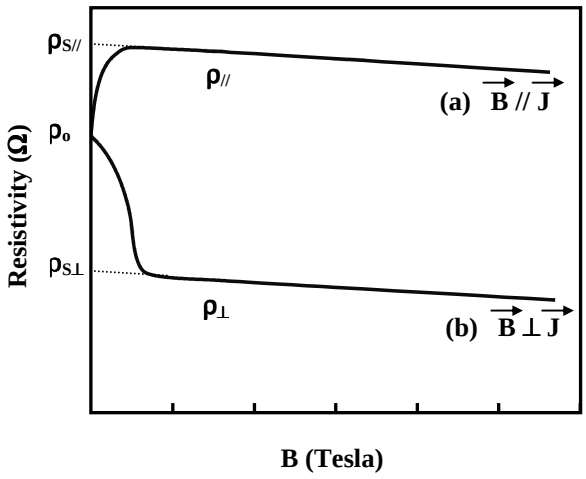

Fig. 5.3. The characteristic resistivity curves of a ferromagnetic conductor measured in the in-plane applied fields $\vec{B}$ parallel (a) and perpendicular (b) to the applied current $\vec{J}$ [95].

The angular dependence of AMR can be written as:

$$\rho = \rho_{\perp} + (\rho_{//} - \rho_{\perp})\cos^2(\vec{J}, \vec{M}) \qquad \textbf{(5.3)}$$

AMR can reach a few percents in Ni and its alloys (in $Ni_{80}Fe_{20}$, AMR is 2% at room temperature, and 20% at low temperature). ($\rho_{//} - \rho_{\perp}$) is positive for transition metal systems. This kind of MR has been the first one to be used in sensors [96].

5.3.3. Giant magnetoresistance (GMR): The invention of GMR

GMR effect was discovered in 1988 by Baibich et al [90] in a series of (001)Fe/(001)Cr magnetic superlattices prepared by molecular beam epitaxy (Fig. 5.4). The Fe layer thickness was fixed at 30 Å. The thickness of Cr layer was increased from 9 Å to 30 Å. A huge magnetoresistance was found in the superlattice multilayers with Cr thickness of 9 Å, 12 Å, and 18 Å. A maximum MR ratio as high as 45% (at 4.2 K) was obtained with a Cr thickness of 9 Å. The magnetism studies showed that there is an antiparallel coupling of the neighbouring Fe layers at zero field when the resistance of multilayers is maximum. Above saturation field ($H > H_S$), all Fe layers are parallel and the resistance is minimum. The MR here strongly depends on the angle between the magnetisations of two Fe successive layers and has been named giant magnetoresistance (GMR). The GMR is different from the OMR and the AMR not only in amplitude but also in mechanism.

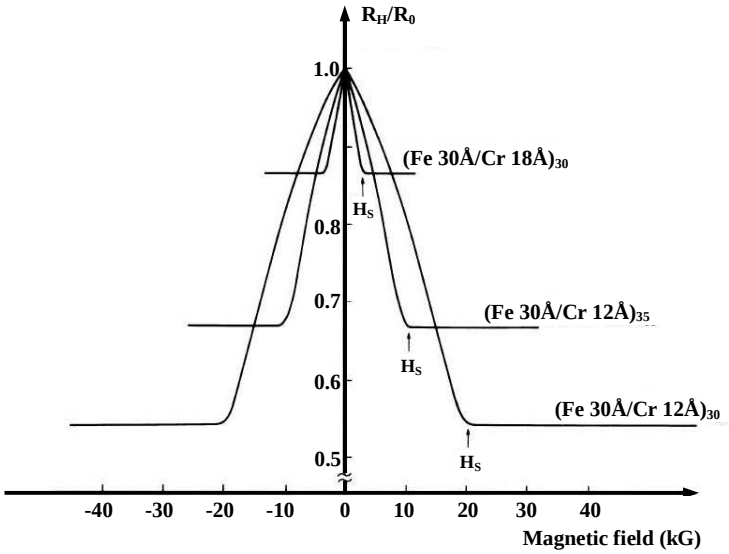

Fig. 5.4. Magnetoresistance of three Fe/Cr superlattices at 4.5 K. The current and the applied field are along the same [110] axis in the plane of the layers (Baibich et al in ref. [90]).

The basic requirements of a GMR junction are two ferromagnetic layers which are magnetically decoupled in order to be able to obtain parallel and antiparallel magnetisation configurations. The MR effect will be observed when comparing the resistance of both configurations. In order to decouple both ferromagnetic electrodes (M_1 and M_2), one needs a non-magnetic metal spacer (NM) (see Fig. 5.5) then the GMR effect may be observed.

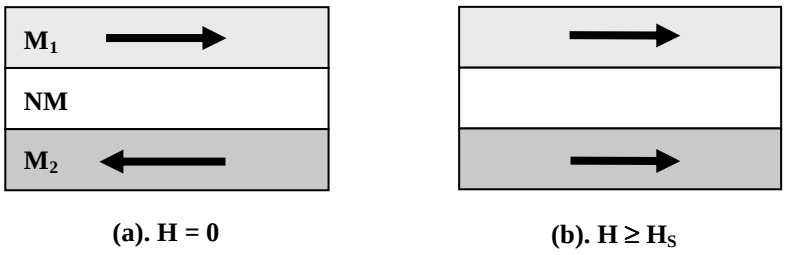

Fig. 5.5. The configuration of a basic GMR junction with two magnetic layers (M_1 and M_2) decoupled by a non-magnetic layer (NM). The magnetic configuration can be parallel (a) or antiparallel (b) depending on the applied field $\mu_o H$.

Two electrical configurations exist. If the current is in the plane of the trilayer, we have the CIP (current-in-plane) GMR. If the current passes perpendicular to the interfaces it is the CPP-GMR (current-perpendicular-to-plane). In CIP the relevant lengthscale for the spacer thickness is the electron mean free path. Electrons should visit both ferromagnetic electrodes. The typical thickness of the spacer is a few nm. In CPP geometry, the spacer thickness can be larger (but small compared to the spin diffusion length in the spacer which can be as large as 100 nm). All the measurements performed in this thesis are CIP measurements .

5.4. The spacer-layer thickness dependence of GMR ratio

Different from AMR, GMR does not depend on the angle between the applied field and the applied current, but depends on the angle between neighbouring magnetic layer magnetisations. As one knows, a basic requirement of GMR junction is the rotation from the antiparallel configuration to the parallel configuration of both magnetic layers ($\overrightarrow{M_1}$ and $\overrightarrow{M_2}$). During the rotation, the dependence of the resistance on the angle φ between both magnetic moments can be written as [96]:

$$R = R_{\uparrow\uparrow} + \Delta R \frac{(1-\cos\varphi)}{2} \qquad \textbf{(5.4)}$$

Where $\Delta R = R_{\uparrow\downarrow} - R_{\uparrow\uparrow}$, and $R_{\uparrow\downarrow}$ and $R_{\uparrow\uparrow}$ are the resistances for antiparallel ($\varphi = \pi$) and parallel ($\varphi = 0$) configurations of both magnetic layers.

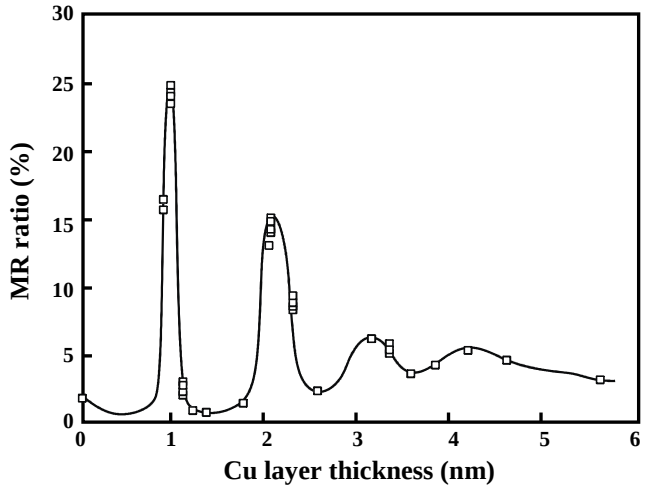

Fig. 5.6. The dependence of MR ratios on the Cu layer thickness in the NiFeCo/Cu/Co/Cu multilayers [94].

Not long after the invention of GMR effect ([90]-[91]), Parkin et al (1990) have studied the dependence of GMR ratio defined as $(R_{\uparrow\downarrow} - R_{\uparrow\uparrow})/R_{\uparrow\downarrow}$ on the thickness of the nonmagnetic layer (spacer-layer) in series of multilayers: $\{Co/Ru\}_n$, $\{Co/Cr\}_n$, and $\{Fe/Cr\}_n$ multilayers in ref. [92], and $\{Co/Cu\}_n$ multilayer in ref. [93]. The GMR ratio is found to oscillate with the thickness of nonmagnetic spacer layer (Ru and Cr), and a much larger MR ratio (115%) was obtained in Co/Cu multilayer at 4.2 K with application of 1.5 Tesla. Fig. 5.6 shows the dependence of MR ratios on the Cu layer thickness in $\{Ni_{80}Fe_{15}Co_5$ (3 nm)/Cu (t)/Co (3 nm)/Cu (t)$\}$ multilayers prepared by sputtering [94]. The MR ratio is maximum at around t = 0.9 nm, 2.0 nm, and 4.2 nm with a period of 1.1 nm.

Furthermore, the antiferromagnetic interlayer exchange coupling was also studied for such the series of multilayers and has been found to oscillate with the thickness of spacer-layer.

The oscillatory dependence of magnetoresistance and exchange coupling on the spacer-layer thickness in many different metallic multilayers have been related to RKKY coupling, which is an indirect coupling using the spacer-layer conduction electrons. The MR ratios usually get maximum when the antiferromagnetic coupling becomes dominant [96]. When RKKY is absent (thicker spacer), a way to stabilise the antiferromagnetic configuration has to be implemented (different coercive fields or pinning of the harder layer).

5.5. Mechanism of giant magnetoresistance

5.5.1. The spin-dependent scattering mechanism

The GMR effect is attributed to a competition of interfacial and bulk spin-dependent scatterings, both of which are accumulated in the global spin dependent scattering asymmetric coefficient β, i.e. the global coefficient β is due not only to the magnetic layer cores (bulk) but also to the interfaces between magnetic and nonmagnetic layers.

In a basic GMR junction including two magnetic layers (M_1 and M_2) decoupled by a non magnetic metallic layer (NM), GMR is positive or negative depending on the global asymmetric coefficient β_1 and β_2 of both magnetic layers (see ref. [106] and [109]). A positive GMR will be induced if $\beta_1\beta_2 > 0$. In opposite, a negative GMR can be induced if $\beta_1\beta_2 < 0$.

In the next discussions, the two kinds (positive and negative) of GMR junctions will be described in more detail with an assumption that no spin-flip occurs in the sample, i.e. the spin of conduction electrons are conservated. Because the spin $\uparrow$ or spin $\downarrow$ electrons are defined by the relative orientation of the z-component of electron spin with respect to the magnetisation (see section 5.2.1), the spin ($\uparrow$ or $\downarrow$) of a spin-conservated electron can be reversed thanks to the reversal of magnetisation axis.

a. The positive GMR (normal GMR)

Let's start interpreting the mechanism of GMR effect in the case that the spin dependent scattering asymmetric coefficients of both magnetic layer are negative ($\beta_{1,2} < 0$). It means that, in both magnetic layers, the spin $\downarrow$ electrons are more scattered than spin $\uparrow$ electrons, i.e. the resistivity of spin $\uparrow$ channel is smaller than that of spin $\downarrow$ channel ($\rho_\downarrow > \rho_\uparrow$). The two magnetic layers are decoupled by a non-magnetic layer with a thickness smaller than the mean-free path of conduction electrons to get a good GMR ratio. The relative orientation of magnetisations in both magnetic layers can somehow be changed from antiparallel to parallel.

The spin-dependent scattering mechanism, in this case ($\beta_{1,2} < 0$), is described in Fig. 5.7. When the magnetic configuration of GMR junction is parallel (P configuration), the spin $\uparrow$ electrons in magnetic layer M_1 are still spin $\uparrow$ electrons in layer M_2 (because $\overrightarrow{M_1}$ and $\overrightarrow{M_2}$ are

parallel). It is clear that the spin ↑ electrons are less scattered while the spin ↓ electrons are strongly scattered in both magnetic layers. The shorting of the spin ↓ channel current by the ↑ channel makes the resistance low in parallel configuration (Fig. 5.7.a). Neglecting the resistance of the non-magnetic layer, the resistance of the GMR junction in configuration parallel (P) can be found as: $R_P = (r_1 + r_2)(R_1 + R_2)/(r_1 + R_2 + r_2 + R_1)$ where $r_{1,2}$ and $R_{1,2}$ are the resistances of two spin channels in the two magnetic layers.

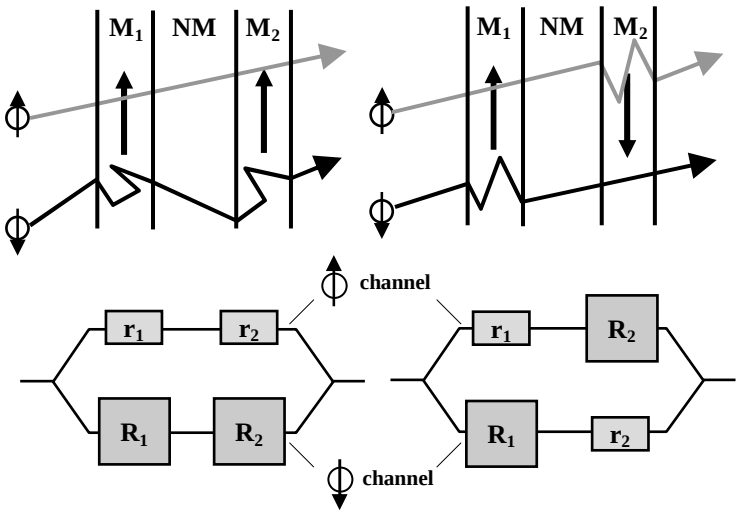

(a). Configuration Parallel **(b). Configuration Antiparallel**

Fig. 5.7. Schematic picture of the GMR mechanism for the case $\beta_{1,2} < 0$ in both magnetic layers. $r_{1,2}$ and $R_{1,2}$ denote the resistances of two spin chanels in the two magnetic layers ($R_1 > r_1$, $R_2 > r_2$). The electron trajectories between two scatterings are represented by straight lines and the scattering by an abrupt changes in the direction. The arrows represent the magnetisation direction of each magnetic layer.

When the magnetisations of both magnetic layers are antiparallel, the spin ↑ in layer M_1 will be spin ↓ in layer M_2, and the spin ↓ in layer M_1 will be spin ↑ in layer M_2. The resistance is averaged in each channel (Fig. 5.7.b). The resistance in configuration antiparallel (AP) is: $R_P = (r_1 + R_2)(R_1 + r_2)/(r_1 + R_2 + r_2 + R_1)$.

By using $R_1 > r_1$ and $R_2 > r_2$, it can be shown that $R_P < R_{AP}$. So the GMR ratio $(R_{AP}-R_P)/R_{AP}$ in this case is positive, it is normal GMR. The characteristic applied field dependence of a positive GMR is presented in Fig. 5.8. The same explanation can be applied for the case when the spin polarisations of both magnetic layers are positive ($\beta_{1,2} > 0$). We just need to swap the positions of spin ↑ and spin ↓ electrons in Fig. 5.7, and then we find again a positive GMR. In summary, when $\beta_1\beta_2 > 0$, the GMR ratio is positive, so it is the normal GMR.

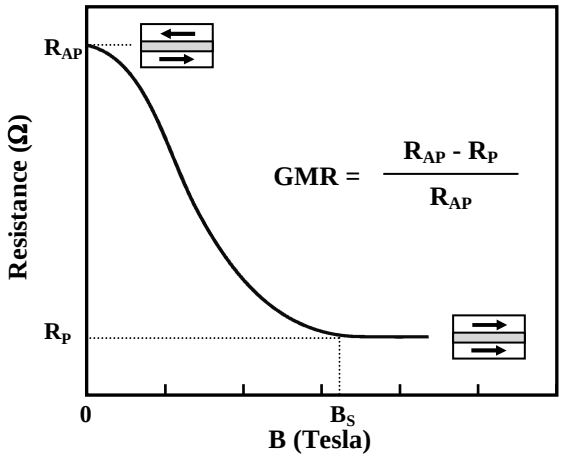

Fig. 5.8. Characteristic curve of a positive GMR where the resistance in antiparallel configuration is larger than that in parallel configuration ($R_P < R_{AP}$).

b. The negative GMR (inverse GMR)

Let us consider the cases of GMR junctions where the asymmetric coefficients of the two magnetic electrodes are opposite in sign, i.e. the term $\beta_1\beta_2$ is negative. The mechanism of spin dependent scattering in the case $\beta_1 < 0$ and $\beta_2 > 0$ is sketched in Fig. 5.9. Please notice that, in this case, the spin $\uparrow$ electrons are less scattered in layer M_1 and more scattered in layer M_2, and the spin $\downarrow$ electrons are more scattered in layer M_1 and less scattered in layer M_2.

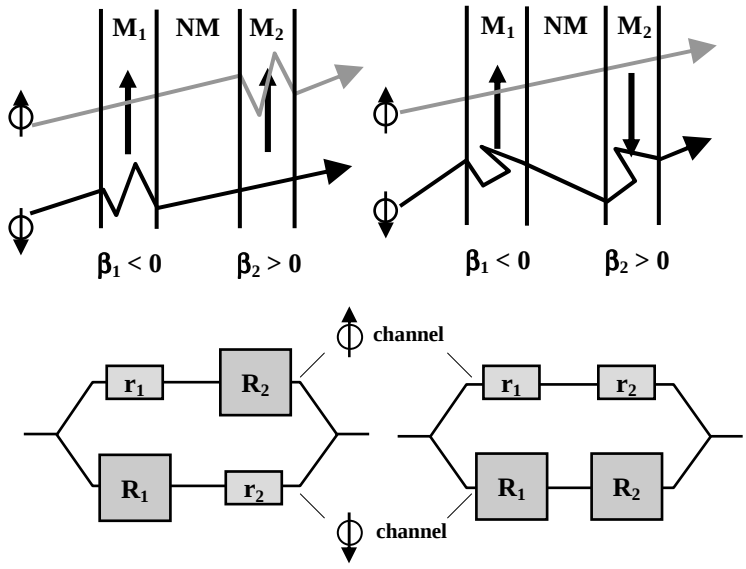

(a). Configuration Parallel (b). Configuration Antiparallel

Fig. 5.9. Schematic picture of the GMR mechanism for the case $\beta_1 < 0$ and $\beta_2 > 0$. $r_{1,2}$ and $R_{1,2}$ denote the resistances of two spin chanels in the two magnetic layers ($R_1 > r_1$, $R_2 > r_2$). The electron trajectories between two scatterings are represented by straight lines and the scatterings by abrupt change in the direction. The arrows represent the magnetisation direction of each magnetic layer.

In configuration parallel (Fig. 5.9.a), the spin ↑ (and spin ↓) electrons in one magnetic electrode are still spin ↑ (and spin ↓) electrons in the other electrode. By using the same calculation as before, we can find in configuration parallel, the resistance of junction is $R_P = (r_1 + R_2)(r_2 + R_1)/(r_1 + R_2 + r_2 + R_1)$. The shorting of one spin channel current just occurs in configuration antiparallel, because the spin ↑ electrons in layer M_1 (low resistance r_1) becomes spin ↓ electrons (low resistance r_2) in layer M_2, so the resistance of the junction in configuration antiparallel is low (Fig. 5.9.b) and can be calculated as $R_{AP} = (r_1 + r_2)(R_2 + R_1)/(r_1 + R_2 + r_2 + R_1)$. Because $(R_1 - r_1) > 0$ and $(R_2 - r_2) > 0$, it can be inferred that $R_P > R_{AP}$. So the GMR ratio $(R_{AP}-R_P)/R_{AP}$ in this case of GMR junction ($\beta_1 < 0$ and $\beta_2 > 0$) is negative, opposite to the case of normal GMR, therefore it is called inverse GMR.

In the last case when $\beta_1 > 0$ and $\beta_2 < 0$, using the same discussion, we just need to swap the positions of spin ↑ and spin ↓ channels in Fig. 5.9, an inverse GMR will be found again. In summary, when two magnetic electrodes in GMR junction have opposite spin asymmetric coefficients, i.e. $\beta_1\beta_2 < 0$, a negative GMR can be induced.

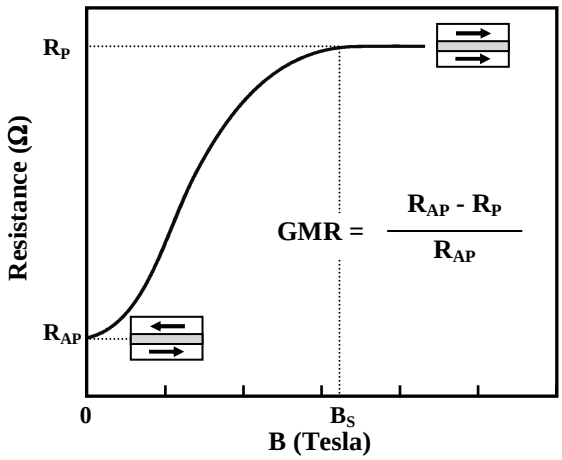

Fig. 5.10. Characteristic curve of a negative GMR where the resistance in antiparallel configuration is smaller than that in parallel configuration ($R_P > R_{AP}$).

The characteristic applied field dependence of a negative GMR (inverse GMR) is presented in Fig. 5.10 where the resistance in configuration antiparallel is smaller than the resistance in configuration parallel.

5.6. GMR junctions based on $Gd_{1-x}Co_x$ ferrimagnet: State of the art

5.6.1. The sign of GMR and the spin asymmetric coefficient of $Gd_{1-x}Co_x$ alloys

Although almost all GMR effects in the literature are positive GMR (normal GMR) including the original paper [90], the negative GMR (inverse GMR) has been observed in many multilayers (see refs. [106]-[115]).

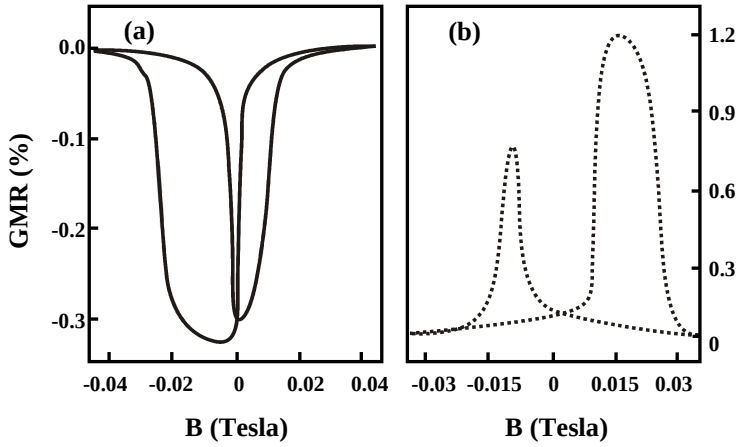

Fig. 5.11. GMR curves at room temperature of two spin-valves: (a) {Fe (2nm, β < 0)/Cu (3 nm)/$Gd_{0.38}Co_{0.62}$ (4.2 nm, β > 0)} and (b) {Fe (2nm, β < 0)/Cu (3 nm)/$Gd_{0.23}Co_{0.77}$ (4.2 nm, β < 0)} (see ref. [116]).

Very recently, Yang et al (2006) [116] have studied GMR of {Fe (2nm)/Cu (3 nm)/$Gd_{1-x}Co_x$ (t_{GdCo} nm)} spin valves (This study was being carried out at the same time as our study on GMR of NiFe\Cu\GdCo multilayers, the results of our study will be presented in chapter 7). These GMR junctions are interesting because the global asymmetric coefficient β of the Fe layer is negative [109], and the global β of $Gd_{1-x}Co_x$ layer can be changed in amplitude and sign by changing the composition of $Gd_{1-x}Co_x$ alloys (see Fig. 5.11) and/or the $Gd_{1-x}Co_x$ layer thickness (see Fig. 5.12). GMR of these spin valves can be positive or negative depending on the the global β of $Gd_{1-x}Co_x$ layer, i.e. the inverse GMR junctions can be induced.

The published results of Yang et al prove that, in bulk of $Gd_{1-x}Co_x$ alloys (i.e. in the core of $Gd_{1-x}Co_x$ layers), β is negative when the magnetisation of $Gd_{1-x}Co_x$ alloys is Co-dominant ($T > T_{comp}$), and it is positive in the case of Gd-dominant magnetisation ($T < T_{comp}$).

5.6.2. The spin asymmetric coefficient of $Gd_{1-x}Co_x$/Cu interfaces and the compensation thichness of $Gd_{1-x}Co_x$ layers

According to the study in ref. [116], whatever the composition of the $Gd_{1-x}Co_x$ layer is, the spin asymmetric coefficient β of Cu/$Gd_{1-x}Co_x$ interface is negative. When β of $Gd_{1-x}Co_x$ layer core is positive, i.e. the magnetisation is Gd-dominant, there is a competition between the spin dependent scatterings in the Cu/$Gd_{1-x}Co_x$ interface ($\beta_{Cu/GdCo} < 0$) and in the $Gd_{1-x}Co_x$ layer core ($\beta_{GdCo} > 0$). In this case, the amplitude and sign of the global β of $Gd_{1-x}Co_x$ layer depend on not only the composition but also the thickness t_{GdCo} of $Gd_{1-x}Co_x$ layer. Consequently, a compensation thickness t^*_{GdCo} of $Gd_{1-x}Co_x$ layer, where the scatterings in the interface and the layer core (bulk) compensates and the global β of $Gd_{1-x}Co_x$ layer is zero, can be induced. When

$t_{GdCo} < t^*_{GdCo}$, the global β of $Gd_{1-x}Co_x$ layer is negative (interface-dominant) and it becomes positive (bulk-dominant) when $t_{GdCo} > t^*_{GdCo}$.

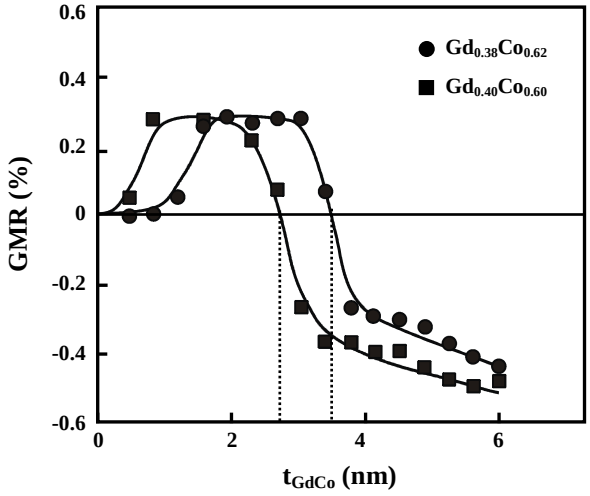

Fig. 5.12. Dependences of GMR ratio of {Fe (2nm)/Cu (3 nm)/$Gd_{1-x}Co_x$ (t_{CoGd})} thin films (x = 0.6 and 0.62) at room temperature on t_{CoGd}. The solid curves serve as guides to the eye (ref. [116]).

The t_{GdCo}-dependences of GMR at room temperature of two samples {Fe (2nm, β < 0)/Cu (3 nm)/$Gd_{0.38}Co_{0.62}$ (t_{GdCo} nm, β > 0)} and {Fe (2nm, β < 0)/Cu (3 nm)/$Gd_{0.40}Co_{0.77}$ (t_{GdCo} nm, β > 0)} imported from ref. [116] are presented in Fig. 5.12. Because the magnetisations of both $Gd_{0.40}Co_{0.60}$ and $Gd_{0.38}Co_{0.62}$ alloys are Gd-dominant at all temperatures, the β of these layer cores is positive, i.e. opposite to the negative β of Cu/GdCo interfaces. Because of the competion between the Cu\GdCo interfacial scatterings (β < 0) and the GdCo layer core scatterings (β > 0), the compensation thicknesses of GdCo layers (t^*_{GdCo}) exist in both samples. Since GMR of sample is zero at the compensation thickness, it can be inferred from Fig. 5.12 that: t^*_{GdCo} = 2.8 nm for $Gd_{0.40}Co_{0.77}$, and t^*_{GdCo} = 3.6 nm for $Gd_{0.38}Co_{0.62}$.

5.7. Conclusion

In this chapter, we have presented a short introduction of the magnetoresistive effects (OMR, AMR, GMR). The spin dependent scattering mechanism has been presented and discussed. The typical behaviours of GMR have been described including the sign reversal of the GMR ratio following the variation of the spin dependent scattering asymmetric coefficient of magnetic layers.

Chapter. 6. Giant magnetoresistance of Fe/Cr multilayers

6.1. Introduction

According to literature, the spin asymmetric coefficients β (=($\rho_\uparrow-\rho_\downarrow$)/($\rho_\uparrow+\rho_\downarrow$)) of Fe, Co, Ni are negative, i.e. the spin ↓ electrons are more scattered than spin ↑ electrons ($\rho_\uparrow < \rho_\downarrow$). In the opposite, in cases of FeCr and NiCr alloys (see Fig. 5.2), they are positive, i.e. $\rho_\uparrow > \rho_\downarrow$ [109]. In Fe/Cr multilayers, the FeCr alloy can be produced at the Fe/Cr interfaces. Because of the opposite sign of the β factors of Fe metal and FeCr alloys, the global factor β of Fe layer depends on the thickness of Fe layers, and a compensation thickness is expected to be induced.

The giant magnetoresistance (GMR) of Fe/Cr magnetic superlattices has been studied and published in the original paper about GMR [90]. Because the thicknesses of all Fe layers are the same, the global factors β of Fe layers are the same, and a normal GMR ($R_{AP} > R_P$) whatever thickness of Cr spacer layers is evidenced. However, because the thickness of Fe layers were fixed at 3 nm, i.e. the global factor β of Fe layers is fixed, the question about the effect of β on GMR of Fe/Cr multilayers is still open. In addition, in the context of applications comes the question of the high temperature behaviour of GMR. In order to tackle these points, in this chapter, we consider the GMR effect of sputtered Fe/Cr multilayers with a fixed Cr-individual layer thickness and variable Fe-individual layer one. This study was carried out in the years of 2002-2005 at Vietnam National University in Hanoi.

6.2. Experimental details

The $\{Fe/Cr\}_n$ mutilayers with a number of periods n = 60 and with a fixed Cr-individual layer thickness, t_{Cr} = 2 nm and a variable Fe-individual layer thickness, t_{Fe} = 1, 2, 3 and 6 nm were prepared by rf-magnetron sputtering. The typical power during sputtering was 100 W and the Ar pressure was 10^{-2} mbar. The substrates were glass with a nominal thickness of 0.5 mm. Both target and sample holder were water-cooled.

Samples were annealed at temperatures from T_A = 200 ^oC to 500 ^oC for 1 hour in vacuum of 5×10^{-5} mbar. The crystalline structure of films was investigated by X-ray diffraction using Cu K_α radiation (Siemens D5000 diffractometer). The magnetisation was measured at room temperature in applied fields up to 1.3 T using the VSM technique.

The magnetoresistance was measured by the four-point technique in current-in-plane configuration and longitudinal geometry. The applied field could be increased up to 0.8 T by using a Cu coil electromagnet at room temperature. The low temperature measurements could

be carried out from the nitrogen liquid temperature (77 K) to room temperature by using the technique described in section 2.10.1.

6.3. Magnetic properties and GMR of Fe/Cr multilayers at 300 K

6.3.1. GMR of as-deposited Fe/Cr multilayers at 300 K

The room temperature GMR ratio $\Delta R/R$ (= $(R_H - R_0)/R_0$, where R_0 and R_H are the resistances in zero field and in applied field $\mu_o H$, respectively) of the as-deposited Fe/Cr multilayers is presented in Fig. 6.1. The results show a normal GMR as expected and the initial magnetoresistive susceptibility of the as-deposited samples is almost constant χ_R (=$(\Delta R/R)/\mu oH$) ≈ 13% T^{-1}. The saturation field, however, increases with decreasing Fe-layer thickness. So that, a maximal magnetoresistance ratio $\Delta R/R$ of 0.7 % is reached in the sample with t_{Fe} = 1 nm. This finding shows that the volume Fe-fraction increases, i.e. the volume/interface fraction ratio increases, while the GMR effect decreases. The result seems to support the dominant contribution of Fe/Cr interfaces to the GMR ratio.

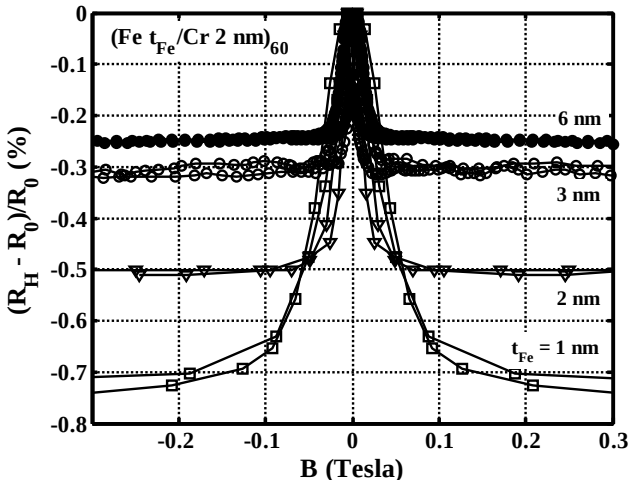

Fig. 6.1. GMR data for (Fe t_{Fe}/Cr 2 nm)$_{60}$ multilayers at 300 K. The Fe layer thickness t_{Fe} is respectively varied 1 nm, 2 nm, 3 nm, and 6nm.

Although the GMR ratio is not governed by the asymmetric factor β of magnetic layers alone, the GMR ratio always increases with the increase of amplitude of β (refs. [106], [109], and [116]). In the cases of Fe/Cr multilayer, because β is negative in the Fe layer cores and positive at the Fe/Cr interfaces where the FeCr alloys is created (see section 5.2.3), the global spin asymmetric coefficient β of the Fe layers depends on the Fe layer thickness (t_{Fe}), and the compensation thickness of Fe layers (t^*_{Fe}) may be produced. When $t_{Fe} = t^*_{Fe}$, the global β is zero and the GMR ratio is zero as a consequence. Near the compensation thickness, GMR will increase following the increase of the difference $|t_{Fe} - t^*_{Fe}|$.

According to experimental results in Fig. 6.1, when t_{Fe} increases from 1 nm to 6 nm, the amplitude of GMR ratio decreases monotonously, it proves that t^*_{Fe} of the Fe layers is not in this range of t_{Fe}, i.e. the global β does not change in sign. Therefore, there are only two possibilities for t^*_{Fe} corresponding to two possibilities of β:

- $t^*_{Fe} < 1$ nm: When $t_{Fe} \geq 1$ nm, β of Fe layer cores overcomes the one of Fe/Cr interfaces, so the global factor β of Fe layers is negative. In this case, when t_{Fe} increases from 1 nm to 6 nm, the amplitude of global β increases too, and the GMR is expected to increase. However, the experimental results presented in Fig. 6.1 proves that the GMR ratio decreases with the increase of t_{Fe}. So $t^*_{Fe} < 1$ nm is not reasonable.
- $t^*_{Fe} > 6$ nm: β of Fe/Cr interfaces overcomes the one of Fe layer cores, so the global factor β is positive for all cases with $t_{Fe} \leq 6$ nm. When t_{Fe} decreases from 6 nm to 1 nm, the fraction of Fe layer cores decreases, so the amplitude of global β is increased, and the GMR ratio is expected to increase. The assumption $t^*_{Fe} > 6$ nm agrees well with experiment, so it should be right.

The global factor β of Fe layers will be discussed more in the next section where the Fe/Cr interfaces are widened using heat treatments.

Table. 6-1: Dependence of the saturation field of (Fe t_{Fe}/Cr 2 nm)$_{60}$ multilayers on the Fe layers thickness.

Fe layers thickness t_{Fe} (nm)	1	2	3	6
Saturation field $\mu_o H_S$ (Tesla)	0.075	0.035	0.024	0.022

Concerning the saturation field $\mu_o H_S$ of GMR curves (Table. 6-1), it is clear that the thicker the Fe layer is, the smaller the saturation field is. According to literature, there is a positive agreement between the antiparallel coupling intensity of magnetic successive layers and the GMR ratio [92]. The stronger the antiparallel coupling is, the larger the GMR ratio is. In the case of Fe/Cr multilayers, the antiparallel coupling between successive Fe layers is strongest, corresponding to a maximum saturation field of 0.075 Tesla, when the thickness of Fe layers is 1 nm. This antiparallel coupling is confirmed in Fig. 6.4 with a zero remanent magnetisation of the as-deposited Fe (1 nm)/Cr sample measured at room temperature.

6.3.2. The effect of heat treatments

Annealing effects on the GMR are presented in Fig. 6.2 for the Fe/Cr multilayers with t_{Fe} = 1 nm. The GMR ratio initially increases with increasing the annealing temperature and

reaches a maximum value of 2.3 % at T_A = 350 °C. With further increasing T_A, the GMR ratio decreases, e.g. after annealing at 500 °C, the GMR ratio equals 0.3 % only. A similar result was observed for samples with t_{Fe} = 2 nm. Such a tendency of GMR has been recently reported for Cu/Co by Hecker et al [123].

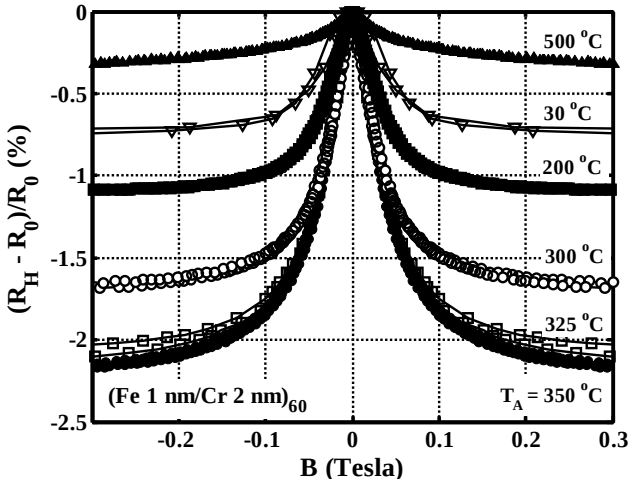

Fig. 6.2. GMR data at 300K for annealed (Fe 1 nm/Cr 2 nm)$_{60}$ films.

These results can be explained as follows. The annealing at $T_A \leq 350$ °C is usually thought to make a break-up of the layers due to the interdiffusion and to the broadening of interfaces. This leads to an increasing interface/volume fraction, i.e. the amplitude of global factor β of Fe layers is increased, and then to the enhancement of the GMR. The effect of annealing at 500 °C, however, is attributed to a further break-up of the layers, leading to the formation of heterogeneous structures of small particles. This argument has been proposed earlier by Flores et al [124].

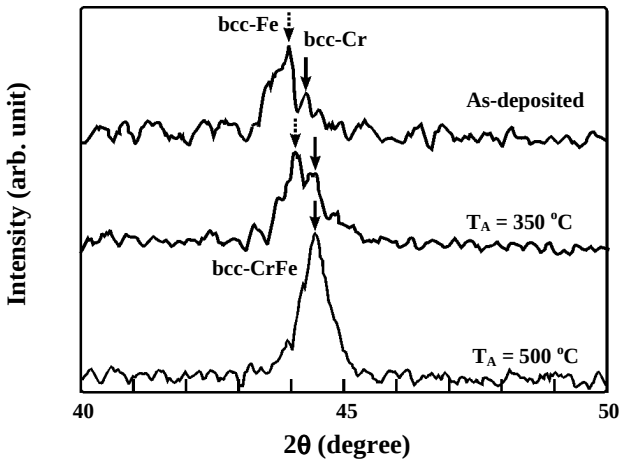

Fig. 6.3. XRD patterns of Fe(1 nm)/Cr multilayers.

XRD results of the Fe(1 nm)/Cr(2 nm) multilayers (Fig. 6.3) strongly support the above argument. At $T_A \leq 350$ °C, the stability of individual Fe- and Cr-layers is well evidenced by the

(110) bcc-Fe and (110) bcc-Cr reflections. At T_A = 500 ^oC, however, a broadened Bragg peak is observed indicating the formation of bcc-CrFe phases.

The magnetisation curves of Fe(1 nm)/Cr(2 nm) multilayers annealed at 30 ^oC (as-deposited sample), 350 ^oC and 500 ^oC are presented in Fig. 6.4. The magnetisation curve of as-deposited sample has a usual behaviour of antiparallel-coupled multilayer (zero remanent magnetisation) with a saturation field of 40 mT. The saturation field is largest when T_A = 350 ^oC, this suggests an increase of the antiparallel coupling intensity of Fe successive layers, and explains why the GMR ratio reaches a maximum value when T_A = 350 ^oC. In the case of T_A = 500 ^oC, the saturation field is smallest and the magnetisation curve becomes quite square like the curve of a ferromagnetic material. This behaviour proves again that the antiferromagnetic coupling breaks down and a ferromagnetic one is established. The system, thus, can no longer switch between an antiparallel (ground state) and parallel aligned state (applied field), and GMR ratio decreases consequently.

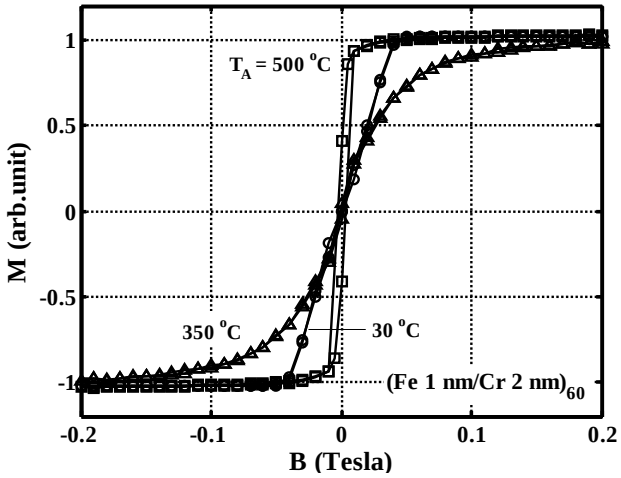

Fig. 6.4. Hysteresis loops at room temperature of Fe(1 nm)/Cr samples annealed at 350 ^oC, 500 ^oC, and as-deposited sample (T_A = 30 ^oC).

The increase of GMR ratio can also be understood in terms of the spin asymmetric coefficient β of Fe layers. As mentioned in previous section (t^*_{Fe} > 6 nm), when $t_{Fe} \leq 6$ nm, the spin dependent scattering in Fe/Cr interfaces (β > 0) is dominant and the global spin asymmetric factor β of Fe layers is positive. Under the effect of a heat treatment, which induces interdiffusion and interface alloying, the Fe/Cr interfaces are widened while the Fe layer cores are narrowed. The increase of interface/volume fraction makes an increase of the amplitude of global factor β of Fe layers, therefore the GMR ratio is increased. When samples are annealed above 350 K, the collapse of the multilayer structure makes GMR decrease.

6.4. Magnetic property and GMR of Fe/Cr multilayer at low temperature

The GMR curves measured at different temperatures are presented in Fig. 6.5 for sample with t_{Fe} = 1 nm annealed at T_A = 350 ^oC. Note that the GMR ratio measured in $\mu_o H$ = 0.3 T increases linearly with decreasing temperature and reaches a value as large as 7.7 % at 77 K. This GMR ratio is about four times larger than that at room temperature.

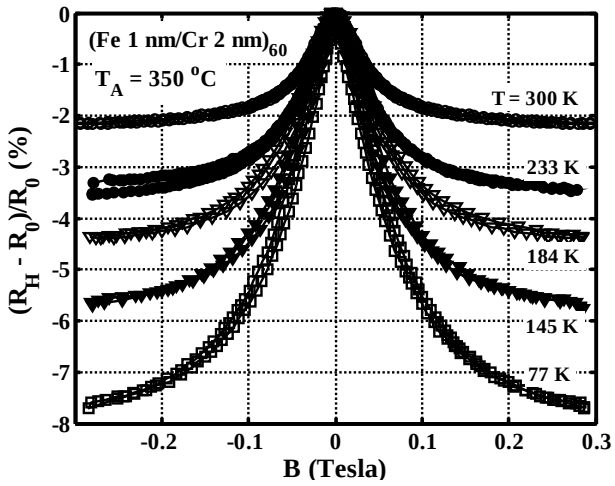

Fig. 6.5. Low-temperature GMR data of Fe(1 nm)/Cr samples annealed at 350 ^oC.

The increase of GMR at low temperature may relate to the following causes:

- The enhancement of the antiferromagnetic coupling: This enhancement can be seen in Fig. 6.5 showing an increases of the saturation field as the temperature decreases
- The decrease of longitudinal resistivity of thin film: Because the contribution from phonons to resistivity is reduced at low temperature, the resistivity of thin films is reduced.

6.5. Conclusion

Our investigations suggest the important role of the scattering at the interfaces. It reveals also that the layer structure of sputtered Fe/Cr multilayers remains stable during annealing up to 350 ^oC. For heat treatments at higher temperatures, the multilayer structure is modified and the onset of a ferromagnetic coupling is found, leading to the reduction of the GMR signal. [These results have been published in Physica B in 2003.]

Chapter. 7. Giant magnetoresistance junction based on GdCo compensated ferrimagnet

7.1. Introduction

Up to now, most GMR junctions are made out of magnetic layers based on transition metal alloys. Since the temperature experimental range is much lower than their Curie temperature, such layers can be considered to have constant magnetisation. Moreover, the common GMR elements usually use magnetic layers with in-plane anisotropy.

In this chapter, $Gd_{1-x}Co_x$ alloy is going to be applied to make a new type of GMR junction with a perpendicular anisotropy of the $Gd_{1-x}Co_x$ layer. With a compensation temperature of about 200 K, the magnetisation of $Gd_{1-x}Co_x$ layer is tuneable by adjusting the temperature from 5 K up to 300 K. Additionally, the spin polarisation can be changed in sign from negative (below T_{comp}) to positive (above T_{comp}) [54]. In this chapter, the extraordinary Hall effect measured in the in-plane or perpendicular applied field will be used as an advanced method to investigate the rotation of $Gd_{1-x}Co_x$ magnetisation.

7.2. GMR junction using $Gd_{1-x}Co_x$

7.2.1. Deposition, organisation, and characterisation of thin films

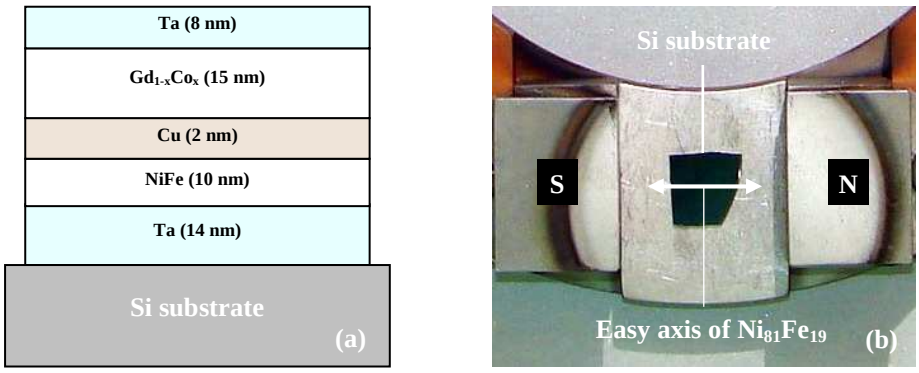

Fig. 7.1. The configuration of GMR junction using $Gd_{1-x}Co_x$ layer (a) and the position of substrate during deposition with an in-plane bias magnetic field (b) to make an in-plane easy axis of Permalloy (EAP).

The structure of GMR junctions used in this chapter is shown in Fig. 7.1.a. The junction is deposited on Si substrate. $Ni_{81}Fe_{19}$ is used as a soft ferromagnetic layer (10 nm), its

anisotropy is in-plane and magnetisation can be rotated easily by a small in-plane applied field. The Cu layer plays the role of non-magnetic metallic spacer in GMR junction. The $Gd_{1-x}Co_x$ layer (15 nm) is sputtered by using the target couple of $Gd_{14}Co_{86}$-$Gd_{10}Co_{90}$ to get the compensation temperature near 200 K. The GMR junction is protected from oxidation by two Ta capping and buffer layers. Because of an in-plane bias magnetic field generated by two $SmCo_5$ permanent magnets during deposition, an in-plane easy axis of $Ni_{81}Fe_{19}$ (EAP) is created in the same direction as the bias field. The magnetoresistance (MR) and the Hall effect measurements will be measured in three directions of applied field (B): in-plane and parallel to easy axis of $Ni_{81}Fe_{19}$ (B // EAP), in-plane and perpendicular to easy axis of $Ni_{81}Fe_{19}$ (B // film, B ⊥ EAP), and perpendicular to the film (B ⊥ EAP). The magnetisation of GMR junction will be investigated using VSM measurement at room temperature (300 K). The measured data is a mixture of MR signal and Hall effect signal. In order to separate MR signal and EHE signal from each other, the mathematical method (odd/even part) described in section 2.10.3 has been applied for all experimental data of GMR junctions.

7.2.2. Perpendicular anisotropy of as-deposited GMR junction

The $Gd_{1-x}Co_x$ layer is deposited on top of the junction. The 8 nm Ta capping layer is thin enough to enable the domain structure of $Gd_{1-x}Co_x$ layer to be observed by PKE imaging.

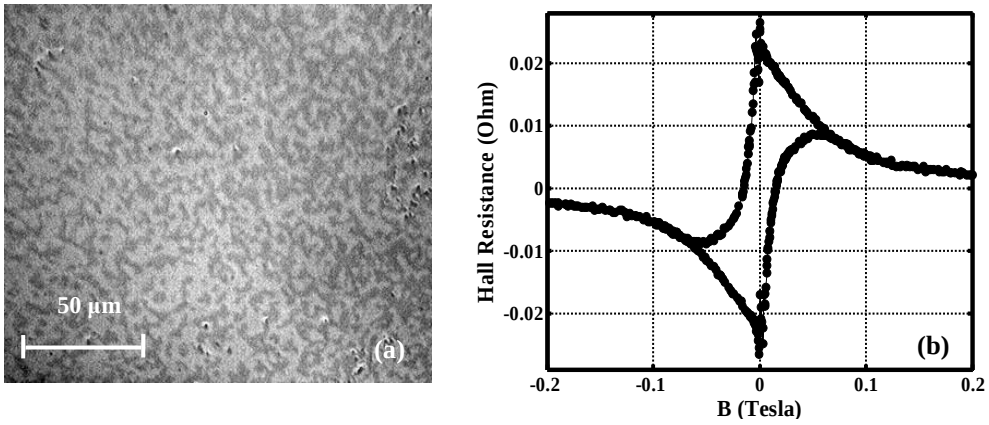

Fig. 7.2. The polar Kerr image without applied field (a) and the EHE loop measured with in-plane applied field (b) of the as-deposited sample.

The polar Kerr image at 300 K of the as-deposited sample is shown in Fig. 7.2.a. Although the contrast of image is decreased because of Ta capping layer, the contrast is still enough to see the multidomain structure and to prove that $Gd_{1-x}Co_x$ layer has a perpendicular anisotropy at room temperature, i.e. the spontaneous magnetisation of $Gd_{1-x}Co_x$ has a large perpendicular component.

The perpendicular anisotropy of $Gd_{1-x}Co_x$ layer can be also detected by using the extraordinary Hall effect (EHE), i.e. the remanent EHE, in either perpendicular or in-plane applied field. The in-plane applied field EHE loop of sample is presented in Fig. 7.2.b, the remanent Hall resistance is about 0.026 Ω, it is equivalent to a Hall resistivity of about 2.5 μΩ.cm. The existences of Ta, Cu, and NiFe layers makes EHE decrease significantly, nevertheless, the remanent Hall resistivity is large enough (comparing to maximum ρ_H = 3.2 μΩ.cm of $Gd_{1-x}Co_x$ layer) to affirms the existence of perpendicular anisotropy, i.e. perpendicular spontaneous magnetisation, in $Gd_{1-x}Co_x$ layer.

7.3. AMR and GMR of the sample

7.3.1. Anisotropic magnetoresistance (AMR) of $Ni_{81}Fe_{19}$ layer

The in-plane magnetisation hysteresis loops measured in two directions perpendicular and parallel to the easy axis of permalloy $Ni_{81}Fe_{19}$ (EAP) are presented in Fig. 7.3. In the case of B // EAP, the magnetisation is fully remanent, i.e. the spontaneous magnetisation of $Ni_{81}Fe_{19}$ layer is 100% aligned in the EAP direction. The coercive field of $Ni_{81}Fe_{19}$ layer is about $\mu_o H_C$ = 0.5 mT and the hysteresis loop is quite square. When B ⊥ EAP, the remanent magnetisation is zero, and the saturation field is about $\mu_o H_S$ = 1.0 mT. The results confirm that there is an in-plane easy axis of $Ni_{81}Fe_{19}$ layer created during deposition.

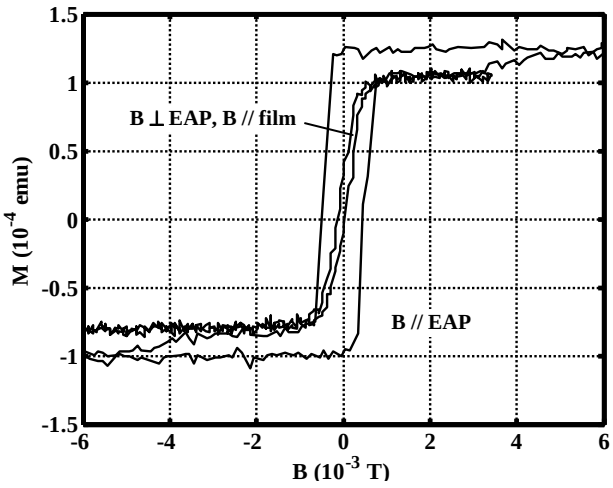

Fig. 7.3. The in-plane magnetisation loops of GMR film at 300 K for both cases when the applied field is perpendicular and parallel to the easy axis of Permalloy $Ni_{81}Fe_{19}$ layer.

Because VSM measurement is not sensitive enough to measure the magnetic moments of the thin $Gd_{1-x}Co_x$ layer (15 nm) near its compensation temperature, EHE is going to be used as an advanced method for investigating the orientation of $Gd_{1-x}Co_x$ magnetisation.

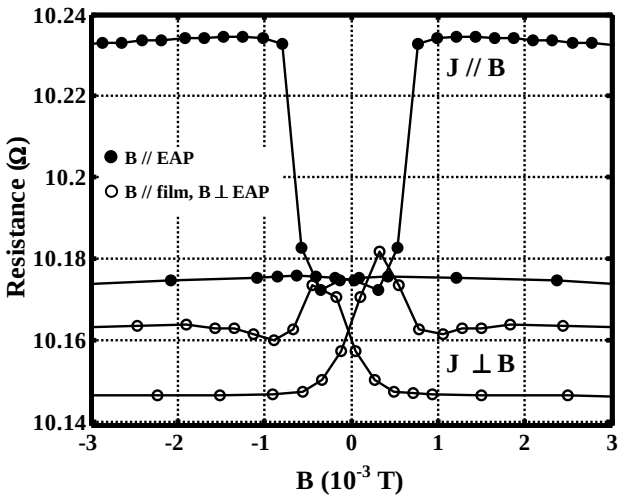

Fig. 7.4. The low field resistance curves of GMR film measured for two cases with an in-plane applied field: B // EAP (open circles) and B ⊥ EAP (solid circles). The applied current is parallel to EAP with the same contacts for both measurements.

In order to measure AMR of the NiFe layer of GMR film, a dc current was applied parallel to the easy axis of $Ni_{81}Fe_{19}$ (EAP) and an in-plane external magnetic field was applied either perpendicular (J ⊥ B) or parallel (J // B) to EAP. The experimental low-field resistances of the GMR film are presented in Fig. 7.4 for both measurements (J // B and J ⊥ B). When the applied field increase from 0 to 1 mT, in the case of J // B the resistance increases up to 10.235 Ω, whereas the resistance decreases down to 10.145 Ω in the case of J ⊥ B. Comparing this low-field behaviour of the GMR film resistance to the typical behaviour of AMR presented in Fig. 5.3, we can conclude that the AMR of $Ni_{81}Fe_{19}$ layer exists in the GMR film. The AMR ratio can be calculated as (5.3): AMR = (10.235-10.145)/10.145 = 0.9%, it is equivalent to half the AMR of $Ni_{81}Fe_{19}$ single layer at room temperature (2%). The decrease of AMR here may be due to the existence of Ta, GdCo, and Cu layers in GMR junction, which act as short circuits.

7.3.2. Giant magnetoresistance (GMR) of the sample

Theoretically, in the case of GMR the resistance of the sample does not depend on the angle between applied field and applied current but depends on the angle between magnetisations of two magnetic layers in GMR junction. The resistance at 300 K of the sample measured in two cases B // EAP and B ⊥ EAP are represented in Fig. 7.5 in higher applied fields. Because MR ratios ($=(R_0 - R_H)/R_0$) are positive ($MR_{B\ //\ EAP}$ = 0.90%, $MR_{B\perp EAP}$ = 0.64%) for both measurements, the magnetoresistance here is obviously giant magnetoresistance (GMR). However, the amplitude of GMR ratio in the case of B // EAP is larger than that in the case of B ⊥ EAP.

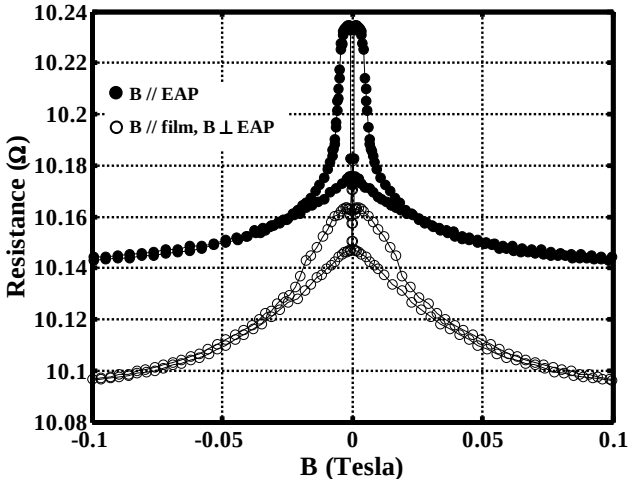

Fig. 7.5. The giant magnetoresistance (GMR) of the sample at 300 K. The applied current is parallel to the EAP. The sign of GMR does not depend on the angle between the applied field and the applied current.

According to VSM measurements (Fig. 7.3), the in-plane saturation field of $Ni_{81}Fe_{19}$ layer is smaller than 0.001 T. Above 0.001 T, the magnetisation of $Ni_{81}Fe_{19}$ layer is parallel to the applied field, therefore, the variation of resistance in applied field above 0.001 T can be attributed to the rotation of $Gd_{1-x}Co_x$ magnetisation from the perpendicular direction of the film.

7.4. GMR at room temperature

7.4.1. In-plane applied field GMR

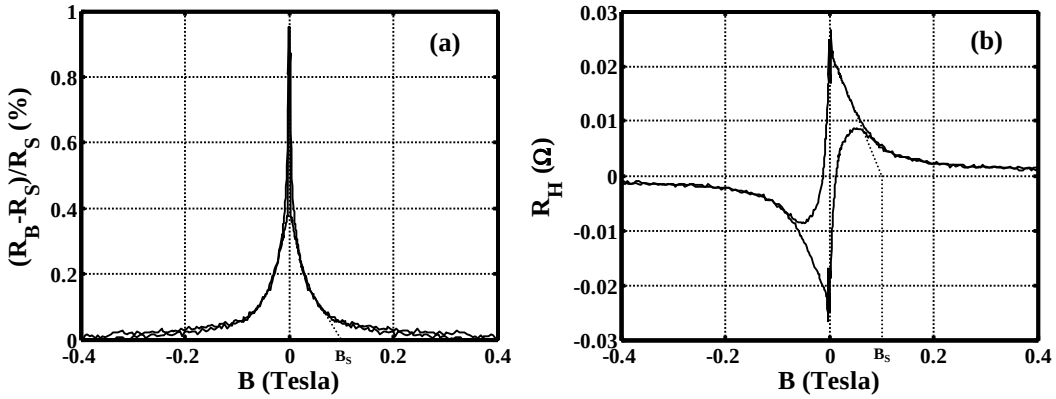

Fig. 7.6. GMR loop (a) and EHE loop (b) of the sample at 300K for the case of B // EAP. R_S is the resistance of GMR sample at 0.4 Tesla.

At 300 K and in the case B // EAP, a GMR of 1% is obtained in the applied field of 0.4 Tesla (see Fig. 7.6.a). Because the $Ni_{81}Fe_{19}$ magnetisation will be in-plane saturated with an applied field of 0.001 T, the further increase of the applied field makes the $Gd_{1-x}Co_x$ magnetisation turn from perpendicular direction to in-plane direction.

The rotation of $Gd_{1-x}Co_x$ magnetisation can be detected by means of EHE. The Hall resistance loops at 300 K in the case of B // EAP is shown in Fig. 7.6.b. We can see that EHE has perpendicular remanence at 300 K because of the perpendicular anisotropy of $Gd_{1-x}Co_x$ layer. In zero applied field, the magnetic configuration of sample is perpendicular as illustrated in Fig. 7.7.a, and the resistance of sample is maximum ($R_{max} = R_0$). When the in-plane applied field increases, the $Gd_{1-x}Co_x$ magnetisation rotates from the perpendicular direction, and the perpendicular component (z-component) of $Gd_{1-x}Co_x$ magnetisation decreases, therefore the Hall resistance decreases consequently (Fig. 7.6.b). When the in-plane applied field exceeds the in-plane saturation field (B_S) of $Gd_{1-x}Co_x$ layer, the $Gd_{1-x}Co_x$ magnetisation is in-plane saturated and the magnetic configuration becomes parallel as illustrated in Fig. 7.7.b. The resistance is minimum in this saturation state ($R_{min} = R_S$).

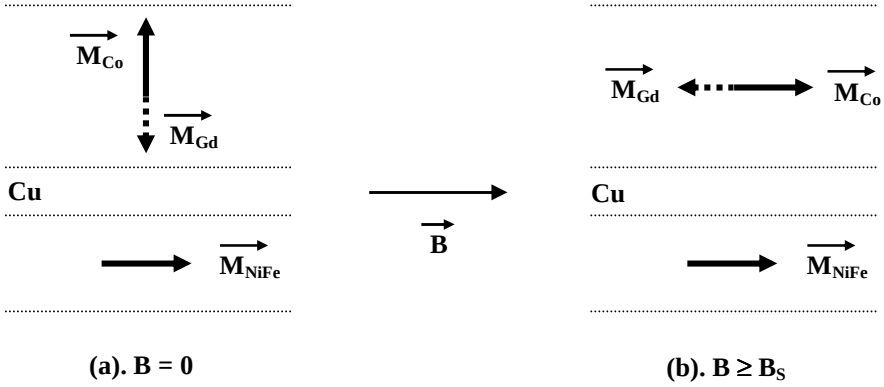

Fig. 7.7. The schematic magnetic configurations of sample in zero applied field (a) and in the in-plane saturation field (b) for the case that the $Gd_{1-x}Co_x$ magnetisation is Co-dominant.

The saturation field extrapolated from EHE loop is B_S = 0.1 T (Fig. 7.6.b), it quite agrees with the saturation field extrapolated from GMR loop (Fig. 7.6.a). It means that the GMR of the sample saturates when the magnetisations of $Ni_{81}Fe_{19}$ and $Gd_{1-x}Co_x$ layers get parallel to each other. Furthermore, at 300 K, the GMR of sample is normal GMR ($R_{H=0} > R_{H=Hs}$), it means that the spin dependent scattering asymmetric coefficients (β) of the $Gd_{1-x}Co_x$ and $Ni_{81}Fe_{19}$ layers have the same sign.

7.4.2. Perpendicular applied field

Fig. 7.8 presents GMR loop (a) and EHE loop (b) of the sample at 300 K measured in perpendicular applied field (B ⊥ film). Because the compensation temperature of $Gd_{1-x}Co_x$ layer is near 200 K, EHE of $Gd_{1-x}Co_x$ at 300 K is positive in the perpendicular applied field measurement. The perpendicular anisotropy of $Gd_{1-x}Co_x$ layer at 300 K makes its magnetisation easy to get the perpendicular saturation state, and the EHE of the $Gd_{1-x}Co_x$ layer is expected 100% remanent. In addition, the Hall effect of $Ni_{81}Fe_{19}$ is also positive, therefore the rotation of

$Ni_{81}Fe_{19}$ magnetisation to the perpendicular direction makes positive contribution to EHE. That is why the Hall resistance (R_H) increases over the remanent R_H in higher perpendicular applied fields (Fig. 7.8.b).

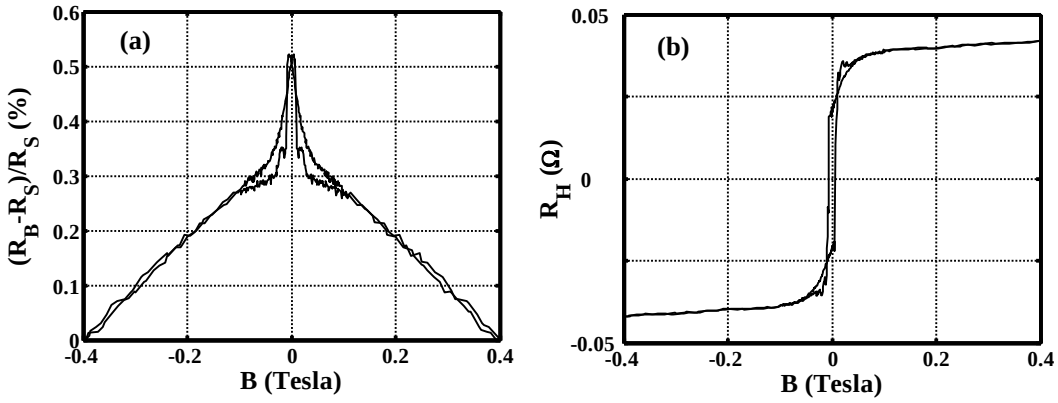

Fig. 7.8. GMR loop (a) and EHE loop (b) of the sample at 300K for the case of B ⊥ film. R_S is the resistance of sample at 0.4 Tesla. The R_H has a perpendicular remanence.

If the applied field exceeds the perpendicular saturation field B_S of $Ni_{81}Fe_{19}$ layer, the magnetisation of $Ni_{81}Fe_{19}$ is fully perpendicular saturated and the magnetic configuration of sample becomes parallel in the normal direction of the film as illustrated in Fig. 7.9.b.

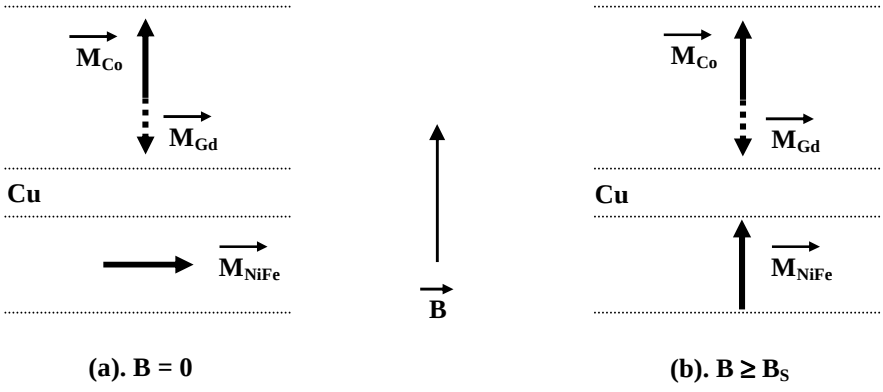

Fig. 7.9. The schematic magnetic configurations of the sample in zero applied field (a) and in the perpendicular saturation field (b) when the $Gd_{1-x}Co_x$ magnetisation is Co-dominant.

According to the high-field (6 T) magnetoresistance and Hall resistance loops of the sample sketched in Fig. 7.10, the perpendicular saturation field of $Ni_{81}Fe_{19}$ layer is about 1 T (B_S = 1 T). The further increase of the applied field makes both R and R_H decrease. The causes are still unclear and may be due to the (negative) ordinary Hall effects of the layers Ta, $Ni_{81}Fe_{19}$, $Gd_{1-x}Co_x$, and Cu. The further studies on GMR of the sample is still going on, hopefully the real causes will be figured out soon in the future.

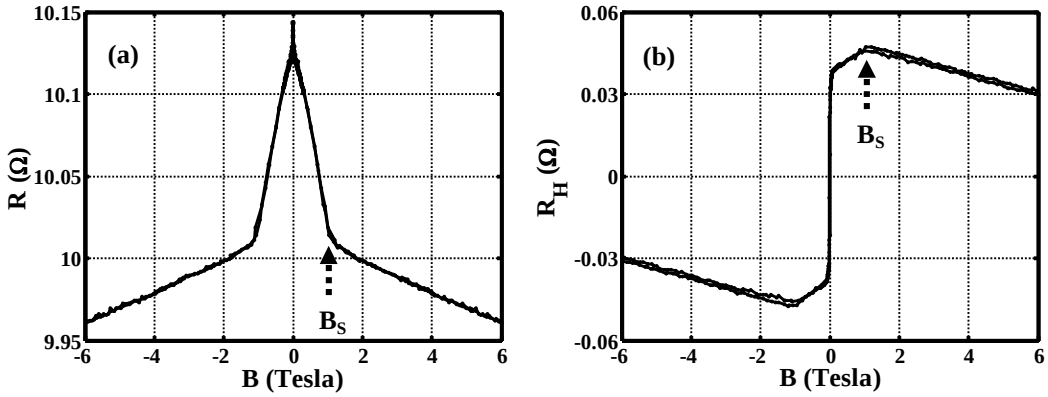

Fig. 7.10. Resistance loop (a) and EHE loop (b) of the sample at 300K for the case of B ⊥ film. The applied field increases up to 6 T. B_S is the perpendicular saturation field of $Ni_{81}Fe_{19}$ layer.

7.5. Magnetoresistance at low temperatures and the sign reversal of GMR

GMR loops at low temperature measured in case of B // EAP are presented in Fig. 7.11. It is clear that the saturation field of GMR becomes larger at temperature near 200 K. When temperature is varied, the GMR ratio changes not only in amplitude but also in sign.

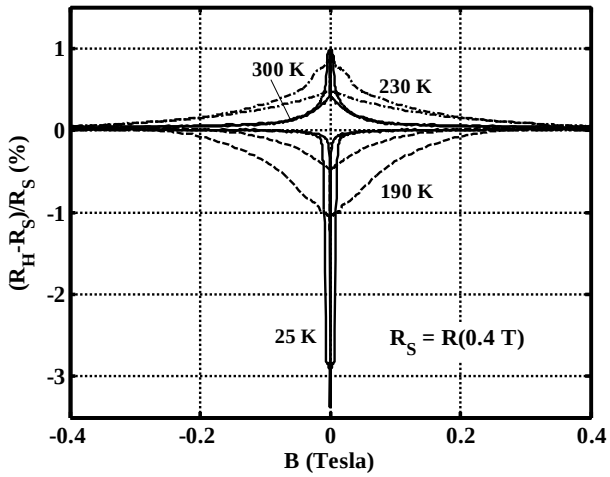

Fig. 7.11. GMR loops of sample at low temperatures. The field B is applied parallel to the easy axis of $Ni_{81}Fe_{19}$ (EAP). R_S is the resistance of sample at 0.4 Tesla.

The temperature dependence of GMR presented in Fig. 7.12 shows a sign reversal at 210 K. GMR seems constant at temperatures below 50 K (GMR = -3.2% at T ≤ 50 K) or at temperatures from 250 K to 300 K (GMR = +1.0% at T ∈ [250 K, 300 K]). The amplitude of GMR changes regularly following the variation of temperature from 50 K up to 250 K.

As described in section 5.5, the sign of GMR of the film $Ni_{81}Fe_{19}/Cu/Gd_{1-x}Co_x$ depends on the term $\beta_{NiFe}\beta_{GdCo}$. GMR is positive (respectively negative) when $\beta_{NiFe}\beta_{GdCo}$ is positive (respectively negative). Because $Ni_{81}Fe_{19}$ is a strong ferromagnetic material with a Curie

temperature of 869 K, below 300 K, the magnetisation and spin polarisation of $Ni_{81}Fe_{19}$ is nearly constant. Furthermore, the thickness of $Ni_{81}Fe_{19}$ layer is fixed at 10 nm, so the spin asymmetric coefficient of $Ni_{81}Fe_{19}$ layer (β_{NiFe}) is quite stable in amplitude and not changed in sign below 300 K. The sign reversal of GMR at T_{comp} of $Gd_{1-x}Co_x$ must be attributed to the $Gd_{1-x}Co_x$ layer.

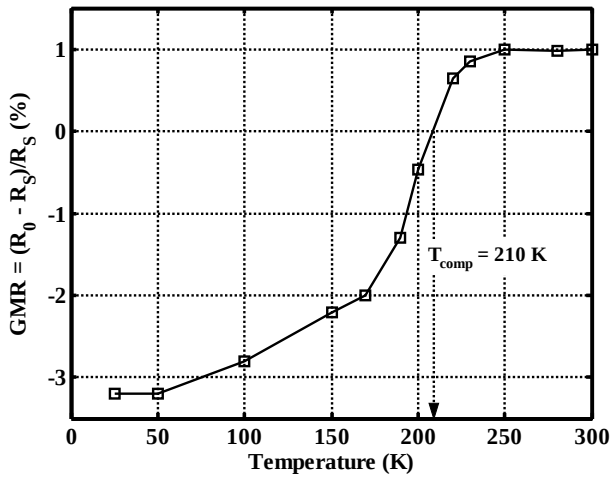

Fig. 7.12. The temperature dependence of GMR measured in the case of B // EAP. R_S is the resistance of sample at 0.4 Tesla.

According to the EHE curves measured in configuration of B ⊥ film, the EHE at 200 K and 220 K have opposite signs (Fig. 7.13), it means that the compensation temperature of $Gd_{1-x}Co_x$ layer (T_{comp}) is between 200 K and 220 K, i.e. $T_{comp} \approx 210$ K. We can conclude that the GMR of sample reverses at T_{comp}. Closer to T_{comp}, the $Gd_{1-x}Co_x$ magnetisation decreases while the perpendicular anisotropy is still stable, therefore the $Gd_{1-x}Co_x$ layer is more difficult to get the in-plane saturation state. The closer to T_{comp} the temperature is, the larger the in-plane saturation field of GMR is. The increase of the in-plane saturation field of GMR near T_{comp} is attributed to the increase of the in-plane saturation field of $Gd_{1-x}Co_x$ magnetisation around T_{comp}. In addition, when the $Gd_{1-x}Co_x$ magnetisation reverses from Gd-dominant ($T < T_{comp}$) to Co-dominant ($T > T_{comp}$) at T_{comp}, the spin asymmetric coefficient of $Gd_{1-x}Co_x$ layer (β_{GdCo}) changes from positive to negative (see section 5.6.2), therefore the GMR ratio consequently reverses its sign at T_{comp}. The decrease of the amplitude of β_{GdCo} may lead to the reduction of GMR in vicinity of T_{comp}.

The obtained results prove that the resistance of the sample depends on the configuration of the $Ni_{81}Fe_{19}$ layer magnetisation ($\overrightarrow{M_{NiFe}}$) and the $Gd_{1-x}Co_x$ layer magnetisation ($\overrightarrow{M_{GdCo}}$). Above T_{comp}, the $Gd_{1-x}Co_x$ magnetisation is Co-dominant, and the resistance of sample is minimum when $\overrightarrow{M_{GdCo}}$ and $\overrightarrow{M_{NiFe}}$ are parallel, i.e. the magnetisation

of $Ni_{81}Fe_{19}$ layer and the Co sublattice magnetisation ($\overrightarrow{M_{Co}}$) are parallel. Oppositely, below T_{comp} the $Gd_{1-x}Co_x$ magnetisation is Gd-dominant, and the resistance of sample is maximum when $\overrightarrow{M_{NiFe}}$ and $\overrightarrow{M_{GdCo}}$ are antiparallel, i.e. $\overrightarrow{M_{NiFe}}$ and $\overrightarrow{M_{Co}}$ are antiparallel.

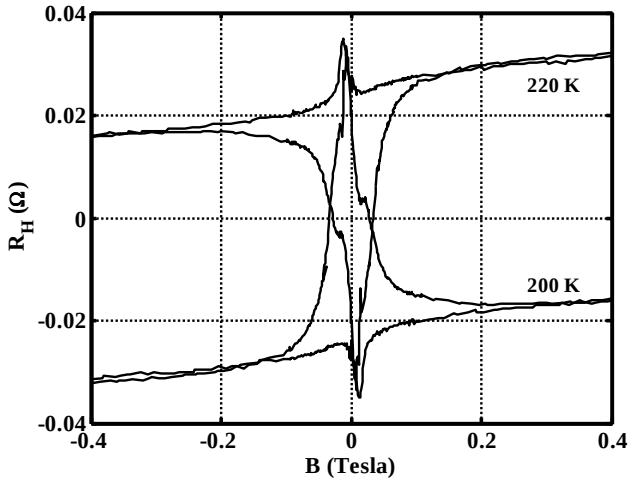

Fig. 7.13. The Hall loops at 200 K and 220 K measured with applied fields perpendicular to film. The Hall loops reveal a T_{comp} = 210 K of $Gd_{1-x}Co_x$ layer.

So far, since the Co and Gd sublattice magnetisations ($\overrightarrow{M_{Gd}}$ and $\overrightarrow{M_{Co}}$) keep antiparallel, the specific contributions of $\overrightarrow{M_{Gd}}$ and $\overrightarrow{M_{Co}}$ to GMR are still an open question, but it could be interpreted as if $\overrightarrow{M_{Co}}$ only.

7.6. GMR in high in-plane applied field (up to 6 Tesla)

All previous measurements have been done in low applied fields (below 0.6 T) where the spin-flop phenomenon of $Gd_{1-x}Co_x$ does not happen. In this section, an external magnetic field up to 6 T will be applied, and temperature will be changed from 5 K to 300 K. Because the spin-flop field of $Gd_{1-x}Co_x$ alloys significantly decreases in vicinity of T_{comp}, the spin-flop phenomenon of $Gd_{1-x}Co_x$ layer can occur in applied fields smaller than 6 Tesla around T_{comp} = 210 K. So the effect of spin-flop phenomenon of $Gd_{1-x}Co_x$ layer on GMR of the sample can be experimentally investigated.

GMR loops of the sample at low temperatures are presented in Fig. 7.14. Except for the reversal of low field GMR at T_{comp} (210 K), a significant decrease of GMR at high field can be observed clearly. Below T_{comp} (210 K) where the low-field GMR is negative, the decrease of resistance at high field looks more obvious, and the applied field where the decrease starts happening (so-called critical field) becomes smaller near T_{comp}. This behaviour of the critical field is similar to the behaviour of the spin-flop field in $Gd_{1-x}Co_x$ alloys (Chapter 4).

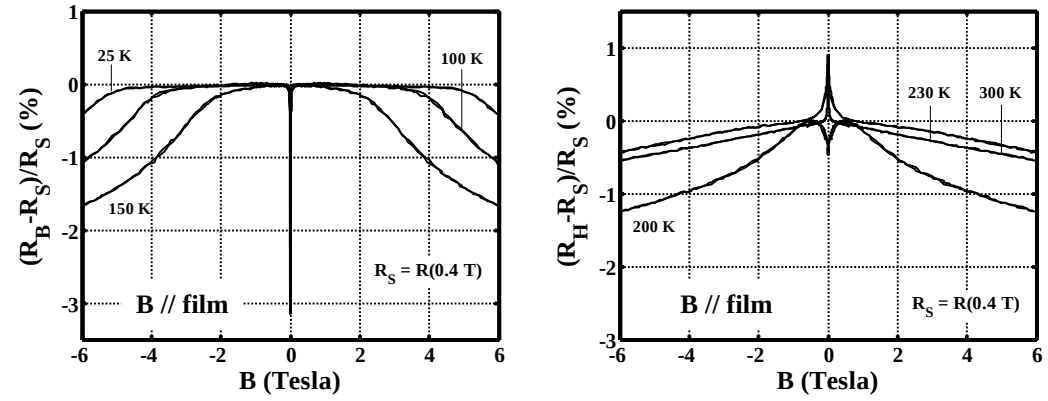

Fig. 7.14. The temperature dependences of GMR where R_S is the resistance of sample at 0.4 Tesla. The applied field is parallel to the film.

In order to check if the decrease of GMR at high field is due to the spin-flop phenomenon of $Gd_{1-x}Co_x$ layer, the sample has been investigated by means of EHE. The EHE loops of the sample at low temperatures are presented in Fig. 7.15.

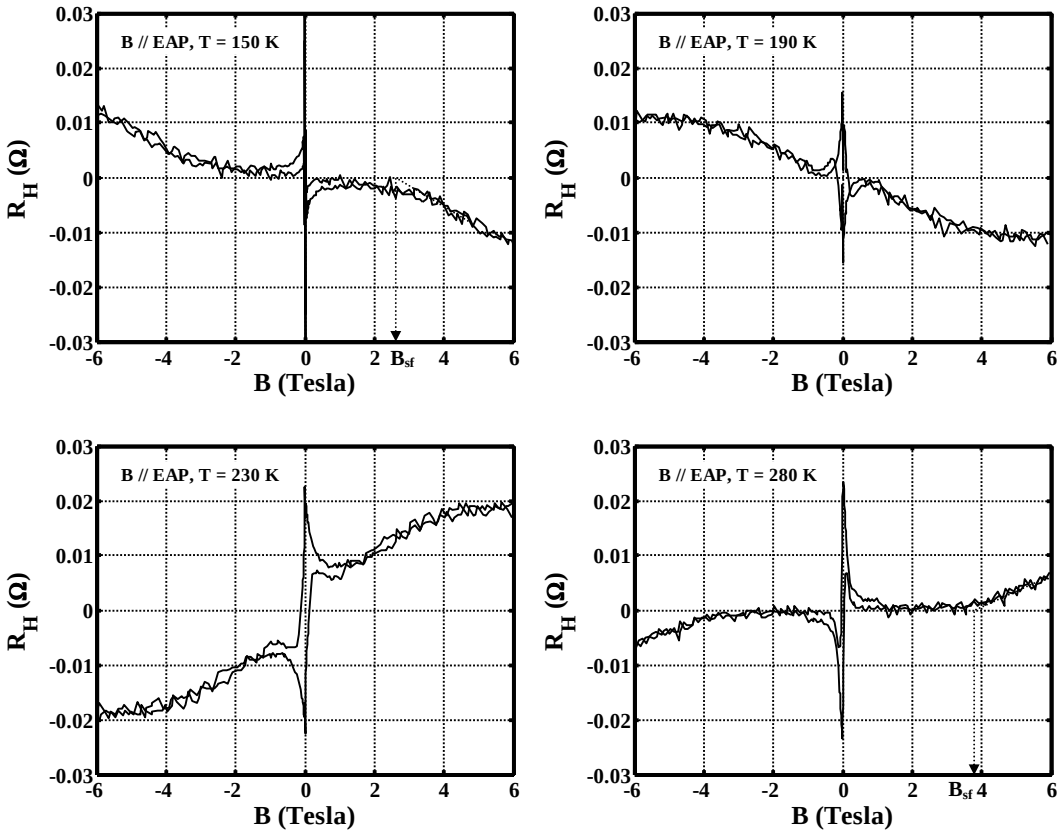

Fig. 7.15. The Hall loops at 150 K, 190 K, 230 K, and 280 K measured with in-plane applied fields. The spin-flop fields (B_{sf}) can be seen clearly at 150 K (B_{sf} = 2.6 T) and 280 K (B_{sf} = 3.8 T)

The increase of the Hall resistance (R_H) at high fields can be seen clearly. Because the applied field is in-plane, the increases of R_H at high fields show the increases of the z-

component of the Co sublattice magnetisation above the spin-flop field. Therefore, the decrease of GMR at high fields is due to the spin-flop of $Gd_{1-x}Co_x$ layer.

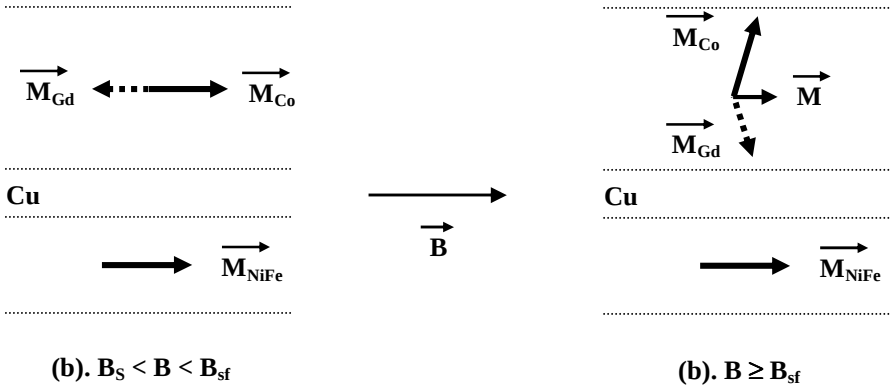

Fig. 7.16. The schematic magnetic configuration of the sample before and after spin-flop in the in-plane applied field. B_S is the in-plane saturation field of $Gd_{1-x}Co_x$ layer, and B_{sf} is the spin-flop field.

Since the total magnetisation of $Gd_{1-x}Co_x$ is still parallel to the in-plane applied field after spin-flop, i.e. only the Gd and Co sublattice magnetisations rotate from the film plane (Fig. 7.16), the decrease of R_H after spin-flop confirms that the GMR does not depend on the angle between the magnetisation of $Ni_{81}Fe_{19}$ and the total magnetisation of $Gd_{1-x}Co_x$, but depends on the angles between the magnetisation of $Ni_{81}Fe_{19}$ layer and the magnetisations of Gd and Co sublattices of the $Gd_{1-x}Co_x$ layer.

7.7. Conclusion

In this chapter, we have fabricated and characterised a new type of GMR junction with a $Gd_{1-x}Co_x$ layer having perpendicular anisotropy and a $Ni_{81}Fe_{19}$ layer having in-plane anisotropy. The in-plane applied field measurements in two configurations B // EAP and B ⊥ EAP prove that there is GMR in the sample.

The extraordinary Hall effect has been used as a useful method to study the magnetic reversal of $Gd_{1-x}Co_x$ layer. The change of the $Gd_{1-x}Co_x$ layer magnetisation from Co-dominant ($T > T_{comp}$) to Gd-dominant ($T < T_{comp}$), i.e. the reversal of the spin polarisation from positive to negative, at the compensation temperature reverses the GMR of sample from negative (normal GMR) to positive (inverse GMR).

The impact of spin-flop phenomenon of the $Gd_{1-x}Co_x$ layer on the GMR of sample has been investigated for the first time. The obtained results show that the GMR of sample does not depend on the angle between the $Ni_{81}Fe_{19}$ layer magnetisation and the $Gd_{1-x}Co_x$ layer magnetisation, but depends on the angles between the $Ni_{81}Fe_{19}$ magnetisation and the magnetisations of Gd and/or Co sublattices. The resistance of sample will be minimum or

maximum when the Co sublattice magnetisation is parallel or antiparallel to the magnetisation of $Ni_{81}Fe_{19}$, respectively.

However, there are still several questions in need of answering: Is there a coupling between $Ni_{81}Fe_{19}$ and $Gd_{1-x}Co_x$ layers? Is there any difference between the contributions of the Gd and Co sublattice magnetisations to the GMR of sample? Is it possible to make GMR junctions with perpendicular magnetic anisotropy in both magnetic layers using $Gd_{1-x}Co_x$ alloys? The further study on GMR of the GMR junctions based on $Gd_{1-x}Co_x$ layers is still going on at IN. We hope that these questions will be answered soon.

Main conclusion

1. $Gd_{1-x}Co_x$ thin film

$Gd_{1-x}Co_x$ thin films with an in-plane gradient of composition have been fabricated in a reproducible way. The existences of a compensation zone and compensation domain walls have been investigated by means of the polar Kerr effect (PKE) and the extraordinary Hall effect (EHE). The compensation domain walls are ideal 180^o domain walls because they are very stable and can be moved easily under control by changing the temperature in a constant applied field. The in-plane composition gradient of the $Gd_{1-x}Co_x$ thin film has been calculated by comparing the composition dependence of T_{comp} calculated by the mean-field model and the transference velocity of the compensation domain wall with the change of temperature. The compensation domain walls should prove useful in the near future for studying and controlling a single domain wall as current-induced switching, and current-induced RF oscillations. Manipulating a single domain wall has also opened new perspectives in magnetic logic and recording.

The extraordinary Hall effect of $Gd_{1-x}Co_x$ thin film has been investigated following the variations of applied field (from 0 T to 6 T) and temperature (from 5 K to 300 K). For the first time, the quantitative contributions of the Gd and Co sublattice magnetisations to the EHE have been estimated. The Co moments make positive sense ($R_{Co} > 0$) while the Gd moments make negative sense ($R_{Gd} < 0$) to EHE. In the EHE amplitude, a dominant role of Co moments has been specified. The contribution of Co moments (near 90%) to EHE is very much larger than the contribution of Gd moments.

The perpendicular multidomain structure of the $Gd_{1-x}Co_x$ thin film has been studied by means of the in-plane applied field EHE. The spin-flop phenomenon of the $Gd_{1-x}Co_x$ thin film has been well investigated by means of the perpendicular applied field EHE. By using the mean-field simulation, the impact of magnetic anisotropy on the spin-flop field (B_{sf}) has been evaluated. The calculated results show that B_{sf} is always minimum at the compensation temperature (T_{comp}) of $Gd_{1-x}Co_x$ layer, but the minimum value of B_{sf} strongly depends on the anisotropy of the $Gd_{1-x}Co_x$ layer (K_{Co}). Because of the anisotropy, the minimum B_{sf} at T_{comp} is not zero anymore. The larger the K_{Co} is, the larger the minimum B_{sf} is. This prediction has been experimentally proved on the unpatterned sample S1 (with $B_{sf} = 0.7$ T at $T_{comp} = 235$ K) and the patterned sample S2a (with $B_{sf} = 1.8$ T at $T_{comp} = 193$ K).

Although the deviation between calculated and experimental results of the spin-flop field (B_{sf}) is still large, the comparison between the unpatterned sample S1 and the patterned sample S2 reveals an important influence of the compositional inhomogeneity on the spin-flop field. In the next studies, the $Gd_{1-x}Co_x$ thin film will be patterned in smaller dimensions to minimise the impact of compositional inhomogeneity.

2. Giant magnetoresistance

The spin dependent scattering at the Fe/Cr interface of Fe/Cr multilayers has been studied by changing the Fe layer thickness. The high temperature heat treatment has been applied to widen the Fe/Cr interfaces. The obtained results supposed a dominant contribution of the scatterings in the Fe/Cr interfaces comparing to the scatterings in the Fe layer cores. The multilayer structure remains stable during annealing up to 350 ^oC. At higher temperatures, the multilayer structure is modified and the onset of ferromagnetic coupling is found, leading to the reduction of the GMR signal.

In an effort of making a new type of GMR junction with perpendicular anisotropy of magnetic layer, $Gd_{1-x}Co_x$ alloy has been applied to make GMR junction $Ni_{81}Fe_{19}/Cu/Gd_{1-x}Co_x$. The PKE measurement proved that the $Gd_{1-x}Co_x$ layer has perpendicular anisotropy at room temperature. The in-plane applied field measurement in the two configurations B // EAP and B $\perp$ EAP proves that GMR exists in the sample. The magnetic reversal of $Gd_{1-x}Co_x$ layer in both low and high applied fields has been investigated by means of EHE. The obtained results showed that GMR of the sample depends on the angle between the $Ni_{81}Fe_{19}$ magnetisation and the magnetisations of Gd and Co sublattices of the $Gd_{1-x}Co_x$ layer. The reversal of magnetisation from Co-dominant ($T > T_{comp}$) to Gd-dominant ($T > T_{comp}$) at T_{comp} reverses the GMR of sample from negative (normal GMR) to positive (inverse GMR).

Publications

1. N.H. Duc, N.A. Tuan, N.T. Nam, and V.N. Thuc, *Giant Magnetoresistance and magnetostriction in nanostructured multilayers*. Proceedings of the International Workshop on Nanophysics and Nanotechnology (IWONN'02), Vietnam (Hanoi), 20-21 June 2002.
2. N. H. Duc, N. A. Tuan, N. T. Nam, N. H. Sinh, J. Teillet, and A. Fnidiki, *Low-field magnetoresistance of Fe/Cr multilayers*. Physica B **327**, 334 (2003).
3. N. T. Nam, N. H. Duc, and L. T. Tai, *Angular dependence of giant magnetoresistance in Fe/Cr multilayers*. Proceedings of the Ninth Asia Pacific Physic Conference (9^{th}APPC), Vietnam (Hanoi), 25-31 October 2004.
4. N. T. Nam, Y. Conraux, C. Meyer, N. H. Duc, and L. Ranno, *Composition-controlled compensation domain wall in GdCo thin films*, The Third Joint European Magnetic Symposia, Spain (San Sebastian), 26-30 June 2006.
5. N. T. Nam and L. Ranno, *Giant magnetoresistance junction using GdCo as a ferrimagnetic layer*, Journées de la Matière Condensée (JMC10), France (Toulouse), 28-31 August 2006.
6. N. T. Nam and L. Ranno, *GMR junction based on a compensated ferrimagnet*, 11 ème Colloque Louis Néel, France (Lyon), 14-16 Mars 2007.
7. L. Ranno and N. T. Nam, *Ferrimagnétique compensé revisité pour l'électronique de spin*, 11 èm Colloque Louis Néel, France (Lyon), 14-16 Mars 2007.

List of Symbols and Abbreviations

Abbreviations	**Comments**
AMR	Anisotropic Magnetoresistance
CNRS	Centre National de La Recherche Scientifique (Grenoble, France)
CryoLab	Cryogenic Laboratory, Vietnam National University in Hanoi
DOS	Density of State
EAP	Easy Axis of Permalloy ($Ni_{81}Fe_{19}$)
EHE	Extraordinary Hall Effect
GMR	Giant Magnetoresistance
IN	Institut Néel, Grenoble
MR	Magnetoresistance
OHE	Ordinary Hall Effect
OMR	Ordinary Magnetoresistance
P	Spin Polarisation of Conduction Electrons
P_N	DOS Spin Polarisation
PHE	Planar Hall Effect
PKM	Polar Kerr Microscope
UJF	Université Joseph Fourier (Grenoble 1)
VNUH	Vietnam National University in Hanoi

List of References

[1]. P. Chaudhari, J. J. Coumo, and R. J. Gambino, IBM J. Res. Dev. **17** (1973), 66

[2]. J. M. D. Coey, J. Appl. Phys. **49** (1978), 1646

[3]. P. Hansen, C. Clausen, G. Much, M. Rosenkranz, and K. Witter, J. Appl. Phys. **66** (1989), 756

[4]. P. Hansen, in: Handbook of Magnetic Materials, Vol. 6, ed. K.H.J. Buschow, North-Holland, Amsterdam (1991), 290

[5]. R. C. Taylor and A. Gangulee, J. Appl. Phys. **47** (1976), 4666

[6]. A. Gangulee and R. C. Taylor, J. Appl. Phys. **49** (1978), 1762

[7]. Neil. Heiman, Kenneth Lee, and Robert I. Potter, J. Appl. Phys. **47** (1976), 2634

[8]. K. Handrich, Phys. Status. Solidi. **32** (1969), K55

[9]. I. A. Cambell, J. Phys. F. 2 (1972), L47

[10]. J. P. Liu, X. P. Zhong, F. R. de Boer, and K.H.J. Buschow, J. Appl. Phys. **69** (1991), 5536

[11]. T. Kohashi, M. Ono, M. Date, A. Yamagishi, X. P. Zhong, Q. Wang, F. M. Yang, R. J. Radwanski, and F. R. de Boer, J. Appl. Phys. **69** (1991), 5542

[12]. N.H. Duc, T.D. Hien, and D. Givord, J. Magn. Magn. Mater., **104-107** (1992), 1344

[13]. N.H. Duc, and D. Givord, J. Magn. Magn. Mater., **124** (1993), 305

[14]. N.H. Duc, and D. Givord, J. Magn. Magn. Mater., **157-158** (1996), 169

[15]. Structure Reports, vol. **26**, ed. W.B. Pearson (1960), 120

[16]. R.J. Radwanski, Physica **B 142** (1986), 57

[17]. M. D. Kuz'min, Y. Skourski, D. Eckert, M. Richter, K. H. Müller, K.P. Skokov, and I.S. Tereshina, Phys. Rev. **B 70** (2004), 172412

[18]. M. Hong, E. M. Gyorgy, and D. D. Bacon, Appl. Phys. Lett. **44** (1984), 706

[19]. A. H. Eschenfelder, in: Ferromagnetic Materials, Vol. 2, ed. E. P. Wohlfarth, , North-Holland, Amsterdam (1980), 354

[20]. Jan H. Fluitman, J. Appl. Phys. **52** (1981), 2468

[21]. Z. Q. Lu, G. Pan, J. Li, and W. Y. Lai, J. Appl. Phys. **89** (2001), 7215

[22]. S. U. Jen, K. P. Huang, and J. C. Lee, J. Appl. Phys. **84** (1998), 843

[23]. A. Schuhl, F. Nguyen Van Dau, and J. R. Childress, Appl. Phys. Lett. **66** (1995), 2751

[24]. E. H. Hall, Phil. Mag. **10** (1880), 301

[25]. E. H. Hall, Phil. Mag. **12** (1881), 157

[26]. R. Ballou, J. Deportes, B. Gorges, R. Lemaire and J.C. Ousset, J. Magn. Magn. Mater.,

54-57 (1986), 465

[27]. R.J. Radwanski, J.J.M. Franse, P.H. Quang, and F.E. Kayzel, J. Magn. Magn. Mater. **104-107** (1992), 1321

[28]. J. M. Luttinger, Phys. Rev. **112** (1958), 739

[29]. L. Berger, Phys. Rev. **B 2** (1970), 4559

[30]. L. Berger and G. Bermann, in: The Hall Effect and Its Applications, ed. C.L. Chien and C.R. Westgate, Plenum Press, New York (1980), 55

[31]. T. R. McGuire, R. J. Gambino, and R. C. O' Handley, in: The Hall Effect and Its Applications, ed. C.L. Chien and C.R. Westgate, Plenum Press, New York (1980), 137

[32]. A. W. Smith and R. W. Sears, Phys. Rev. **34** (1929), 1466

[33]. E. M. Pugh and N. Rostoker, Revs. Mod. Phys. **25** (1953), 151

[34]. A. Ogawa, T. Katayma, M. Hirano, and T. Tsushima, AIP Conf. Proc. **24** (1974), 575.

[35]. K. Okamoto, T. Shirakawa, S. Matsuchita, and Y. Sakurai, IEEE Trans. Magn. **10** (1974), 799

[36]. T. Shirakawa, Y. Nakajima, K. Okamoto, S. Matsuchita, and Y. Sakurai, AIP. Conf. Proc. **34** (1976), 349

[37]. R. Asomoza, I. A. Campbell, H. Jouve, and R. Meyer, J. Appl. Phys. **48** (1977) 3829

[38]. Y. Mimura, N. Imamura, and Y. Kushiro, J. Appl. Phys. **47** (1976) 3371

[39]. A. Ogawa, T. Katayma, M. Hirano, and T. Tsushima, Jap. J. Appl. Phys supplement. **15** (1976), 87.

[40]. T. R. McGuire, R. J. Gambino, and R. C. Taylor, J. Appl. Phys. **48 (**1977), 2965

[41]. A. P. Cracknell and R. A. Vaughan, in: Magnetism in Solids, Redwood Burn Limited, Trowbridge, Wiltshire (1981), 50

[42]. R. J. Gambino, P. Chaudhari, and J. J. Cuomo, AIP Conf. Proc. **18** (1974), 578

[43]. R. Malmhäll, J. Appl. Phys. **54** (1983), 5128

[44]. E. du Tremolet de Lacheisserie, B. Gignoux, and M. Schlenker in: Magnetism, Vol. 1, Springer (2005), 403

[45]. A. Gerber, A. Milner, A. Finkler, M. Karpovski, L. Goldsmith, J. Tuaillon-Combes, O. Boisron, P. Melinon, and A. Perez, Phys. Rev. **B 69** (2004), 224403

[46]. H. W. Schumacher, C. Chappert, R. C. Sousa, P. P. Freitas, and J. Miltat, Phys. Rev. Lett. **90** (2003), 017204

[47]. J. A. Katine, F. J. Albert, R. A. Buhrman, E. B. Myers, and D. C. Ralph, Phys. Rev. Lett. **84** (2000), 3149

[48]. S. I. Kiselev, J. C. Sankey, I. N. Krivorotove, N. C. Emley, R. A. Buhrman, and D. C. Ralph, Nature 425 (25 sept. 2003), 380

[49]. D. A. Allwood, G. Xiong, C. C. Faulkner, D. Atkinson, D. Petit, and R. P. Cowburn,

Science **309** (9 sept. 2005), 1688

[50]. S. S. P. Parkin, U. S. Patent No 6,834,005, No 6,898,132 (2004)

[51]. N.H. Duc, N.T.M. Hong, and J. Teillet, J. Magn. Magn. Mat. **316** (2007), 269

[52]. D. Givord, A. D. Santos, Y. Souche, J. Voiron, S. Wüchner, J. Magn. Magn. Mat. **121** (1993) 216

[53]. R. Morales, J. I. Martin, and J. M. Alameda, Phys. Rev. **B 70** (2004), 174440

[54]. C. Kaiser, A. F. Panchula, and S. S. P. Parkin, Phys. Rev. Lett. 95 (2005), 047201

[55]. Xin Jiang, Li Gao, Jonathan Z. Sun, and Stuart S. P. Parkin, Phys. Rev. Lett. **97** (2006), 217202

[56]. Christian Kaiser and Stuart S. P. Parkin, Appl. Phys. Lett. **88** (2006), 112511

[57]. P. Chaudhari, J. J. Cuomo, and R. J. Gambino, Appl. Phys. Lett. **22** (1973), 337

[58]. J. P. Nozières, L. Ranno, and Y. Conraux, U. S. patent No 7,129,555 (2006)

[59]. R. D. McMichael and M. J. Donahue, IEEE Trans. Magn. **33** (1997), 4167

[60]. M. Laufenberg, D. Backes, W. Bührer, D. Bedau, M. Kläui, U. Rüdiger, C. A. F. Vaz, J. A. C. Bland, L. J. Heyderman, F. Nolting, S. Cherifi, A. Locatelli, R. Belkhou, S. Heun, and E. Bauer, Appl. Phys. Lett. **88** (2006), 52507

[61]. M. Kläui, C. A. F. Vaz, J. Rothman, J. A. C. Bland, W. Wernsdorfer, G. Faini, and E. Cambril, Phys. Rev. Lett. **90** (2003), 97202

[62]. C. C. Faulkner, M. D. Cooke, D. A. Allwood, D. Petit, D. Atkinson, and R. P. Cowburn, J. Appl. Phys. **95** (2004), 6717

[63]. M. Kläui, H. Ehrke, U. Rüdiger, T. Kasama, R. E. Dunin-Borkowski, D. Backes, L. J. Heyderman, C. A. F. Vaz, J. A. C. Bland, G. Faini, E. Cambril, and W. Wernsdorfer, Appl. Phys. Lett. **87** (2005), 102509

[64]. A. Himeno, S. Kasai, and T. Ono, J. Appl. Phys. **99** (2006), 08G304

[65]. G. S. D. Beach, C. Nistor, C. Knutson, M. Tsoi, and J. L. Erskine, Nature Mater. **4** (2005), 741

[66]. Y. Nakatani, A. Thiaville, and J. Miltat, Nature Mater. **2** (2003), 521

[67]. D. A. Allwood, G. Xiong, C. C. Faulkner, D. Atkinson, D. Petit, and R. P. Cowburn, Science **309** (2005), 1688

[68]. L. Berger, J. Appl. Phys. **55** (1984),1954

[69]. J. C. Slonczewski, J. Magn. Magn. Mater. **159 (**1996), L1

[70]. H. J. Leamy and A. G. Dirks, J. Appl. Phys. **50** (1979), 2871

[71]. T. Mizoguchi and G. S. Cargill III, J. Appl. Phys. **50** (1979), 3570

[72]. S. Tsunashima, H. Takagi, K. Kamegaki, T. Fujii, and S. Uchiyama, IEEE Trans. Magn. MAG-14 (1978),844

[73]. H. Takagi, S. Tsunashima, S. Uchiyama, and T. Fujii, J. Appl. Phys. **50** (1979), 1642

[74]. Y. J. Choe, S. Tsunashima, T. Katayama, and S. Uchiyama, J. Magn. Soc. Jpn. **11** (1987), 273

[75]. W. H. Meiklejohn, F. E. Luborsky, and P. G. Frischmann, IEEE Trans. Magn. MAG-23 (1987), 2272

[76]. T. Egami, C. D. Graham, W. Dmowski, P. Zhou, P. J. Flanders, E. E. Marinero, H. Notarys, and G. Robinson, IEEE Trans. Magn. MAG-23 (1987), 2269

[77]. Y. Suzuki, S. Takayama, F. Kirino, and N. Ohta, IEEE Trans. Magn. MAG-23 (1987), 2275

[78]. M. V. Bystrov, A. Jahn, B. Knappe, and G. R. Myuller, Sov. Phys. Sol. State 18 (1976), 488

[79]. M. Mansuripur, M. F. Ruane , IEEE Trans. Magn. **22** (1986), 33

[80]. Magnetic Domain, ed. Alex Hubert and Rudolf Schäfer, Springer (1998)

[81]. S. Zhang, Phys. Rev. **B 51**, 3632 (1995)

[82]. A. Granovsky, F. Brouers, A. Kalitsov, and M. Chshiev, J. Magn. Magn. Mater. **166** (1997), 193

[83]. A. V. Vedyaev, A. B. Granovsky, A. V. Kalitsov, and F. Brouers, JETP **85** (1997), 1204

[84]. S. N. Song, C. Sellers, and J. B. Ketterson, Appl. Phys. Lett. **59** (1991), 479

[85]. P. Xiong, G. Xiao, J. Q. Wang, J. Q. Xiao, J. S. Jiang, and C. L. Chien, Phys. Rev. Lett. **69** (1992), 3220

[86]. J. M. Lavine, Phys. Rev. **123** (1961), 1273

[87]. J. A. Dreesen and E. M. Pugh, Phys. Rev. **120** (1960), 1218

[88]. R. Malmhall, G. Backstrom, S. M. Bhagat, and K. V. Rao, J. Non-Cryst. Solids **28** (1978), 159

[89]. L. Ranno in: Alloy Physics, ed. Wolfgang Pfeiler, John Wiley & Sons Inc (2007)

[90]. M. N. Baibich, J. M. Broto, A. Fert, Nguyen Van Dau, F. Petroff, P. Eitenne, G. Creuzet, A. Friederich, and J. Chazelas, Phys. Rev. Lett. **61** (1988), 2472

[91]. G. Binasch, P. Grünberg, F. Saurenbach, and W. Zinn, Rev. **B 39** (1989), 4828

[92]. S. S. P. Parkin, N. More, and K. P. Roche, Phys. Rev. Lett. **64** (1990), 2304

[93]. S. S. P. Parkin, Z. G. Li, and D. G. Smith, Appl. Phys. Lett. **58** (1991), 2710

[94]. H. Sakakima and M. Satomi, J. Magn. Magn. Mat. **121** (1993), 374

[95]. I. A. Cambell and A. Fert, in: Ferromagnetic Materials, Vol. 3, ed. E. P. Wohlfarth, North-Holland, Amsterdam (1982), 769

[96]. E. Hirota, H. Sakakima, K. Inomata, In: Giant Magneto-Resistance Devices, Springer (2002)

[97]. N.F. Mott. and H.H.Wills, “Resistance and thermoelectric properties of the transition metals”, Proc. Roy. Soc. **A 156** (1936), 368

[98]. A. Fert, I.A. Campbell, J. Phys. **F 6** (1976), 849

[99]. J.W.F. Dorleijn, Miedema, A.R., "A quantitative investigation of the two current conduction in nickel alloys", J. Phys. **F 5** (1975), 487

[100]. J.W.F. Dorleijn, Miedema, A.R., "The residual resistivities of dilute iron-based alloys in the two-current model", J.Phys.**F 7** (1977) L23

[101]. B. A. Gurney, Speriosu, V.S., Nozieres, J.P., Lefakis, H., Wilhoit, D.R., Need,O.U., Phys. Rev. Lett. **71** (1993), 4023

[102]. E. C. Stoner, Proc. Royal Soc., **A 165** (1938), 372

[103]. I. I. Mazin, Phys. Rev. Lett. **83** (1999), 1427

[104]. R. Meservey and P. M. Tedrow, Phys. Rep. **238** (1994), 173

[105]. R. J. Soulen , Science 282 (1998), 85

[106]. C. Vouille, A. Barthelemy, F. Elokan Mpondo, P. A. Schroeder, S. Y. Hsu, A. Reilly, R. Loloee, and A. Fert, Phys. Rev. **B 60** (1994), 6710

[107]. J. M. George, L. G. Pereira, A. Barthelemy, F. Petroff, L. Steren, J. L. Duvail, A. Fert, R. Loloee, P. Holody, and P. A. Schroeder, Phys. Rev. Lett. **72** (1994), 408

[108]. S. Y. Hsu, A. Barthelemy, P. Holody, R. Loloee, P. A. Schroeder, and A. Fert, Phys. Rev. Lett. **78** (1997), 2652.

[109]. C. Vouille, A. Fert, A. Barthelemy, S. Y. Hsu, R. Loloee, and P. A . Schroeder, J. Appl. Phys. **81** (1997), 4573

[110]. J. P. Renard, P. Bruno, R. Megy, B. Bartenlian, P. Beauvillain, C. Chappert, C. Dupas, E. Kolb, M. Mulloy, P. Veillet, and E. Velu, Phys. Rev. **B 51** (1995), 12821

[111]. J. P. Renard, P. Bruno, R. Megy, B. Bartenlian, P. Beauvillain, C. Chappert, C. Dupas, E. Kolb, M. Mulloy, J. Prieur, P. Veillet, and E. Velu, J. Appl. Phys. **79** (1996), 5270

[112]. C. Bellouard, H. D. Rapp, B. George, S. Mangin, G. Marchal, and J. C. Ousset, Phys. Rev. **B 53** (1996), 5082

[113]. C. Bellouard, B. George, G. Marchal, N. Maloufi, and J. Eugene, J. Magn. Magn. Mater. **165** (1997), 312

[114]. C. H. Lai, C. C. Lin, B. M. Chen, H. P. Shieh, and C. R. Chang, J. Appl. Phys. **89** (2001), 7124

[115]. F. E. Stanley, M. Peter, C. H. Marrows, S. Langridge, and B. J. Hickey, Europhys. Lett. **49** (2000), 528

[116]. D. Z. Yang, B. You, X. X. Zhang, T. R. Gao, S. M. Zhou, and J. Du, Phys. Rev. **B 74** (2006), 024411

[117]. S. Ohnishi, M. Weinert, and A. J. Freeman, Phys. Rev. **B 30** (1984), 36

[118]. F. Petroff, A. Barthelemy, D. H. Mosca, D. K. Lottis, A. Fert, P. A. Schroeder, W. P. Pratt, R. Loloee, and S. Lequien, Phys. Rev. **B 44** (1991), 5355

[119]. A. Barthélémy, A. Fert and F. Petroff, in: Handbook of Magnetic Materials, vol. 12, Ed. K.H.J. Buschow, Elsevier Science (1999), 1

[120]. F. E. Stanley, M. Perez, C. H. Marrows, S. Langridge, and B. J. Hickey, Europhys. Lett. **49** (2000), 528

[121]. Chih-Huang Lai, Chao-Cheng Lin, B. M. Chen, Han-Ping D. Shieh, and Ching-Ray Chang, J. Appl. Phys. **89** (2001), 7124

[122]. K.Y. Kim and J.E. Evetts, J. Magn. Magn. Mater., **198-199** (1999), 92

[123]. M. Hecker, D. Tietjen, D. Elefant and C.M. Schneider, J. Appl. Phys. **89** (2001), 7113

[124]. W.H. Flores, S.R. Teixeira, J.B.M. da Cunha, M.C.M. Alves, H. Tolentino, A. Traverse, J. Magn. Magn. Mater. **233** (2001), 100